Nonlinear Aeroelasticity and Active Control of Airfoils Subjected to Gusts

Xiaoyang Zhang

A Thesis

in

The Department

of

Mechanical, Industrial and Aerospace Engineering

Presented in Partial Fulfillment of the Requirements

For the Degree of Master of Applied Science (Mechanical Engineering)

Concordia University

Montréal, Québec, Canada

November 2019

Concordia University

School of Graduate Studies

This is to certify that the thesis prepared

By: **Xiaoyang Zhang**

Entitled: **Nonlinear Aeroelasticity and Active Control of Airfoils Subjected to Gusts**

and submitted in partial fulfillment of the requirements for the degree of

Master of Applied Science (Mechanical Engineering)

complies with the regulations of this University and meets the accepted standards with respect to originality and quality.

Signed by the final examining committee:

_____ Dr. Tsz Ho Kwok, Chair

_____ Dr. Chunjiang An, External Examiner (BCEE)

_____ Dr. Farjad Shadmehri, Internal Examiner

_____ Dr. Wen-Fang Xie, Supervisor

_____ Dr. Mojtaba Kheiri, Supervisor

Approved by _____

Dr. Martin Pugh, Chair

Department of Mechanical, Industrial and Aerospace Engineering

_____ 2019 _____

Dr. Amir Asif, Dean

Gina Cody School of Engineering and Computer Science

Abstract

Nonlinear Aeroelasticity and Active Control of Airfoils Subjected to Gusts

Xiaoyang Zhang

In this thesis, the coupling effects of structural nonlinearities and a gust input on the aeroelastic behaviour of an airfoil are studied, and an adaptive controller which is effective for suppressing limit-cycle oscillations (LCOs) is designed. The dynamics of the airfoil are approximated via two- (pitch and plunge) and three-degree-of-freedom (pitch, plunge and flap) models. Different types of structural nonlinearities, such as free-play and hysteresis are considered in the modelling. The nonlinear dynamics is analyzed based on time history, power spectral density (PSD), phase-plane, and Poincaré section plots, along with the estimation of the dominant Lyapunov exponent for the chaotic-like motion. It is found that free-play and hysteresis nonlinearities may considerably reduce the critical flow velocity compared to the linear system. The dynamic responses of the nonlinear system to sharp-edged and 1-cosine gust profiles are obtained at different flow velocities and compared to those of the system with no gust input. In addition, basin of attraction is plotted to show the stability boundary of the system subjected to a sharp-edged gust with various amplitudes. It is discussed that as the gust becomes stronger, the likelihood of the occurrence of LCO increases. Based on the nonlinear model with a control surface, the suppression of LCO is studied. Without uncertainties, a PD controller together with a partial feedback linearized controller can effectively alleviate oscillations due to gusts and structural nonlinearities. Considering some uncertain structural parameters, an adaptive controller with estimation parameter update

law is further designed to stabilize the system. A Lyapunov function is constructed and utilized to prove the stability of the system.

To my beloved parents

Qian Zhang, Yan Li

and

my lovely Fiancée,

Xixi Guo

Acknowledgments

By completing this dissertation, my Master's degree takes the final step towards its conclusion. While conceiving these few words, I realized how many people I owe for their support, so that acknowledging all of them within this limited space is not possible. Therefore, I wish to express my sincere gratitude to all those who have helped me in attaining such a goal.

Besides that, it is my pleasure to express my deepest gratitude to my supervisors, Prof. Wen-Fang Xie and Prof. Mojtaba Kheiri, for their nonstop supports, suggestions, and direction, as well as the financial support throughout the course of this study. I would like to thank them for all that I could learn from their talents and experience, and for all the possibilities they gave me during my research. I particularly appreciated the freedom they accorded to my research, and their trust in my capabilities that always encouraged my steps from the very beginning. I am aware that spending these years under their supervision was an invaluable opportunity in my professional and scientific career.

In addition, I would like to thank Dr. Weixing Yuan during my four-month summer work at National Research Council Canada (NRC), for giving his precious and kind advice regarding my research and sharing his extended experience in engineering.

Hearty thanks also go to my colleagues and friends who accompanied me along these years: Ms. Tingting Shu, Mr. Pengcheng Li and Mr. Juqi Hu. I am also grateful to all those people who have given me support and I didn't have the chance to thank them.

Last, but not least, my gratitude and sincere thanks go to my family, including my parents and my fiancée for their support, kindness and ‘being always there’ regardless of my choices, and for having allowed, with their efforts, to get to where I am now.

Contents

List of Figures

List of Tables

List of Symbols

a	nondimensional distances of the elastic axis from the mid-chord
$C_{L\alpha}$	the lift-curve slope (normally taken as 2π)
c_m	nondimensional distances of the control surface (flap)
	hinge line from the mid-chord
L	lift of the lifting surface
M	pitching moment of the wing-flap about the elastic axis
M_0	preload for freeplay model
M_a	aerodynamic pitching moment of the wing-flap system
M_f	stiffness in the freeplay zone
m	mass per unit span of the entire wing
m_{tot}	mass per unit span of the entire wing plus the support blocks[1]
N_ξ, N_α, N_β	the nonlinear plunge, pitch and flap structural stiffness terms
r_α	radius of gyration of the wing-flap with respect to the semi-chord b
r_β	radius of gyration of the flap with respect to the semi-chord b
T	pitching moment (or torque) of the flap about its hinge
U_∞	air flow velocity
$U^* = U_\infty/(b\omega_\alpha)$	dimensionless velocity
x_α	nondimensional distance of the centre of gravity of the wing-flap
	from the elastic axis
x_β	nondimensional distance of the reduced centre of gravity of the flap
	from the hinge line

[1] Considering the mass of support blocks would allow for comparison with experimental results.

α	pitch displacement about the elastic axis
β	aileron (flap) displacement about the hinge line
	(relative to the main wing surface)
β_c	control command input
δ	total angular size of the freeplay region
δ_f	freeplay angle offset
ζ_ξ, ζ_α, ζ_β	viscous structural damping coefficients for plunge, pitch
	and flap degrees-of-freedom
ν	modified control input
ξ	plunge DOF
ρ_∞	air density
τ	$U_\infty t/b$, the dimensionless time
ω_ξ, ω_α, ω_β	uncoupled pitching, plunging and flapping modes natural frequencies
$\bar{\omega}_1$	ω_ξ/ω_α
$\bar{\omega}_2$	$\omega_\beta/\omega_\alpha$
$(\dot{})$	$\partial()/\partial t$, t being time
$(\breve{})$	reduced lift $(/mb)$ or moment $(/mb^2)$
$(\hat{})$	estimated parameter
$(\tilde{})$	estimation error
Superscripts	
$'$	$\partial()/\partial\tau$
Subscripts	
a	aerodynamic component
g	gust component

Chapter 1

Introduction

1.1 Motivation

Aeroelasticity is an interdisciplinary field concerning the interactions between aerodynamic, inertial and elastic forces, and the influence of these interactions on the aircraft design and performance. There is a growing tendency in the aerospace industry for improving fuel efficiency of commercial transport aircraft via reducing the airframe weight and increasing the aerodynamic efficiency (e.g. by increasing the lift-to-drag ratio using higher aspect-ratio wings) [1]. The potential implication of such modifications is the increase of the structural flexibility. On the other hand, defence sectors demand more agile, higher-speed combat aircraft. Increasing structural flexibility and/or expanding the flight envelope of an aircraft would normally make it more susceptible to larger structural deformations and more prone to complex aerodynamic phenomena, such as flow separation and wake roll-up.

Classical aeroelastic theories were developed assuming linear aerodynamics and structures. The problem then reduces to solving a set of linear equations, often described in

the *state-space* form, which can be readily solved in either time or frequency domain. Linear aerodynamic theories usually fail to give accurate results at high subsonic or transonic airspeeds [2]. On the other hand, linear structural dynamic theories normally become unreliable when structural deformations become large – *geometric nonlinearities*. Structural nonlinearities also arise from worn hinges of control surfaces, loose control linkages and material behaviour (e.g. when the yield stress is exceeded leading to a nonlinear stress-strain relationship) [1, 2].

Aeroelastic flutter is a potentially catastrophic instability – it can quickly destroy an aircraft. Classical aeroelastic theories do not take into account structural and aerodynamic nonlinearities [3]. While different types of structural and aerodynamic nonlinearities are commonly encountered in aeronautical engineering [2]. Nonlinearities can make the aeroelastic stability and dynamical behaviour of system more complex. An aircraft may be disturbed by a time-dependent external excitation, such as a gust, during its normal operation. The coupling effects of nonlinearities and disturbances are worth investigating. Nevertheless, to the best of the author's knowledge, only few studies exist on the nonlinear aeroelastic response of a lifting surface to a time-dependent external disturbance. Most of the previous studies were only concerned about the cubic-type nonlinearity and also with incomplete details about the dynamics of the system in the presence of a gust input. The immediate necessity for studies such as this thesis may be recognized by the emergence of new applications, such as Urban Air Mobility where the flying vehicle will normally experience highly-turbulent gusty airflow. The nonlinear aeroelastic behaviour of an aircraft flying in such conditions is yet to be investigated.

In the reality, aeroelastic problem, potentially manifested as self-sustained or divergent oscillations, can be sensitive to many parameters whose values are uncertain [4]. Based on instability and uncertainty of the nonlinear aeroelastic system, the design of effective

controllers to suppress flutter is particularly crucial for the new generation of aircraft which are likely to be lighter, faster, more flexible, and more agile. In this thesis, the coupling effects of structural nonlinearities and time-dependent gust are investigated and the adaptive controller to suppress LCO, which may also called as *mild flutter* [5], is designed considering structural uncertainties.

1.2 Literature Review

In this section, a literature review on the nonlinear aeroelasticity and active control of aeroelastic system is presented. In addition, some studies on the gust response, as well as its suppression are reviewed.

1.2.1 Nonlinear Aeroelasticity

Aeroelasticity is an interdisciplinary field of study dealing with interactions between inertia, aerodynamic and elastic forces. Classical theories in aeroelasticity assume linear aerodynamics and structural dynamics resulting in modelling with a set of linear equations. These equations can be fairly easily solved in time or frequency domain and be used for examining the aircraft stability and response to external excitation. However, linear aerodynamic theories start to break down at high airspeeds. Flow separation and shock oscillations may also introduce aerodynamic nonlinearities. Moreover, structural nonlinearities may arise from, for example, large deformations, material behaviour, worn hinges of control surfaces, and loose control linkages, as discussed in [2, 5].

Woolston *et al.* [5] may be the first researchers who investigated the effects of structural nonlinearities on the flutter of a wing. Two different wing models were studied: (i) a wing capable of bending and twisting or a two-degree-of-freedom (2-DOF) system, and (ii) a wing

with a control surface (i.e. 3-DOF system). They considered structural nonlinearities as concentrated in the torsional stiffness. Three different types of nonlinear springs, namely flat spot or dead zone, hysteresis, and cubic were examined. The flat spot type nonlinearity was used to represent free play in the hinge or linkage of a control system.[1] They found that there is a strong connection between the stability of a nonlinear system and the initial conditions - in many cases the flutter speed was decreased as the initial disturbance was increased.

Lee *et al.* [6] studied nonlinear flutter of a two-dimensional (2-D) airfoil undergoing plunging and pitching motions using a time marching finite difference scheme, considering a spring with preload and free-play in the pitching DOF. By setting different values of freeplay, preload, initial conditions and system parameters, they compared and analysed the time history and flutter boundary diagrams. They observed three types of oscillatory motion, namely damped, limited amplitude and divergent. They found that with the presence of a structural nonlinearity of the type considered, the divergent flutter speed is the same as the linear flutter speed. Also, different values of preload and initial conditions did not appear to affect the limited amplitude of oscillatory motion for both DOFs. In contrast, changing the system parameters, such as the ratio of the uncoupled natural frequencies had noticeable effects on the limited amplitudes.

A comprehensive review of different types of structural and aerodynamic nonlinearities encountered in aeronautical engineering was conducted by Lee *et al.* [2]. They discussed several techniques, such as finite difference and describing function for solving equations with structural nonlinearities. They found that even a 2-DOF system with a single nonlinearity in the pitch degree of freedom might show a complex dynamical behavior. For example,

[1]The phrases 'flat spot' and 'free play' will be used interchangeably throughout the paper. Similarly are the phrases 'torsional stiffness/spring' and 'rotational stiffness/spring'.

they showed that a system with a free-play nonlinearity might undergo period-1, period-2, and period-4 limit-cycle oscillations (LCO) as well as chaotic motion, depending on the airspeed.[2] Dowell and Tang [7] studied four specific aeroelastic models carrying different sources of nonlinearity: (i) an airfoil with a control surface that had hinge free play, (ii) a plate-like wing where the tension-induced bending generated a cubic stiffness, (iii) a very high-aspect-ratio wing (HARW) where the nonlinearity arose due to coupling among flapwise bending, chordwise bending and torsion of the wing structure, and (iv) a wing encountering large shock motions in the transonic flow range, which produced nonlinear aerodynamic forces. They found that plunge, pitch and flap modes dominated the flutter motion, at lower, higher and yet higher Mach numbers respectively, which agreed with the remarks in [8, Section 11.12]. Recently, Afonso *et al.* [1] conducted a review focusing on the nonlinear aeroelasticity of HARWs. They drew several conclusions from the reviewed studies. For example, HARWs were prone to instabilities if encountered by a sufficiently strong external perturbation such as a gust and turbulence.

The nonlinear aeroelastic behaviour of airfoil sections in incompressible flow was examined by many investigators. Price *et al.* [9] considered free-play nonlinearity, Price *et al.* [10] assumed bi-linear and cubic nonlinearities, and Alighanbari and Price [11] dealt with a third-order rational curve to approximate free-play nonlinearity – all assumed the nonlinearity in the pitch DOF. Liu *et al.* [12, 13] investigated the dynamic response of a two-dimensional (2-D) aeroelastic system with free-play and hysteresis stiffness nonlinearities using the point transformation method. They examined different free-play and hysteresis parameters based on various initial conditions (i.e. pitching angles) without any external excitation. Liu and Dowell [14] employed the first-order harmonic balance (HB) method, also known as the describing function approach, and also developed a higher-order HB method to study the

[2] As discussed in Section 2.2.1, period-2 and period-4 motions may actually be period-1-h and period-2-h motions, respectively.

nonlinear aeroelastic dynamics of an airfoil section that included a control surface with free play. They showed that the high-order HB method outperformed the first-order HB method, where the results were in excellent agreement with the time integration results.

Moreover, Chen *et al.* [15] applied the equivalent linearization method to cubic stiffness nonlinearies in pitching and plunging degrees-of-freedom. They found that the Hopf bifurcation leading to LCO may be subcritical or supercritical, depending on the ratio of cubic plunging and pitching stiffness coefficients. Cui *et al.* [16][17] used the precise integration method (PIM), proposed by Zhong [18] for numerically solving ordinary differential equations, to solve the aeroelastic equations for an airfoil with free-play and hysteresis stiffness nonlinearities in the pitching DOF. Through comparing the results, they showed that the PIM is superior to the widely-used Runge-Kutta method in terms of solution accuracy and computational time.

Yamasaki and Epureanu [19] proposed a method to 'forecast' bifurcations and post-bifurcations behaviour for nonlinear aeroelastic systems. The method worked based on observations of the transient response of the system in the pre-bifurcation regime, and hence it was called 'model-free'. They applied the method to a 2-DOF typical airfoil section where pitching and plunging stiffnesses were generally taken as polynomials of degree five. Recently, Ghadami and Epureanu [20] proposed an improved bifurcation forecasting method and applied the method to a 3-DOF airfoil. The improved forecasting method might be used to forecast two- and three-dimensional (i.e. a system parameter and two state variables) bifurcation diagrams.

Most recently, Zhang and Chen [21] explored the nonlinear aeroelastic behaviour of a 3-DOF airfoil with external store using analytical (i.e. based on the normal form and center-manifold theories) and numerical (i.e. fourth-order Runge-Kutta technique) approaches. Cubic stiffness was considered for the pitch, plunge and flap degrees-of-freedom. They showed

that the system may display a complex dynamics, such as chaotic motion. Tian *et al.* [22] investigated nonlinear aeroelastic characteristics of an all-movable fin in hypersonic flow considering both aerodynamic and free-play nonlinearities. They found that the temperature elevation might reduce the flutter boundary and extend the region of chaotic motions. Very complex dynamical behavior was observed due to the existence of free-play nonlinearities in both pitch and flap DOFs, especially multiple periodic, quasi-periodic LCOs and chaotic motion in low Mach number range.

In addition, Tang and Dowell [23] considered a 3-DOF typical airfoil section with control surface free play. The aerodynamic forces were obtained using Peter's finite state incompressible flow theory [24]. They investigated theoretically and experimentally the correlation of flutter/LCO behaviour when the initial pitch angle was non-zero. They also studied the linear and nonlinear aeroelastic responses to a periodic gust load. Berci *et al.* [25] investigated the aeroelastic behavior and gust response of a flexible airfoil and compared them with those of a rigid typical airfoil section. The flexible airfoil could bend and twist chordwise and was supported by linear translational and torsional springs which were used to model the spanwise elasticity. They found that the flexible airfoil underwent divergence and flutter at lower flow velocities compared to the rigid airfoil with the same aero-structural parameters. They also found that the flexible airfoil displayed higher frequency and lower amplitude oscillations, compared to its rigid counterpart, when it was encountered by a gust.

Conner *et al.* [26] studied theoretically as well as experimentally the aeroelastic behaviour of a three-degree-of-freedom typical airfoil section with control surface free-play. An interesting discovery of their experiments on the limit-cycle behaviour of the typical section was that the system parameters could be affected as a result of the fatigue associated with extended oscillatory motion. Tang *et al.* [27] analyzed theoretically and experimentally the nonlinear response of a typical airfoil section with control surface free-play, excited by

periodic and continuous linear frequency sweep gust loads in low subsonic flow. In their theoretical approach, they used Peter's [28] finite state aerodynamic theory.

Several researchers had studied the response of a lifting surface to a time-dependent external excitation. For example, Poirel and Price [29] investigated the effect of longitudinal atmospheric turbulence on the dynamics of an airfoil with a hardening, cubic structural stiffness in pitch. It was found that, in the absence of turbulence, i.e. the non-excited case, two distinct regions of dynamic response, namely stable equilibrium position and LCO, existed. However, three different regions of dynamical behaviour were observed when the airfoil was excited by longitudinal turbulence. For the excited case, within the intermediate range of flow velocities, a new type of dynamical behaviour was observed, where the airfoil response was concentrated about the equilibrium position. The existence of this new form was attributed to the parametric nature of excitation. Marzocca *et al.* [30] investigated the aeroelastic response to a time-dependent external excitation of a linear, 2-D rigid-/elastic-lifting surface in incompressible flow field, featuring plunging-pitching coupled motion. Tang and Dowell [31] studied theoretically and experimentally the gust response for an HARW. The wing was modelled structurally based on a nonlinear beam theory, and the structural dynamic equations were combined with the ONERA aerodynamic stall model.

Haddadpour *et al.* [32] examined the effects of the sharp-edged gust on the aeroelastic behaviour of a flexible HARW. In their model, they used a linear, pitching-plunging structural dynamics and linear quasi-steady aerodynamics. Bifurcation characteristics of an airfoil section with cubic structural nonlinearity in pitch direction and subjected to turbulent flow were examined by Poirel and Price [33]. Dessi and Mastroddi [34] examined the nonlinear dynamics and gust response of a 2-DOF typical airfoil section. The rigid airfoil was supported by a linear translational and a softening-type cubic rotational spring, and the gust was assumed to be of the 1-cosine form. They concluded that the excitation due to discrete gust

models was equivalent to considering the response of the system to certain initial conditions.

In [35], the integro-differential equations governing arbitrary plunging-pitching motion of an airfoil were transformed into a set of fourth-order ordinary differential equations. These equations were then used to find the flutter speed and the dynamic response of an airfoil to a sharp-edged gust excitation. Recently, Zhang *et al.* [36, 37] presented some numerical results on the nonlinear dynamics and time response of a 2-DOF typical airfoil section encountered with a gust. In [36], strong cubic and free-play stiffness models and in [37] free-play and hysteresis models were considered. They found that as the sharp-edged or 1-cosine gust becomes stronger, the probability of the occurrence of LCO in the subcritical flow regime increased.

1.2.2 Aeroservoelasticity

In addition to the *predictive* or *diagnostic* type studies, some of which were reviewed above, some studies mainly concerned suppression or at least alleviation of undesirable dynamical behaviour of aeroelastic systems.

To date, extensive research has been conducted to achieve active flutter suppression and gust alleviation, where one or more control surfaces are actuated according to a control law which relates the control command to some measurements taken, by sensors, on the aircraft. Horikawa and Dowell [38] proposed an elementary explanation of wing flutter suppression problems with active feedback control via a standard root locus technique. Their proposed feedback loop was a pure gain feedback of wing motion (i.e. bending displacement, bending acceleration at the center of mass, torsion displacement, or torsion acceleration) into a trailing-edge flap system. They used a quasi-steady aerodynamic model coupled with a 2-DOF structural dynamic model. Luton and Mook [39] developed a method for predicting the unsteady, subsonic, aero-servo-elastic response of a wing. They used a general

unsteady vortex-lattice method to model the aerodynamics, as well as a relatively simple, linear feedback control system. The control system consisted of leading- and trailing-edge ailerons moving in accordance to control laws, as well as a servo law which related the commanded angle to the actual aileron deflection. The control laws were formed based on measurements of the lateral velocity and twist angle rate of the wing tip.

Librescu *et al.* [40] developed the active flap control capability for a 2-D wing-flap system to suppress flutter and improved the subcritical aeroelastic response to time-dependent external pulses. The aerodynamic forces were derived from Theodorsen's equations using Wanger's function. They implemented plunging/pitching velocity feedback control laws and their combination, as well as linear-quadratic regulator, modified bang-bang, and fuzzy logic control. It was noted that a few errors, originating from [41], were recently discovered in [40] and subsequently corrected by Mozaffari-Jovin *et al.* [42, 43]. In addition, the work of Ko *et al.* [44] on the use of the feedback linearization to derive locally asymptotically stable (nonlinear) feedback controllers should be mentioned. Two more recent studies on the aeroservoelasticity of 2-D wings were [45, 46].

Building highly accurate aeroelastic and aero-servo-elastic models for real-world aircraft required considering uncertainties present in the structure (e.g. structural stiffness and damping), fluid flow (e.g. shock location) as well as in the control mechanism (e.g. sensors and actuators).

Dai *et al.* [47] reviewed the methods and advances made in the last few decades for the study of aeroelasticity with uncertainties. They pointed out that uncertainty modelling for nonlinearity was the most challenging task when it came to aeroelastic problems. In addition, quantification of damping was by far the most vexing problem in the structural dynamic modelling: unlike the inertial and stiffness properties of a structural system, damping was not referred to a unique physical phenomenon. Kareem and Sun [48] investigated

the dynamic response of structures with uncertain damping. Their numerical results demonstrated that the uncertainty in damping had a great influence on the system response. The effects depended on the mean value and coefficient of variation of the damping ratio. When there was a 4% difference between the estimation value and the nominal value, the root mean square (RMS) differences from two cases were quite significant. Also, as the variability increases, the higher order component response contribution to RMS increased.

Ko *et al.* [49] applied partial feedback linearization to a 2-DOF aeroelastic system with uncertain structural stiffness nonlinearities. Local stability was achieved by an adaptive controller. However, in their model, a quasi-steady flow theory was adopted and the dynamics of the control surface was neglected. Recently, Zhang *et al.* [37] succeeded in suppressing LCOs and thus stabilizing a structurally-nonlinear wing encountering a gust. In their theoretical model, however, all the parameters including nonlinear parameters must be known *a priori* to generate the control command.

1.3 Research Objectives and Main Contributions

1.3.1 Research Objectives

The main research objectives of this thesis are: 1) To study the coupling effects of a gust and structural nonlinearities on the aeroelastic behaviour of an airfoil, and 2) To develop an adaptive controller to suppress flutter and alleviate gust response of a structurally-nonlinear airfoil with uncertainties.

1.3.2 Main Contributions

Actual lifting surfaces, such as aircraft wings may contain various structural nonlinearities, and they often encountered with atmospheric turbulence during a normal flight. Nevertheless, to the best of the author's knowledge, most studies on the aeroelasticity or aeroservoelasticity of a 2-D nonlinear wing had considered structural nonlinearity only for one of the DOFs, and thus possible nonlinear interactions between vibration modes were neglected. Only few studies had been dedicated to the nonlinear aeroelastic response of a lifting surface to a time-dependent external disturbance. This thesis aims to systematically study the effects of sharp-edged and 1-cosine gusts – two standard deterministic gust models – on the dynamical behaviour of a 2-DOF typical airfoil section having either cubic, free-play or hysteresis structural nonlinearity. Moreover, very few research work had been carried out on the controller design to deal with a nonlinear aeroelastic system with uncertain structural parameters, especially for the uncertain damping coefficients.

In this thesis, the main contributions are reflected in two aspects. Regarding the first aspect, the coupling effects of a gust and structural nonlinearities (including free-play and hysteresis) on the aeroelastic behaviour of an airfoil were studied. The airfoil was modelled as either a two- or a three-degree-of-freedom system, where pitch and plunge were the main DOFs and flap was the extra DOF. Not only focusing on the pitch DOF like most researches, the dynamics of plunge DOF were also investigated. The basin of attraction under gust input was plotted and the effects of gusts on the stability and motion characteristics of nonlinear system were investigated. These studies are particularly crucial for the design of new generation of aircraft, manned or unmanned, which are likely to be lighter, faster, more flexible, and more agile. A good example is in the application of Urban Air Mobility, on which gusts may have significant effects.

Based on the nonlinear 3-DOF aeroelastic system with a control surface as the control

actuator, the second aspect of main contribution is about the control system design. Instead of quasi-steady assumption and neglect of the dynamics of control surface in most studies on suppression of flutter, the unsteady aerodynamics was utilized for the modelling and the dynamics of control surface was considered in this thesis. Since it is relatively hard to measure accurately nonlinear structural stiffness and damping coefficients, they were considered as uncertainties. The adaptive control technique was employed to stabilize the wing with uncertain system parameters. The estimation update law was designed, and the Lyapunov function was used to prove the stability of the designed adaptive control system. The numerical results show that the adaptive control system designed in this study is quite effective in suppressing LCOs and has very high robustness. The research results were summarized in the following publications:

- Xiaoyang Zhang, Mojtaba Kheiri, Wen-Fang Xie, "Nonlinear dynamics and gust response of a two-dimensional wing," submitted to *International Journal of Non-Linear Mechanics*.

- Xiaoyang Zhang, Mojtaba Kheiri, Wen-Fang Xie, "Aero-servo-elasticity of a wing with uncertain system parameters," to be submitted to *AIAA Journal*.

- Xiaoyang Zhang, Mojtaba Kheiri, Wen-Fang Xie, "Gust response of a two-dimensional nonlinear wing," in *Proceedings of the Canadian Society for Mechanical Engineering International Congress, Toronto, ON, Canada,* 2018.[36]

- Xiaoyang Zhang, Mojtaba Kheiri, Wen-Fang Xie, "Active control of a two-dimensional nonlinear wing encountering a gust," in *Proceedings of the 27th Canadian Congress of Applied Mechanics, Sherbrooke, QC, Canada,* 2019.[37]

- Xiaoyang Zhang, Mojtaba Kheiri, Wen-Fang Xie, "Adaptive control of a two-dimensional

nonlinear wing with structural stiffness and damping uncertainties," in *Proceedings of the 27th Canadian Congress of Applied Mechanics, Sherbrooke, QC, Canada,* 2019.[50]

- Xiaoyang Zhang, Weixing Yuan, "Development of flutter analysis solver FLUTQ," Volume 1, LTR-AL-2019-0047, Ottawa: National Research Council Canada, 2019.[51]

- Weixing Yuan, Xiaoyang Zhang, Dominique Poirel, "Flutter analysis solution stabilization for the PK-method," Abstract submitted to XI International Conference on Structural Dynamics (EURODYN 2020).

1.4 Thesis Outline

This thesis has six main chapters, which are organized as follows:

In Chapter 2, the typical dynamics and the gust response of a 2-DOF aeroelastic model with two different nonlinearities are presented.

Further more, the typical dynamics of a 3-DOF system with free-play nonlinearity in control surface hinge are discussed in Chapter 3.

In Chapter 4, under the assumption with no uncertainties, feedback linearization and active controller are introduced to suppress flutter and alleviate gust response.

In Chapter 5, considering uncertainties, an adaptive controller is designed and the robustness and effectiveness of the controller are assessed.

In Chapter 6, the research work at the stage of studying for Master is summarized and some possible future works are given.

Chapter 2

2-DOF Nonlinear Aeroelastic model

In this chapter, aeroelastic equations for an airfoil performing arbitrary pitching-plunging motion in inviscid, incompressible flow and subjected to a gust are presented. Numerical solutions to the dynamic model of the systems with two different structural nonlinearities are discussed. In addition, the gust response of the nonlinear system is presented.

2.1 Aeroelastic Modelling

2.1.1 Governing Equations Including the Gust Input

Fig. 2.1 shows the cross-section of a 2-D rigid wing with degrees of freedom in the plunge and pitch directions. The plunge displacement is measured from the elastic axis and is represented by h (positive downward); α is the pitch angle about the elastic axis (positive nose up). The elastic axis is located at a distance of ab from the mid-chord, while the mass center is located at a distance of $x_\alpha b$ from the elastic axis, b being the semi-chord. The wing is supported by a translational and a rotational spring, attached to the elastic axis, which generally have a nonlinear stiffness.

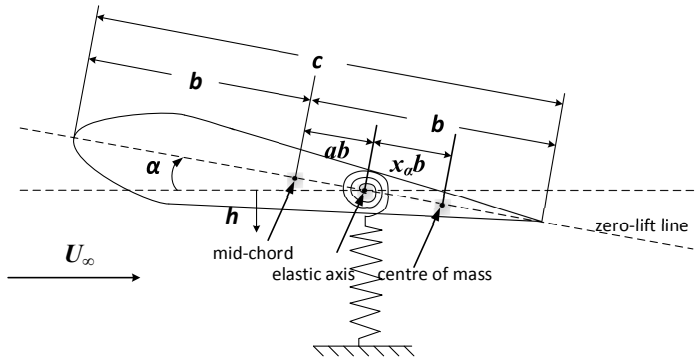

Figure 2.1: Schematic showing geometry of the wing section. The chord length is denoted by $c = 2b$; ab is the distance between the elastic axis and the mid-chord, and $x_\alpha b$ is the distance between the centre of mass and the elastic axis; α is the pitch angle (positive pitch up); also, h denotes the vertical displacement (positive downward); U_∞ is the freestream velocity. The stiffness of the wing is modelled via a translational and a rotational spring attached at the the elastic axis.

Here, following the formulations presented in [2, 30], the dimensionless aeroelastic equations featuring coupled plunging-pitching motion of a typical airfoil section subjected to a gust input are expressed as

$$\xi'' + x_\alpha \alpha'' + 2\zeta_\xi \frac{\bar{\omega}}{U^*}\xi' + (\frac{\bar{\omega}}{U^*})^2 G(\xi) - l_a(\tau) = l_g(\tau), \tag{2.1}$$

$$\frac{x_\alpha}{r_\alpha}\xi'' + \alpha'' + 2\zeta_\alpha \frac{1}{U^*}\alpha' + \frac{1}{U^{*2}} M(\alpha) - m_a(\tau) = m_g(\tau), \tag{2.2}$$

where $\xi = h/b$ is the dimensionless plunge displacement, and ζ_ξ and ζ_α are, respectively, viscous damping ratios in the pitch and plunge directions; $U^* = U_\infty/(b\omega_\alpha)$ is the dimensionless flow velocity, and $\bar{\omega} = \omega_\xi/\omega_\alpha$ is the frequency ratio, U_∞ being the freestream velocity, ω_ξ and ω_α also being natural frequencies of plunging and pitching motions, respectively; also, $l_a(\tau)$ and $m_a(\tau)$ are the aerodynamic lift and pitching moment about the elastic axis, respectively, while $l_g(\tau)$ and $m_g(\tau)$ are the lift and moment about the elastic axis due to the gust; $G(\xi)$

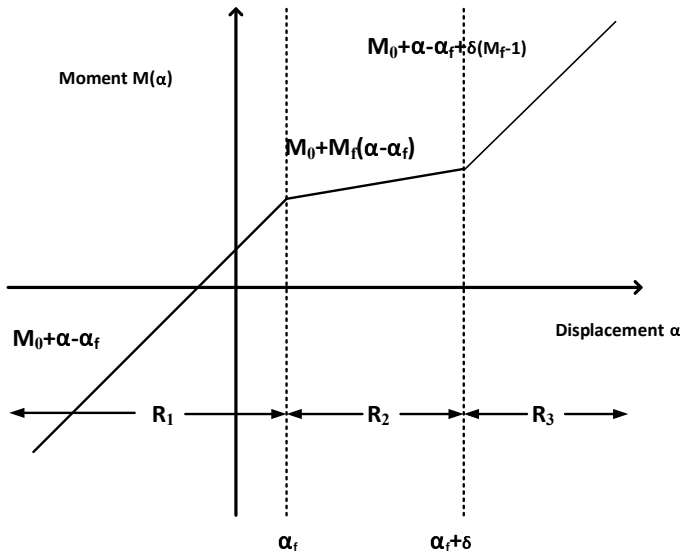

Figure 2.2: The general free-play stiffness model – the pitching moment $M(\alpha)$ versus the pitch angle α; M_0 represents the preload; M_f is the stiffness in the free-play zone, α_f is the pitch angle offset, and δ is the free-play range.

and $M(\alpha)$ represent the nonlinear plunge and pitch structural stiffness terms, respectively; moreover, $()' = \partial()/\partial\tau$ denotes the time derivative with respect to dimensionless time τ.

In this thesis, two different stiffness nonlinearities are considered in the pitch DOF. The effects of free-play will be considered as for small displacements, the spring offers no or small resistance to the deflection of the structure. The free-play nonlinearity, in its general form, may be represented by a trilinear stiffness model as [2]

$$M_\alpha = \begin{cases} M_0 + \alpha - \alpha_f, & \text{for } \alpha < \alpha_f, \\ M_0 + M_f(\alpha - \alpha_f), & \text{for } \alpha_f \leq \alpha \leq \alpha_f + \delta, \\ M_0 + \alpha - \alpha_f + \delta(M_f - 1), & \text{for } \alpha > \alpha_f + \delta, \end{cases} \tag{2.3}$$

where M_0 represents the preload, M_f the stiffness in the free-play zone, α_f the pitch angle offset, and δ the free-play range; see also Fig. 2.2.

On the other hand, the hysteresis nonlinearity may be expressed as the combination of

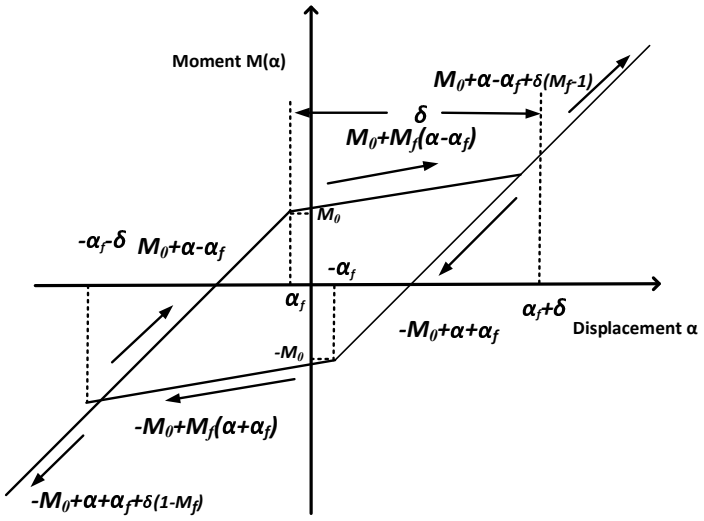

Figure 2.3: General hysteresis stiffness model; M_0 represents the preload; M_f is the stiffness in the hysteresis zone, α_f is the switching point, and δ is the hysteresis range.

two different free-play stiffness models [2]:

$$M_\alpha = \begin{cases} \alpha - \alpha_f + M_0, & \text{for } \alpha < \alpha_f, \alpha' > 0, \\ M_f(\alpha - \alpha_f) + M_0, & \text{for } \alpha_f \le \alpha \le \alpha_f + \delta, \alpha' > 0, \\ \alpha + M_0 - \alpha_f + \delta(M_f - 1), & \text{for } \alpha > \alpha_f + \delta, \alpha' > 0, \\ \alpha + \alpha_f - M_0, & \text{for } \alpha > -\alpha_f, \alpha' < 0, \\ M_f(\alpha + \alpha_f) - M_0, & \text{for } -\alpha_f - \delta \le \alpha \le -\alpha_f, \alpha' < 0, \\ \alpha - M_0 + \alpha_f - \delta(M_f - 1), & \text{for } \alpha < -\alpha_f - \delta, \alpha' < 0, \end{cases} \tag{2.4}$$

where M_0 represents the preload, M_f the stiffness in the hysteresis zone, α_f the switching point, and δ the hysteresis range; see also Fig. 2.3.

The aerodynamic lift $l_a(\tau)$ and pitching moment $m_a(\tau)$ may be expressed as

$$l_a(\tau) = -\frac{2}{\mu}\int_0^\infty \phi(\tau-\sigma)(\alpha' + \xi'' + (\frac{1}{2}-a)\alpha'')d\sigma - \frac{1}{\mu}(\alpha' + \xi'' - a\alpha''), \tag{2.5}$$

$$\begin{aligned} m_a(\tau) =& \frac{2}{\mu}(\frac{1}{2}+a)\int_0^\infty \phi(\tau-\sigma)(\alpha' + \xi'' + (\frac{1}{2}-a)\alpha'')d\sigma \\ &+ \frac{1}{r_\alpha^2\mu}a(\xi'' - a\alpha'') - \frac{1}{r_\alpha^2\mu}(\frac{1}{2}-a)\alpha' - \frac{1}{8}\frac{1}{r_\alpha^2\mu}\alpha'', \end{aligned} \tag{2.6}$$

where $\mu = m/(\pi\rho b^2)$ is the mass ratio, and $r_\alpha = I_\alpha/(mb^2)$ is the dimensionless radius of gyration; m, ρ, and I_α being, respectively, mass of the wing per unit span, air flow density, and mass moment of inertia about the elastic axis per unit span. Also, $\phi(\tau)$ is called the Wagner function and is given by

$$\phi(\tau) = 1 - A_1 e^{-b_1\tau} - A_2 e^{-b_2\tau} \ (\tau > 0), \tag{2.7}$$

where the constants are $A_1 = 0.165$, $A_2 = 0.335$, $b_1 = 0.0455$, $b_2 = 0.3$.

By considering $w_g(\tau)$ as the gust velocity and using Duhamel's integral concept, the lift and pitching moment about the elastic axis due to the penetration into the gust, $l_g(\tau)$ and $m_g(\tau)$, respectively, may be written as

$$l_g(\tau) = \frac{2}{\mu}\int_0^\tau \psi'(\tau-\sigma)\frac{w_g(\tau)}{U_\infty}d\sigma, \tag{2.8}$$

$$m_g(\tau) = (\frac{1}{2}+a)\frac{2}{r_\alpha^2\mu}\int_0^\tau \psi'(\tau-\sigma)\frac{w_g(\tau)}{U_\infty}d\sigma, \tag{2.9}$$

where $\psi(\tau)$ is called the Küssner function.

A widely-used approximation for Küssner's function is the following two-term exponential expression [2]:

$$\psi(\tau) = 1 - A_3 e^{-b_3\tau} - A_4 e^{-b_4\tau} \ (\tau > 0), \tag{2.10}$$

where the constants are $A_3 = 0.5$, $A_4 = 0.5$, $b_3 = 0.130$ and $b_4 = 1$.

In this chapter, two different gust profiles, each corresponding to a specific variation of the gust speed as a function of time, will be used. They are: (a) sharp-edged gust, and (b) 1-cosine gust. Their analytical expressions are:

$$\text{sharp-edged gust: } w_g(\tau) = H(\tau)w_0, \tag{2.11}$$

$$\text{1-cosine gust: } w_g(\tau) = \frac{1}{2}H(\tau)w_0(1 - cos\frac{\pi\tau}{\tau_g}) - \frac{1}{2}H(\tau - 2\tau_g)w_0(1 - cos\frac{\pi\tau}{\tau_g}), \tag{2.12}$$

where w_0 is the gust maximum amplitude/speed; $H(\tau)$ represents the Heaviside step function, and τ_g is half of the loading time of the gust. A dimensionless gust term of $w_0^* = w_0/U_\infty$ is introduced for the following numerical results.

2.1.2 State-space Equations

In order to deal with the integral terms in equations (2.5-2.6) and (3.7-3.8), six new variables or states are introduced as

$$\begin{aligned} w_1 &= \int_0^\tau e^{-b_1(\tau-\sigma)}\alpha(\sigma)\mathrm{d}\sigma, \;\; w_2 = \int_0^\tau e^{-b_2(\tau-\sigma)}\alpha(\sigma)\mathrm{d}\sigma, \\ w_3 &= \int_0^\tau e^{-b_1(\tau-\sigma)}\xi(\sigma)\mathrm{d}\sigma, \;\; w_4 = \int_0^\tau e^{-b_2(\tau-\sigma)}\xi(\sigma)\mathrm{d}\sigma, \\ w_5 &= \int_0^\tau e^{-b_3(\tau-\sigma)}\frac{w_g(\sigma)}{U_\infty}\mathrm{d}\sigma, \;\; w_6 = \int_0^\tau e^{-b_4(\tau-\sigma)}\frac{w_g(\sigma)}{U_\infty}\mathrm{d}\sigma. \end{aligned} \tag{2.13}$$

Using variables in equation (2.13), the aeroelastic equations (3.3) and (3.1) may be re-written as

$$c_0\xi'' + c_1\alpha'' + c_2\xi' + c_3\alpha' + c_4\xi + c_5\alpha + c_6w_1 + c_7w_2 + c_8w_3 + c_9w_4 + c_{10}w_5 + c_{11}w_6 + (\frac{\bar{\omega}}{U^*})^2G(\xi) = f(\tau), \tag{2.14}$$

$$d_0\xi'' + d_1\alpha'' + d_2\xi' + d_3\alpha' + d_4\xi + d_5\alpha + d_6w_1 + d_7w_2 + d_8w_3 + d_9w_4 + d_{10}w_5 + d_{11}w_6 + (\frac{1}{U^*})^2M(\alpha) = g(\tau), \tag{2.15}$$

where $f(\tau)$ and $g(\tau)$ are functions of the initial conditions and terms in the Wagner function, which are given as

$$f(\tau) = \frac{2}{\mu}[\xi(0) + (\frac{1}{2} - a)\alpha(0)] \times (A_1b_1e^{-b_1\tau} + A_2b_2e^{-b_2\tau}), \tag{2.16}$$

$$g(\tau) = -\frac{(1+2a)}{r_\alpha^2\mu}[\xi(0) + (\frac{1}{2} - a)\alpha(0)] \times (A_1b_1e^{-b_1\tau} + A_2b_2e^{-b_2\tau}). \tag{2.17}$$

The coefficients c_i $(i = 0, ..9)$ and d_i $(i = 0, ..9)$ in equations (2.14) and (2.15) were given in [2] and will not be repeated here for the sake of brevity; however, c_{10}, c_{11}, d_{10} and d_{11} are given as

$$c_{10} = -\frac{2}{\mu}A_3b_3,\ c_{11} = -\frac{2}{\mu}A_4b_4,$$
$$d_{10} = -(\frac{1}{2} + a)\frac{2}{r_\alpha^2\mu}A_3b_3,\ d_{11} = -(\frac{1}{2} + a)\frac{2}{r_\alpha^2\mu}A_4b_4. \tag{2.18}$$

By introducing a variable vector $\mathbf{X} = (x_1, ..x_{10})^T$ with $x_1 = \alpha,\ x_2 = \alpha',\ x_3 = \xi,\ x_4 = \xi',\ x_5 = w_1,\ x_6 = w_2,\ x_7 = w_3,\ x_8 = w_4,\ x_9 = w_5,\ x_{10} = w_6$, a set of 10 first-order ordinary

differential equations written in the explicit form can be obtained, as follows

$$\mathbf{X}' = F(\mathbf{X}, \tau). \tag{2.19}$$

2.2 Numerical Solution

The dimensionless parameters of the linear system used here for numerical solutions are: $a = -0.5$, $\mu = 100$, $x_\alpha = 0.25$, $r_\alpha = 0.5$, $\zeta_\alpha = \zeta_\xi = 0, \bar{\omega} = 0.2$ [2]. The initial conditions for plunging motion are set as $\xi'(0) = \xi(0) = 0$ for all the simulations. Using the eigenvalue solution method with the given parameters, the linear dimensionless flutter speed, that is $U_L^* = 6.28$, is obtained, which agrees well with the results given in [2].

Equation (3.18) is solved numerically using the direct time-integration method via the eight-order Dormand-Prince formula implemented as 'ode8' in MATLAB Simulink. After running several test cases with different values of the dimensionless time step, $\Delta\tau$, and the simulation time range, t_f, it was found that $\Delta\tau = 0.01$, and $t_f = 3 \times 10^4$ would be sufficient for obtaining reliable numerical results. Examples of convergence studies have been shown in Fig. 2.4. Figs. 2.4(a,b) show time histories obtained with three different time steps (i.e. $\Delta\tau = 0.1,\ 0.01, \text{and},\ 0.001$) at $U^*/U_L^* = 0.8$ and $U^*/U_L^* = 0.3$, respectively. As seen from the figures, the time response obtained with $\Delta\tau = 0.01$ is reasonably similar to that obtained with the smaller time step $\Delta\tau = 0.001$ although with a phase difference at $U^*/U_L^* = 0.3$. Quantitatively speaking, the relative error between the root mean square (rms) of amplitudes changes from $6.42 \times 10^{-5}\%$ to $6.48 \times 10^{-6}\%$ for $U^*/U_L^* = 0.8$ and from 5.07% to 0.18% for $U^*/U_L^* = 0.3$ when $\Delta\tau$ is reduced from 0.1 to 0.001; see Table 2.1. Thus, $\Delta\tau = 0.01$ is sufficiently small to ensure accurate results throughout the present paper.

To investigate the minimum required time range for accurate numerical solutions, power

Table 2.1: Root mean square (rms) of pitch displacement with $a = -0.5$, $\mu = 100$, $x_\alpha = 0.25$, $r_\alpha = 0.5$, $\zeta_\alpha = \zeta_\xi = 0$, $\bar{\omega} = 0.2$, and free-play nonlinearity in pitch ($\delta = 0.5°, M_0 = M_f = 0, \alpha_f = 0.25°$) obtained using different time steps, $\Delta\tau$, in the time integration. The value in parentheses shows the relative error between the rms value in a column and that in the next column.

	$\Delta\tau = 0.1$	$\Delta\tau = 0.01$	$\Delta\tau = 0.001$
$U^*/U_L^* = 0.8$	0.8562 (6.42×10^{-5}%)	0.8562 (6.48×10^{-6}%)	0.8562
$U^*/U_L^* = 0.3$	0.5587 (5.07%)	0.5318 (0.18%)	0.5308

spectral density (PSD) plots obtained with three different time ranges (i.e. $t_f = 2 \times 10^4$, 3×10^4, and 4×10^4) are compared. Figs. 2.4(c,d) show PSD plots at $U^*/U_L^* = 0.8$ and $U^*/U_L^* = 0.3$, respectively. As seen, the PSD plots for the time ranges tested here are in good agreement with each other in terms of fundamental frequencies and amplitudes. This suggests that the simulation time range taken in this paper, i.e. $t_f = 3 \times 10^4$, is sufficiently large for obtaining reliable results.

2.2.1 Aeroelastic Behaviour of the System with Free-play Nonlinearity

Fig. 2.5 represents a 2-D physical model which is free to oscillate in pitch and plunge DOFs. The pitch DOF is provided by a bearing-supported shaft. This system, in turn, is suspended between a pair of leaf springs on either side of the test section, so that the entire mechanism is free to translate in plunge. In plunge DOF, the system is linear. The nonlinearity is introduced in the torsional (pitch) DOF as shown in the detail sketch. A leaf spring is clamped to the end of the torsion axis and its free end extends upward between two setscrews. The gap between the screws can be closed completely to give a linear torsion spring, or opened to provide any desired amount of angular free-play, giving the spring characteristic shown at the right of the Fig. 2.5 [5].

The behaviour investigation begins with comparing some results obtained from the present

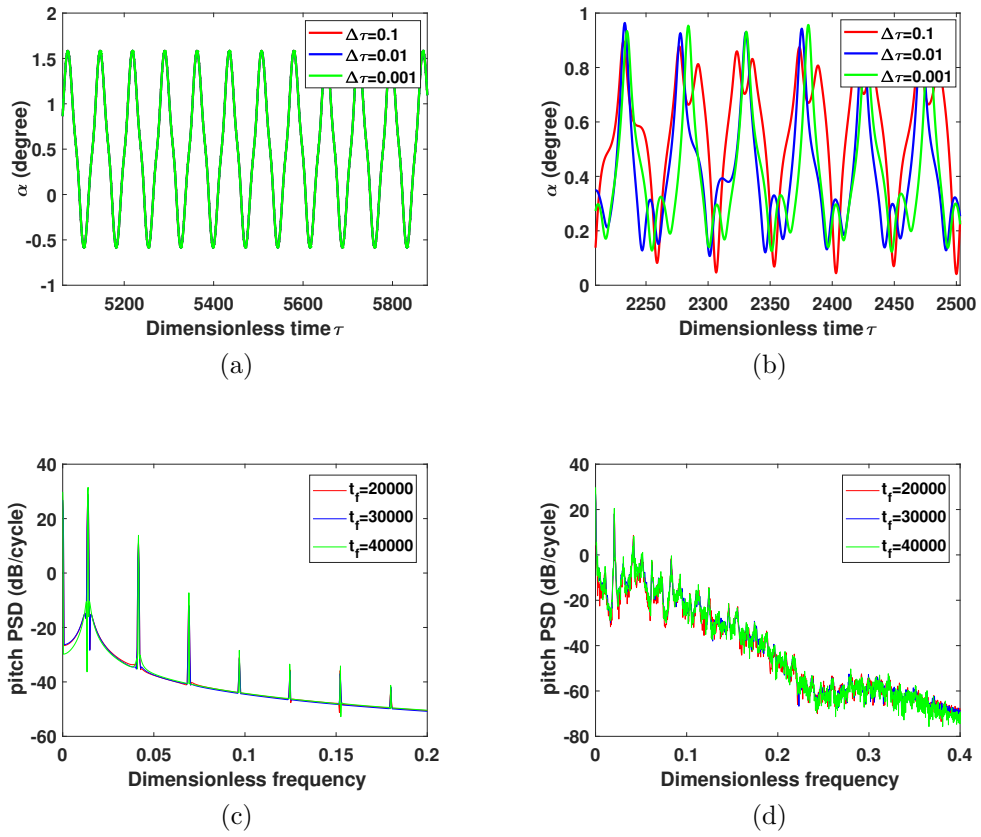

Figure 2.4: Numerical solution convergence study: (a,b) pitching motion amplitude versus dimensionless time obtained with three different time steps (i.e. $\Delta\tau = 0.1,\ 0.01,$ and 0.001) at $U^*/U_L^* = 0.8$ and $U^*/U_L^* = 0.3$, respectively; (c,d) PSD plots for the pitching motion obtained with three different time ranges (i.e. $t_f = 2\times10^4,\ 3\times10^4,$ and 4×10^4) at $U^*/U_L^* = 0.8$ and $U^*/U_L^* = 0.3$, respectively.

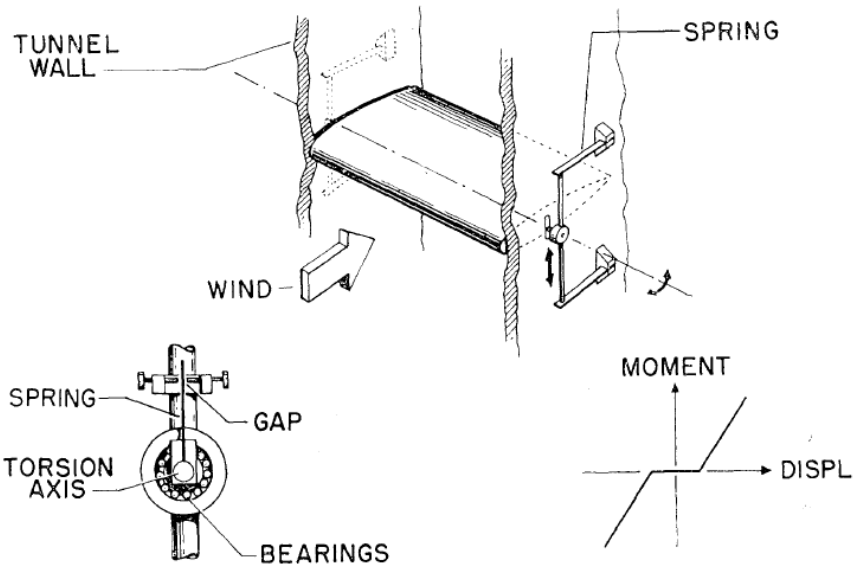

Figure 2.5: Free-play physical model (from [5]).

model with those available in the literature. The aeroelastic system is considered in [9, Fig. 11] to validate the model in the absence of gust. The system under consideration has a free-play pitching stiffness, where $\delta = 0.5°$, $M_0 = M_f = 0$, and $\alpha_f = 0.25°$; please see equation (2.3) and Fig. 2.2 for the definition of the parameters. The same initial conditions as in [9] have been considered: $\alpha_0 = 7$ deg and $\alpha_0' = 0$. Fig. 2.6 shows the bifurcation diagram where values of the pitch angle α when $\alpha' = 0$ are recorded and plotted against the normalized dimensionless airspeed, U^*/U_L^*.[1] The bifurcation diagram agrees exactly with Fig. 2.7, which is from [9, Fig. 11].

The rest of this section is devoted to the study of the typical dynamics of an aeroelastic system with free-play pitching stiffness. Although such studies already exist in the literature, as discussed in the Introduction, this chapter studies the dynamics of the system in more details, especially for plunge DOF, which is hardly found in the literature. In addition to bifurcation diagrams, the time history, phase-plane, PSD and Poincaré plots for both

[1]Please mind the difference in definition of parameters in Ref. [9] and here; U^* and U_L^* in this thesis are equivalent to U and U^* in Ref. [9], respectively.

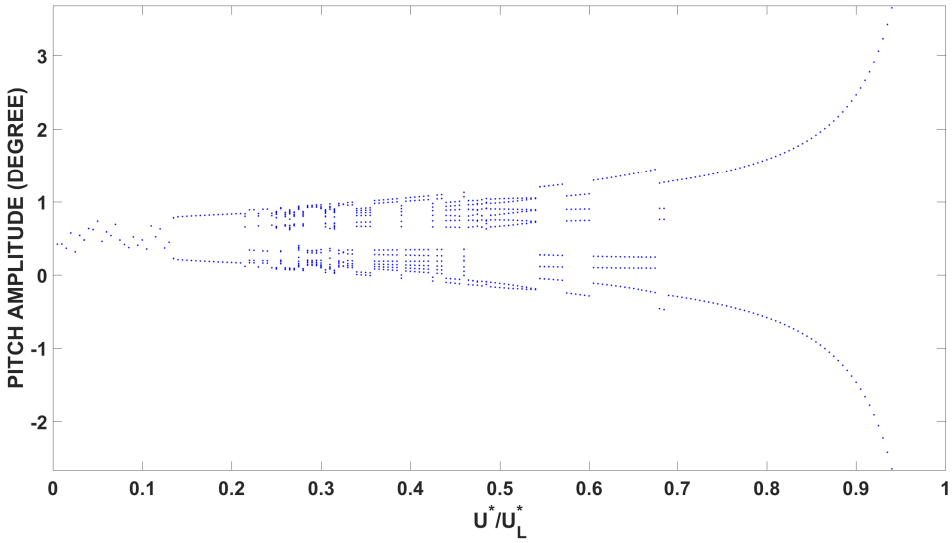

Figure 2.6: Bifurcation diagram for a system with the free-play nonlinearity in pitch ($\delta = 0.5°, M_0 = M_f = 0, \alpha_f = 0.25°$) for $\alpha_0 = 7°$ and $\alpha_0' = 0$, in which values of the pitch angle α are plotted when $\alpha' = 0$ as a function of the normalized dimensionless airspeed, U^*/U_L^* (cf. [9, Figure 11]).

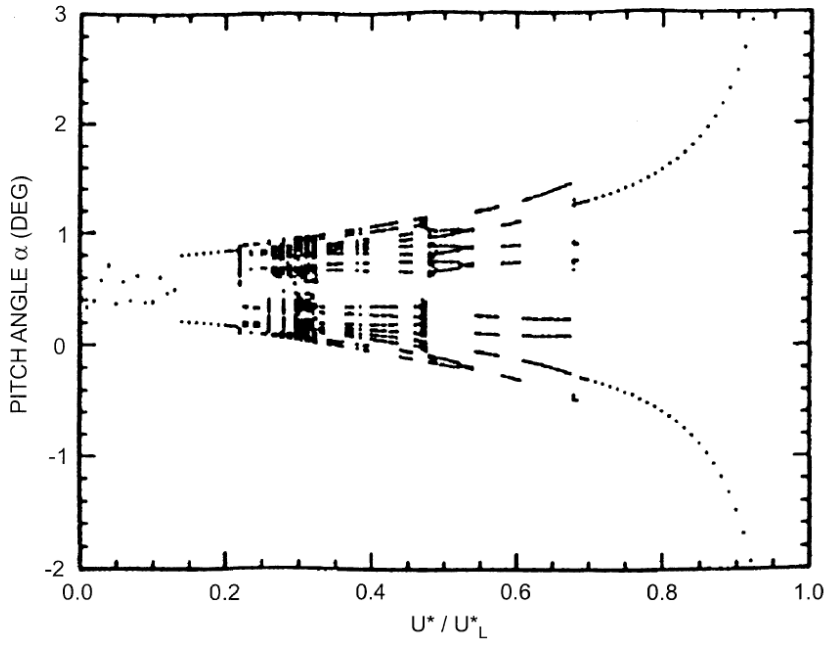

Figure 2.7: Bifurcation diagram for a system with the free-play nonlinearity in pitch ($\delta = 0.5°, M_0 = M_f = 0, \alpha_f = 0.25°$) for $\alpha_0 = 7°$ and $\alpha_0' = 0$, in which values of the pitch angle α are plotted when $\alpha' = 0$ as a function of the normalized dimensionless airspeed, U^*/U_L^* (from [9]).

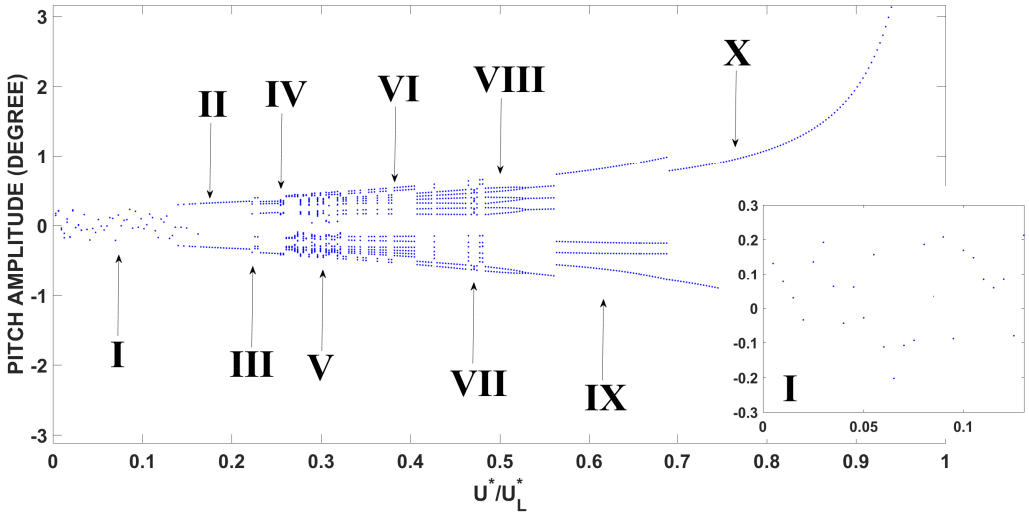

Figure 2.8: Bifurcation diagram for a system with free-play nonlinearity in pitch (airfoil 1: $\delta = 0.5°, M_0 = M_f = 0, \alpha_f = -0.25°$) for $\alpha_0 = 1°$ and $\alpha_0' = \xi = \xi_0' = 0$, in which values of the pitch angle α are plotted when $\alpha' = 0$ as a function of the normalized dimensionless airspeed, U^*/U_L^*. Different regions in the bifurcation diagram have been labelled from I to X. The inset to the right shows a magnified portion of region I. Table 2.2 should be consulted for the interpretation of the labels.

degrees of freedom are shown for several normalized dimensionless flow velocity. Moreover, the maximum Lyapunov exponent is calculated in order to actually determine the type of motion, especially when it is chaotic-like.

The dynamics of two airfoils which have different free-play parameters in the pitch DOF: $\delta = 0.5$ deg, $M_0 = M_f = 0$, $\alpha_f = -0.25$ deg (airfoil 1), and $\delta = 2$ deg, $M_0 = M_f = 0$, $\alpha_f = -1$ deg (airfoil 2) are examined. It is recalled that the linear flutter speed for this system is $U_L^* = 6.28$. In this section, the pitching initial conditions for bifurcation diagrams and time history results are set as: $\alpha_0' = \alpha'(0) = 0$, $\alpha_0 = \alpha(0) = 1$ deg.

Figs. 2.8 and 2.9 show the bifurcation diagrams for pitching and plunging motion of airfoil 1, respectively. Note that the inset to the right of the figure shows the enlarged region I. In the bifurcation diagrams presented in this thesis, a single dot represents a zero or a non-zero static equilibrium position (region I), and two dots represent period-1 motion (regions

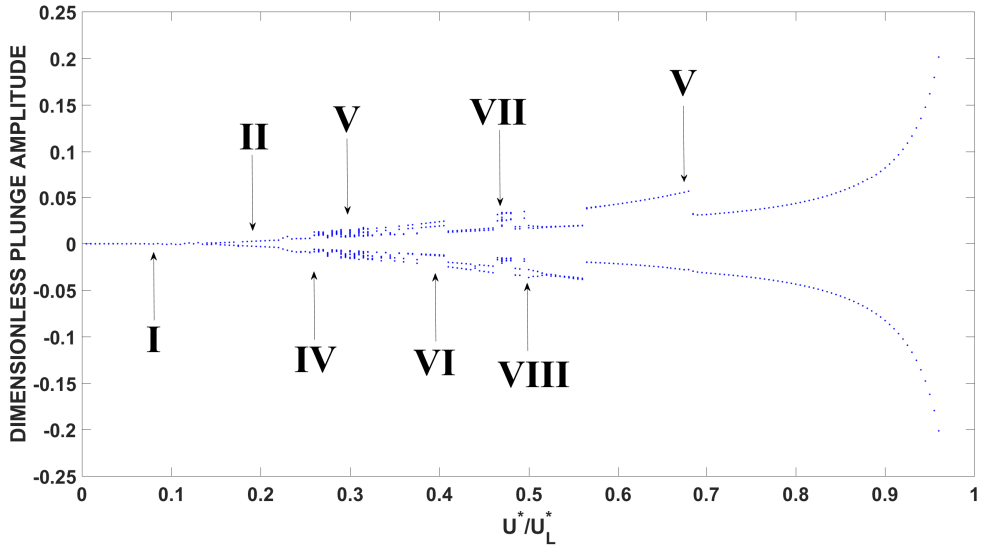

Figure 2.9: Bifurcation diagram for a system with free-play nonlinearity in pitch (airfoil 1: $\delta = 0.5°, M_0 = M_f = 0, \alpha_f = -0.25°$) for $\alpha_0 = 1°$ and $\alpha_0' = \xi = \xi_0' = 0$, in which values of the plunge ξ are plotted when $\xi' = 0$ as a function of the normalized dimensionless airspeed, U^*/U_L^*. Different regions in the bifurcation diagram have been labelled from I to X. Table 2.3 should be consulted for the interpretation of the labels.

II and X). Four dots should normally indicate period-2 motion (like regions IV, VI and VIII in Fig. 2.9); however, as discussed in the following paragraphs, for pitch DOF of the present dynamical system, they indicate period-1 with harmonics or in short, 'period-1-h' motion (regions III and IX in Figs. 2.8 and 2.10). Similarly, eight dots represent 'period-2-h' motion instead of standard period-4 motion (regions IV, VI and VIII in Figs. 2.8 and 2.10), and finally, multiple scattered dots suggest chaotic motion (regions V and VII).

As seen from Fig. 2.8, and especially from the inset, only a single dot is seen at a given value of U^*/U_L^* in the low flow velocity range. This indicates that the airfoil remains dynamically stable, where initial disturbances due to initial conditions are damped out after some time, and the pitch angle reaches either zero or a small non-zero value. Hence, the static equilibrium position for two consecutive velocity points may be very much different; such a behaviour have also been observed previously; see, for example, [9]. However, at

Table 2.2: Dynamical behaviour in different regions of the pitch bifurcation diagram shown in Fig. 2.8.

Region	$U^*/U_L^{*\ddagger}$	**Type of motion**
I	(0 0.135)	Static Equilibrium
II and X	(0.136 0.219) and (0.689 1)	Period-1
III and IX	(0.220 0.248) and (0.530 0.688)	Period-1-h
IV, VI and VIII	(0.249 0.252) (0.328 0.466) and (0.485 0.529)	Period-2-h
V and VII	(0.253 0.327) and (0.467 0.484)	Chaos

‡ U^*/U_L^* is the normalized dimensionless airspeed

Table 2.3: Dynamical behaviour in different regions of the plunge bifurcation diagram shown in Fig. 2.9.

Region	U^*/U_L^*	**Type of motion**
I	(0 0.135)	Static Equilibrium
II and X	(0.136 0.248) and (0.530 1)	Period-1
IV, VI and VIII	(0.249 0.252) (0.328 0.466) and (0.485 0.529)	Period-2
V and VII	(0.253 0.327) and (0.467 0.484)	Chaos

$U^*/U_L^* = 0.136$ the airfoil loses stability via a Hopf bifurcation leading to period-1 LCO. Soon after, the system regains stability (as indicated by a single dot) but loses it again at a slightly higher flow velocity. This switching between stability and instability is observed until $U^*/U_L^* = 0.138$ from which the motion remains period-1. At a higher flow velocity, i.e. $U^*/U_L^* = 0.220$, period-1 motion becomes period-1-h and soon after, at $U^*/U_L^* = 0.249$, it changes to period-2-h motion. At $U^*/U_L^* = 0.253$, motion becomes chaotic-like, but by further increasing the flow velocity, motion becomes period-2-h again. Switching from periodic to chaotic-like motion and from that back to periodic motion occurs between $U^*/U_L^* = 0.467$ and $U^*/U_L^* = 0.484$. Eventually, at $U^*/U_L^* = 0.689$ motion becomes period-1 once again through several inverse period-doubling bifurcations. Table 2.2 summarizes the different regions of the dynamical behavior and their boundaries as seen from the bifurcation diagram.

As also noted from Fig. 2.8, the pitch amplitude generally increases as the flow velocity

is increased, which is sensible since the aerodynamic loads become stronger as they are proportional to the flow velocity squared. As seen from the figure, in the region X, the pitch amplitude increases sharply with U^*/U_L^* and goes to very large values when $U^*/U_L^* > 1$ (not shown in the figure). This indicates the occurrence of divergent or violent flutter in that region; for more details, see Refs. [2, 5].

From Fig. 2.9 and Table 2.3, it is seen that the typical dynamical behavior of plunge DOF is relatively simpler than the one of pitch DOF, which can also be seen from the following dynamical figures. Most region boundaries are the same as the ones of pitch DOF. The main differences include that there is no period-1-h (regions III and IX) and the regions of period-2-h (regions IV, VI and VIII) for pitch DOF are the ones of period for plunge DOF.

Figs. 2.10 and 2.11 show, respectively, bifurcation diagrams for pitching motion and plunging motion of airfoil 2. It is noticed that, all the regions, except the region IV also materialize in the bifurcation diagrams for airfoil 2. Moreover, the same sequence of period-doubling bifurcations is observed for airfoil 2 although some regions are smaller or larger compared to those observed for airfoil 1. However, the pitching and plunging motion amplitudes for airfoil 2 are quite larger than those for airfoil 1, which may sound reasonable as δ and α_f for airfoil 2 are several times of those for airfoil 1. Note that the inset to the right of Fig. 2.11 shows the enlarged region VI, which shows the motion type in this region is period-2 more clearly. Tables 2.4 and 2.5 give the exact range for the different regions seen in Figs. 2.10 and 2.11, respectively.

The important message of the bifurcation diagrams shown in Figs. 2.8-2.11 is that the free-play nonlinearity may cause the system to lose the static equilibrium at a much lower flow velocity than the linear flutter speed; for example, for airfoil 1, the critical flow velocity was found to be $U_{NL}^* = 0.85$, while that for the linear system is $U_L^* = 6.28$. This indicates that the free-play stiffness nonlinearity may considerably reduce the critical flow velocity,

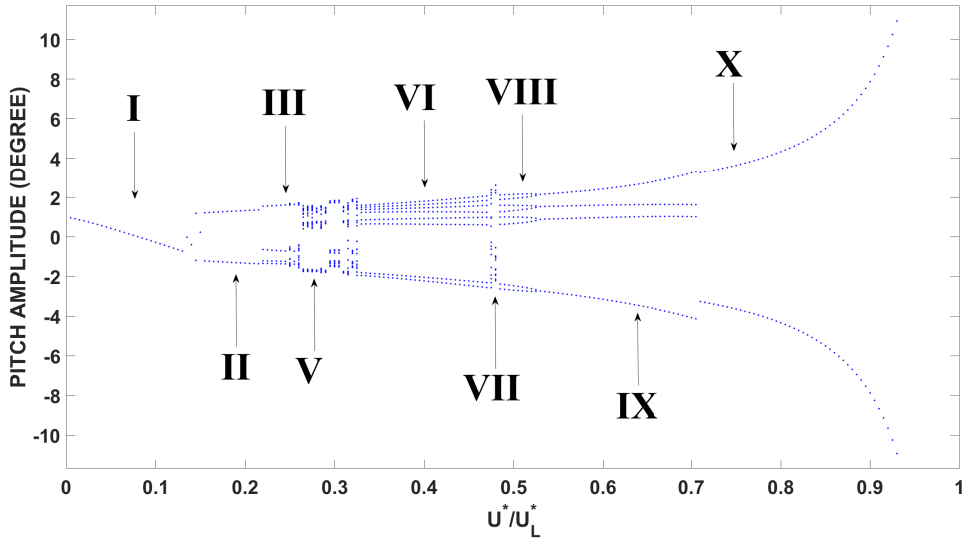

Figure 2.10: Bifurcation diagram for a system with free-play nonlinearity in pitch (airfoil 2: $\delta = 2^\circ, M_0 = M_f = 0, \alpha_f = -1^\circ$) for $\alpha_0 = 1^\circ$ and $\alpha_0' = \xi = \xi_0' = 0$, in which values of the pitch angle α are plotted when $\alpha' = 0$ as a function of the normalized dimensionless airspeed, U^*/U_L^*. Different regions in the bifurcation diagram have been labelled from I to X. Table 2.4 should be consulted for the interpretation of the labels.

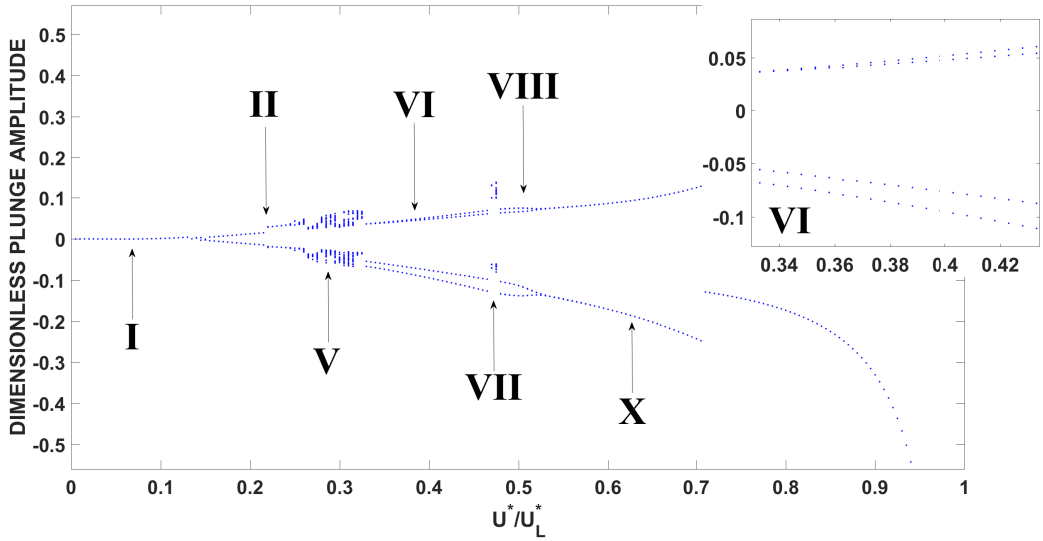

Figure 2.11: Bifurcation diagram for a system with free-play nonlinearity in pitch (airfoil 2: $\delta = 2^\circ, M_0 = M_f = 0, \alpha_f = -1^\circ$) for $\alpha_0 = 1^\circ$ and $\alpha_0' = \xi = \xi_0' = 0$, in which values of the plunge ξ are plotted when $\xi' = 0$ as a function of the normalized dimensionless airspeed, U^*/U_L^*. Different regions in the bifurcation diagram have been labelled from I to X. The inset to the right shows a magnified portion of region VI. Table 2.5 should be consulted for the interpretation of the labels.

Table 2.4: Dynamical behaviour in different regions of the pitch bifurcation diagram shown in Fig. 2.10.

Region	U^*/U_L^*	**Type of motion**
I	(0 0.141)	Static Equilibrium
II and X	(0.142 0.217) and (0.708 1)	Period-1
III and IX	(0.218 0.251) and (0.528 0.707)	Period-1-h
VI and VIII	(0.328 0.465) and (0.478 0.527)	Period-2-h
V and VII	(0.252 0.327) and (0.466 0.477)	Chaos

Table 2.5: Dynamical behaviour in different regions of the plunge bifurcation diagram shown in Fig. 2.11.

Region	U^*/U_L^*	**Type of motion**
I	(0 0.141)	Static Equilibrium
II and X	(0.142 0.251) and (0.528 1)	Period-1
VI and VIII	(0.328 0.465) and (0.478 0.527)	Period-2
V and VII	(0.252 0.327) and (0.466 0.477)	Chaos

as also observed by others, e.g. [2]. Thus, when such a nonlinearity is known to exist in the system, a nonlinear aeroelastic analysis has to be performed to actually determine the stability boundary of the system. In addition, the bifurcation diagrams suggest that for airfoils with the free-play type nonlinearity in the pitch DOF, the route to chaos is via period-doubling.

In the rest of this section, the numerical results obtained for airfoil 2 are discussed. Fig. 2.12 shows the time history, PSD, phase-plane, and Poincaré plots for $U^*/U_L^* = 0.8$ which lies in the region X in Figs. 2.10 and 2.11. The sinusoidal-like time history (Fig. 2.12(a)), the existence of a main frequency with its harmonics (Fig. 2.12(b)), the single-loop phase-plane plot (Fig. 2.12(c)) and one dot in the Poincaré map (Fig. 2.12(d)) all confirm a period-1 LCO for pitch DOF at $U^*/U_L^* = 0.8$. The motion of plunge has the same dynamical feature, so plunge DOF behaves period-1 LCO as well. It is noted that the Poincaré section maps presented here were obtained, similarly to Ref. [52], using an internal clock as the system is autonomous: α and α' were recorded at those times when $\xi' = 0$ and $\xi < \bar{\xi}$ (the mean value

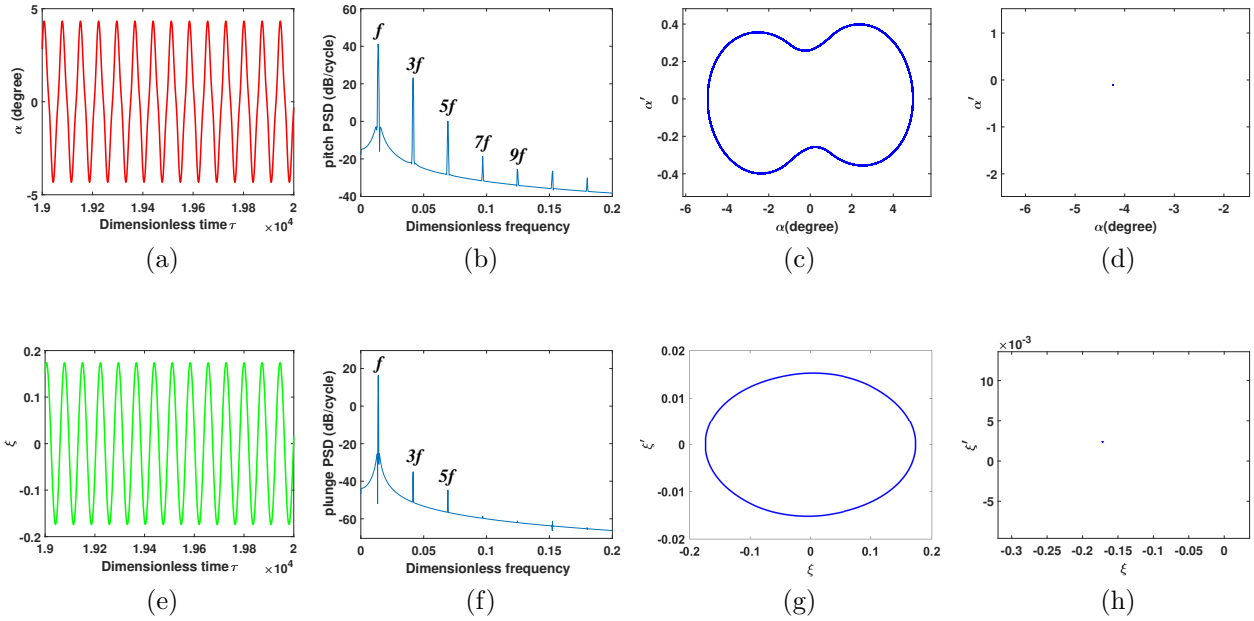

Figure 2.12: The dynamics of the system with free-play nonlinearity in pitch (airfoil 2) at $U^*/U_L^* = 0.8$ (region X in Fig. 2.10 and Fig. 2.11) where period-1 motion is observed: (a-d) time history, PSD, phase-plane, and Poincaré plots, respectively, for the pitch DOF, α, and (e-h) time history, PSD, phase-plane, and Poincaré plots, respectively, for the plunge DOF, ξ.

of plunge displacement); ξ and ξ' were recorded at those times when $\alpha' = 0$ and $\alpha < \bar{\alpha}$ (the mean value of pitch displacement).

At $U^*/U_L^* = 0.56$ which lies in the region IX in Fig. 2.10 and region X in Fig. 2.11, as discussed previously, for pitch DOF, period-2 motion is expected, and the appearance of a double-loop in the phase-plane plot in Fig. 2.13(c) may also be viewed as a confirmation of that. Nevertheless, no sub-harmonic of the main frequency, f, is seen in the PSD plot shown in Fig. 2.13(b); instead, harmonics of f, i.e. nf $(n = 2, 3, \cdots)$, are observed. Also, there is only one dot in the corresponding Poincaré map shown in Fig. 2.13(d). This motion of pitch DOF may thus be labelled as period-1-h or period-1 with harmonics, following the terminology adopted in [12]. Nevertheless, the motion of plunge is still period 1, as the dynamical features are similar with the ones at $U^*/U_L^* = 0.8$.

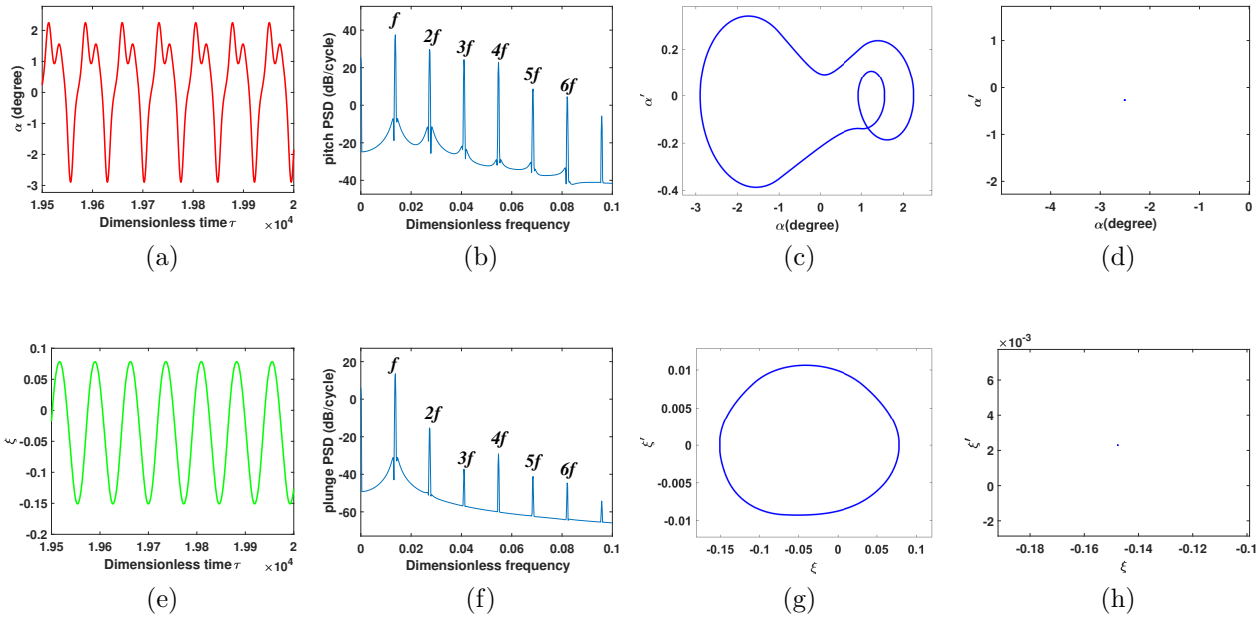

(a) (b) (c) (d)

(e) (f) (g) (h)

Figure 2.13: The dynamics of the system with free-play nonlinearity in pitch (airfoil 2) at $U^*/U_L^* = 0.56$ (region IX in Fig. 2.10 and region X in Fig. 2.11): (a-d) time history, PSD, phase-plane, and Poincaré plots, respectively, showing period-1-h motion for the pitch DOF, α, and (e-h) time history, PSD, phase-plane, and Poincaré plots, respectively, showing period-1 motion for the plunge DOF, ξ.

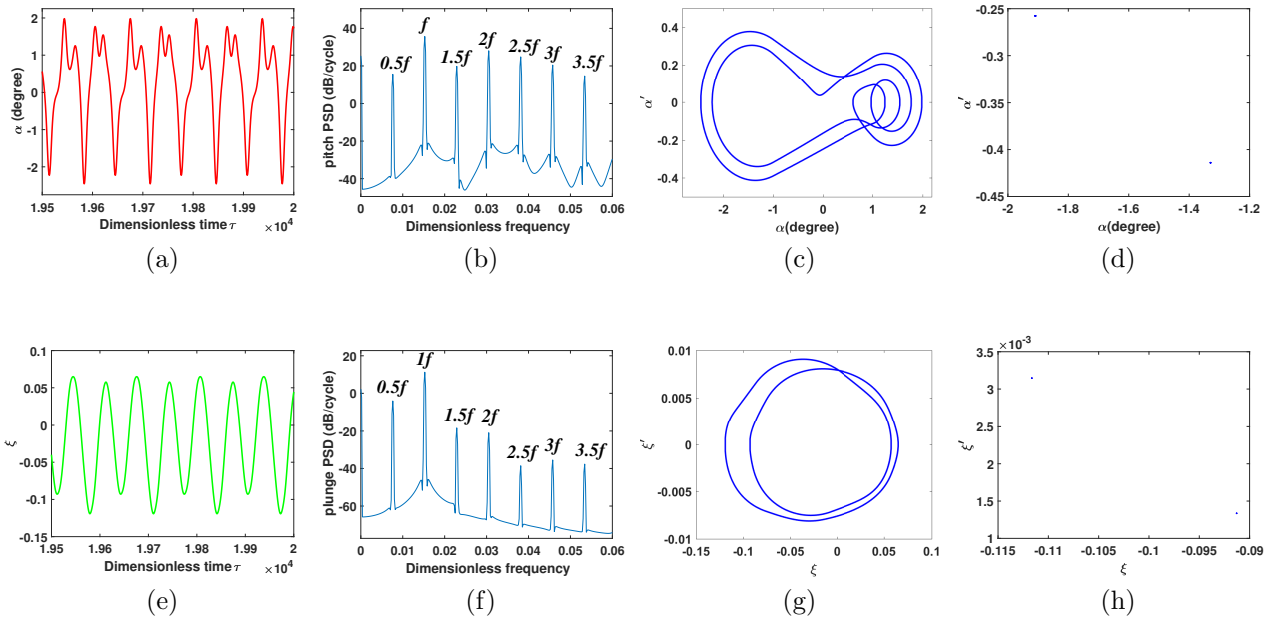

Figure 2.14: The dynamics of the system with free-play nonlinearity in pitch (airfoil 2) at $U^*/U_L^* = 0.45$ (region VI in Fig. 2.10 and Fig. 2.11): (a-d) time history, PSD, phase-plane, and Poincaré plots, respectively, showing period-2-h motion for the pitch DOF, α, and (e-h) time history, PSD, phase-plane, and Poincaré plots, respectively, showing period-2 motion for the plunge DOF, ξ.

At $U^*/U_L^* = 0.45$, period-4 motion in pitch DOF may be expected according to Fig. 2.14(c) which shows four closed loops. According to Fig. 2.14(d), however, there are only two dots in the Poincaré plot. Also, as seen from the PSD diagram in Fig. 2.14(b), there is only one subharmonic at $\frac{1}{2}f$, and the rest of the spectrum is dominated by harmonics of f as well as odd harmonics of $\frac{1}{2}f$. These suggest 'period-2-h' or period-2 with harmonics motion. While in plunge DOF, two closed loops in Fig. 2.14(g) and two dots in Fig. 2.14(h) both confirm a classical period-2 motion.

Finally, for pitch DOF, the erratic time history (Fig. 2.15(a)), relatively wide-banded frequency content in the PSD plot (Fig. 2.15(b)), the appearance of a 'two-well potential' in the phase-plane plot (Fig. 2.15(c)) and the distinct structure in the Poincaré map (Fig. 2.15(d)) all lend some evidence to existence of chaotic motion at $U^*/U_L^* = 0.3$ which lies

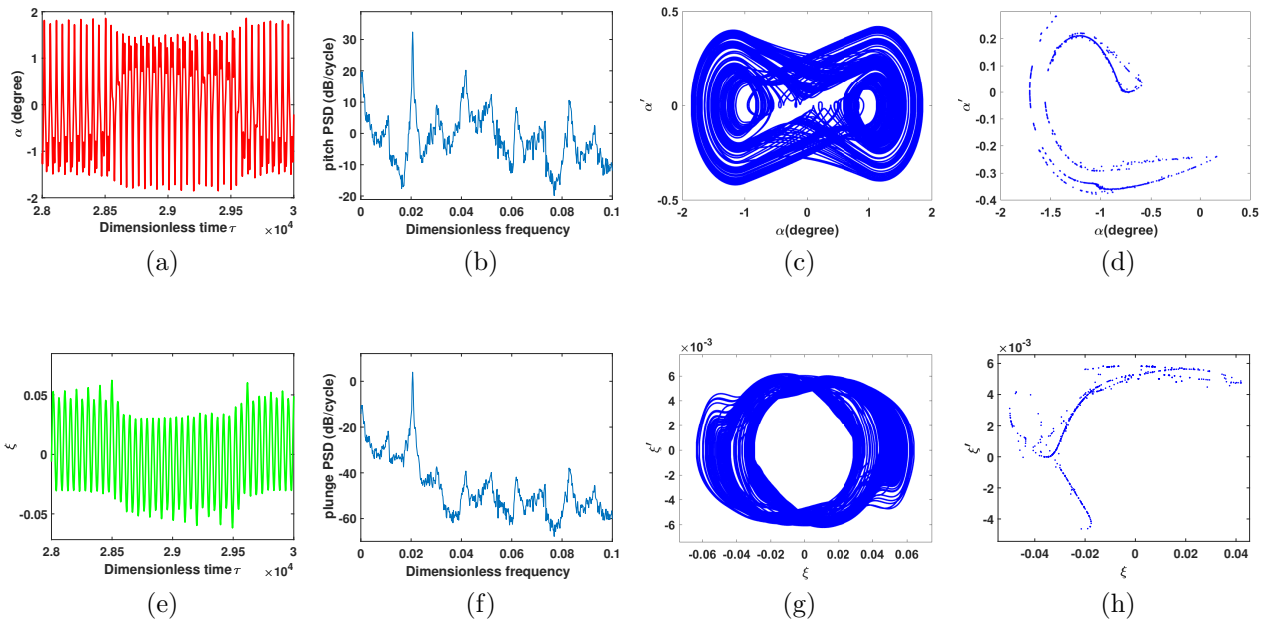

Figure 2.15: The dynamics of the system with free-play nonlinearity in pitch (airfoil 2) at $U^*/U_L^* = 0.3$ (region V in Fig. 2.10 in Fig. 2.11) where chaotic-like motion is observed: (a-d) time history, PSD, phase-plane, and Poincaré plots, respectively, for the pitch DOF, α, and (e-h) time history, PSD, phase-plane, and Poincaré plots, respectively, for the plunge DOF, ξ.

in the region V. To determine the type of motion at this flow velocity more definitely, a measure such as Lyapunov exponents should be sought. The dominant Lyapunov exponent is estimated from time series following the method of time delay reconstruction implemented by Wolf *et al.* [53]. The dominant Lyapunov exponent at several points lying in regions V and VII (e.g. U^*/U_L^*=0.27, 0.30, 0.32 and 0.47) was found to be between 0.01 to 0.02 bits/sec indicating that the system is 'mildly/weakly' chaotic. It should be noted that the dominant Lyapunov exponent was also calculated for multiple points in other regions in order to validate the bifurcation diagram predictions. For example, for $U^*/U_L^* = 0.45$ and $U^*/U_L^* = 0.56$ where period-2-h and period-1-h motions were predicted, respectively, the dominant Lyapunov exponent was found to be zero. For plunge DOF, the motion in regions V and VII is also determined by positive dominant Lyapunov exponent as chaotic.

2.2.2 Gust Response of the System with Free-play Nonlinearity

To validate the model that includes gust effects, the our numerical results are compared to those presented in Ref. [35]. Fig. 2.16 shows time history diagrams for an aeroelastic system ($U^* = 1,\ a = 0,\ x_\alpha = 0,\ r_\alpha = 0.5,\ \zeta_\alpha = \zeta_\xi = 0$) with two different combinations of mass ratio (μ) and frequency ratio ($\bar{\omega}$). Figs. 2.16(a,b) show, respectively, the variation of the normalized pitching and plunging amplitudes as a function of time for $\mu = 14,\ \bar{\omega} = 0.29$. On the other hand, Figs. 2.16(c,d) show the same quantities but for $\mu = 21,\ \bar{\omega} = 0.58$ (cf. [35, Figure 5]). It is noted that pitching and plunging amplitudes are normalized with respect to their steady-state values. These plots are exactly the same as Fig. 2.17, which is from [35].

Considering that the dynamical behavior of plunge DOF is simpler than that of pitch DOF when the nonlinearity is in pitch, as shown in Section 2.2.1, only the gust response of pitch DOF is shown in the rest of this section. The combined effects of a sharp-edged gust and pitching initial conditions on the response of airfoil 2 are given in Fig. 2.18. The figure shows the basin of attraction for different gust amplitudes at $U^*/U_L^* = 0.136$. A circle in the figure indicates the occurrence of a LCO, whereas a dot indicates static equilibrium. The probability of the occurrence of LCO may be obtained by calculating the density of circles in each plot, that is 100 $\times$ number of circles divided by the total number of grid points. The probability values are 76.5%, 78.6%, 81.7%, 86.2%, 91.9% and 95.5% for $w_0^* = 0,\ 0.018,\ 0.037,\ 0.055,\ 0.073,$ and 0.092 (i.e. $w_0 = 0,\ 0.1,\ 0.2,\ 0.3,\ 0.4,$ and 0.5 m/s), respectively. These results show that a stronger gust increases the probability of occurrence of LCO at a flow velocity close to the onset of the Hopf bifurcation.

As seen from Fig. 2.18(a), in the absence of the gust (i.e. $w_0 = 0$), the distribution of dots and circles is point symmetric. The dynamical behaviour of the system appears to be complex and sometimes unpredictable. Regions or 'islands' of static equilibrium or zero motion are observed for large values of α_0 and α_0', while a small initial pitch angle and a

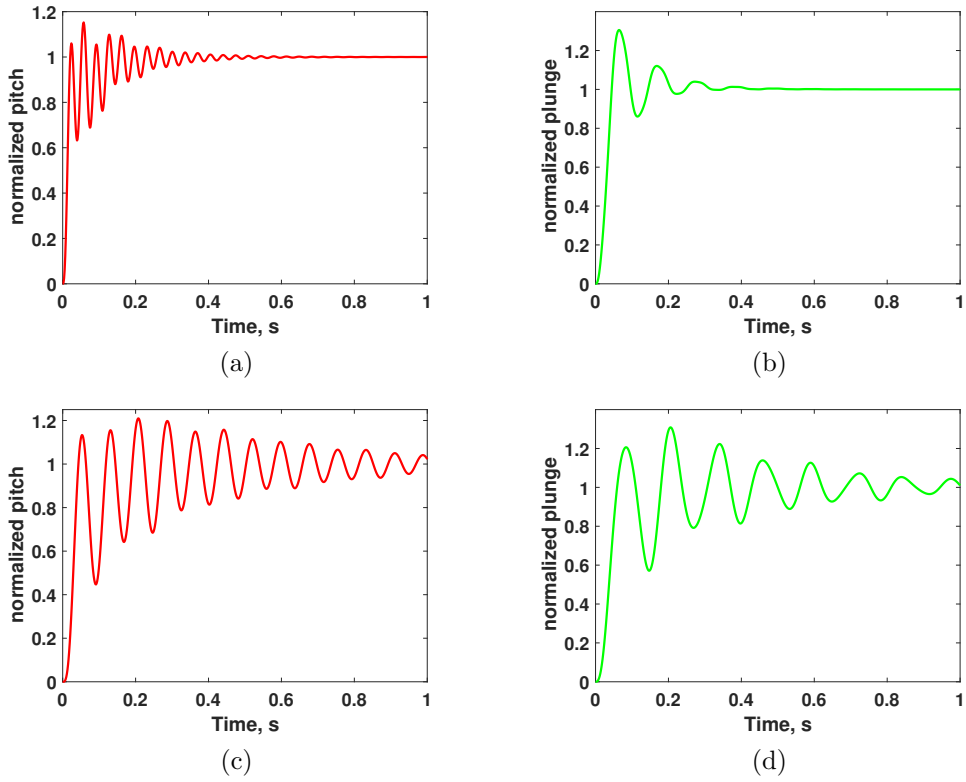

Figure 2.16: Time history plots for an aeroelastic system with $U^* = 1$ with $a = 0$, $x_\alpha = 0$, $r_\alpha = 0.5$, and $\zeta_\alpha = \zeta_\xi = 0$ under a sharp-edged gust input ($w_0 = 0.305$m/s): (a,b): $\mu = 14$, $\bar{\omega} = 0.29$ (cf. [35, Figure 4]), and (c,d): $\mu = 21$, $\bar{\omega} = 0.58$ (cf. [35, Figure 5]). Figures (a,c) show the variation of the pitch angle normalized with respect to the steady-sate value as a function of time, while figures (b,d) show the variation of normalized plunging amplitude as a function of time.

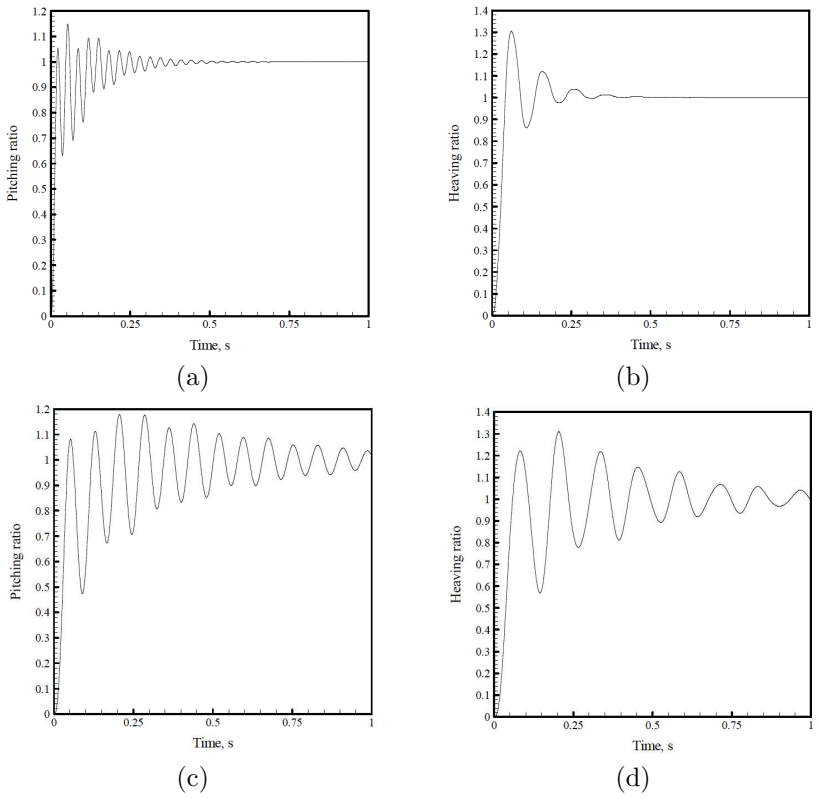

Figure 2.17: Time history plots (from [35]) for an aeroelastic system with $U^* = 1$ with $a = 0$, $x_\alpha = 0$, $r_\alpha = 0.5$, and $\zeta_\alpha = \zeta_\xi = 0$ under a sharp-edged gust input ($w_0 = 0.305$m/s): (a,b): $\mu = 14$, $\bar{\omega} = 0.29$ (from [35, Figure 4]), and (c,d): $\mu = 21$, $\bar{\omega} = 0.58$ (from [35, Figure 5]). Figures (a,c) show the variation of the pitch angle normalized with respect to the steady-sate value as a function of time, while figures (b,d) show the variation of normalized heaving (plunging) amplitude as a function of time.

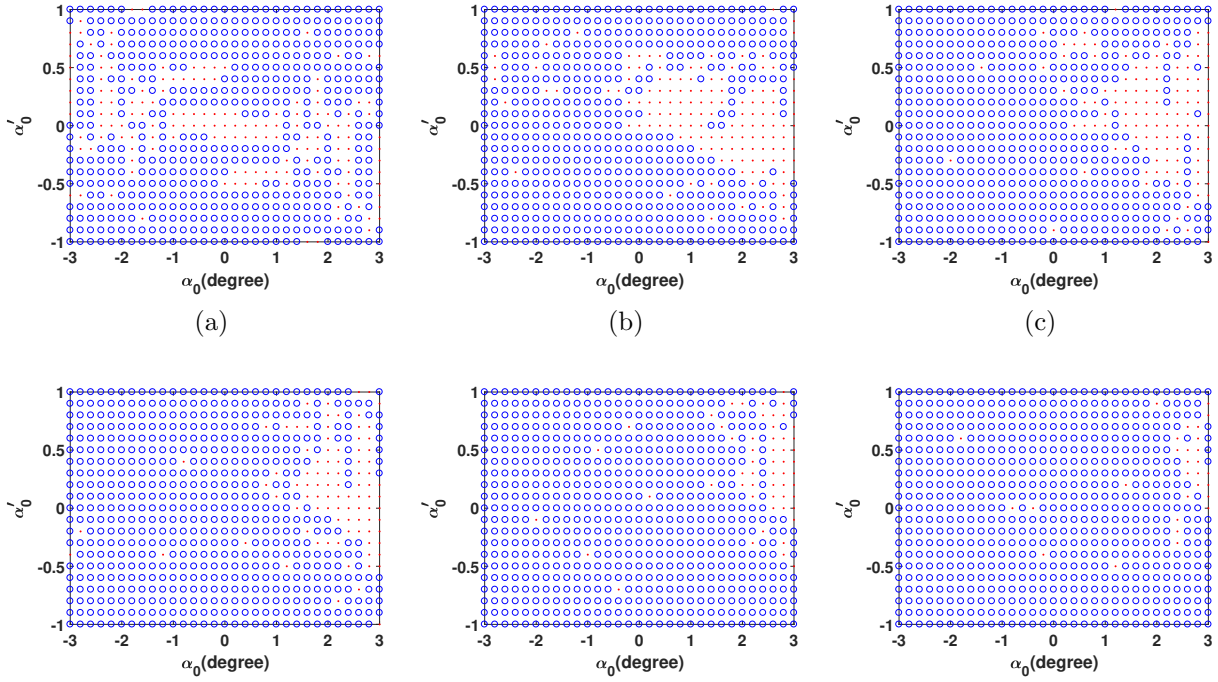

Figure 2.18: Basin of attraction at $U^*/U_L^* = 0.136$ for different amplitudes of sharp-edged gust (circle: LCO, dot: static equilibrium): (a) $w_0^* = 0$ ($P = 76.5\%$), (b) $w_0^* = 0.018$ ($P = 78.6\%$), (c) $w_0^* = 0.037$ ($P = 81.7\%$), (d) $w_0^* = 0.055$ ($P = 86.2\%$), (e) $w_0^* = 0.073$ ($P = 91.9\%$), and (f) $w_0^* = 0.092$ ($P = 95.5\%$), where P is the probability of the occurrence of LCO.

small pitch velocity may be sufficient to excite an LCO.

As seen from Figs. 2.18(b)-(f), the dynamical behaviour for systems excited by a sharp-edged gust becomes less complex compared to that with no gust. Regions of stability are more confined to large positive values of α_0, and this becomes more and more pronounced as the gust becomes stronger. It is also interesting to see from Figs. 2.18(b)-(f) that for a positive gust amplitude, which induces a positive angle of attack, the airfoil has a higher chance of becoming stable when $\alpha_0 > 0$. Conversely, as seen from Fig. 2.19, for a negative gust amplitude – a downward gust – the airfoil has a higher probability of stability when $\alpha_0 < 0$.

Fig. 2.20 shows the pitching response of the system to (a) a sharp-edged, and (b) a

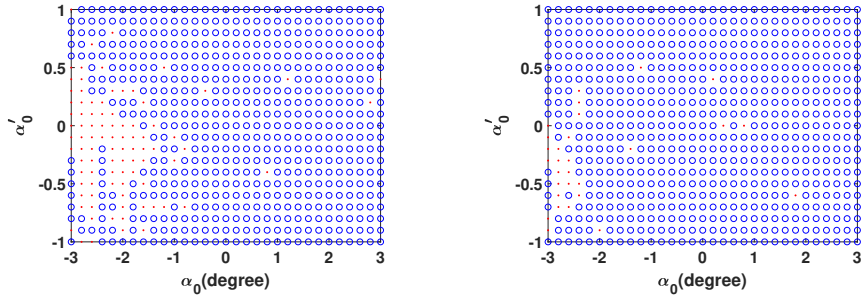

(a) (b)

Figure 2.19: Basin of attraction at $U^*/U_L^* = 0.136$ for different amplitudes of sharp-edged gust (circle: LCO, dot: static equilibrium): $w_0^* = -0.055$, (b) $w_0^* = -0.092$.

1-cosine gust at $U^*/U_L^* = 0.136$. Note that except for the plots of basin of attraction which are used to investigate the effects of different gust amplitudes, all the left gust amplitudes in this thesis are set as $w_0 = 10$ m/s. For comparison purposes, the time response in the presence of the gust is plotted on top of the time response in the absence of the gust. As seen, the system undergoes LCO under the gust input, while in the absence of the gust it regains static stability. In other words, a gust input causes the system to get 'attracted' to LCO at a lower airspeed – at $U^*/U_L^* = 0.136$ instead of 0.142.

Fig. 2.21 shows the time response at $U^*/U_L^* = 0.2$ which is a point in the region II in the bifurcation diagram shown in Fig. 2.10. As discussed, within this region, the airfoil section undergoes period-1 LCO in the absence of a gust. However, this changes to period-1-h LCO when the airfoil encounters a sharp-edged or a 1-cosine gust. Thus, the gust input may alter the type of response. In addition, it increases the amplitude of oscillation, especially in the transient part of the response.

Fig. 2.22 shows the time response at $U^*/U_L^* = 0.3$, where the motion is chaotic in the absence of a gust, lying in the region IV in Fig. 2.10. As seen, with the gust input, the pitching motion remains chaotic-like. Fig. 2.23 shows the time response at $U^*/U_L^* = 0.71$. Here also, the period-1 motion, which occurs in the gust absence, changes to a period-1-h

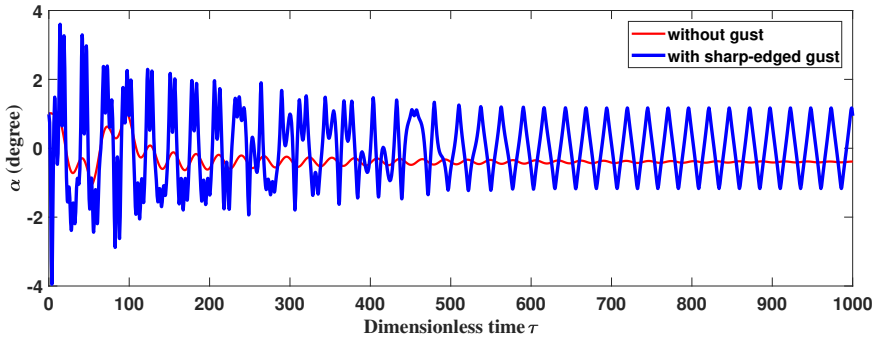

(a)

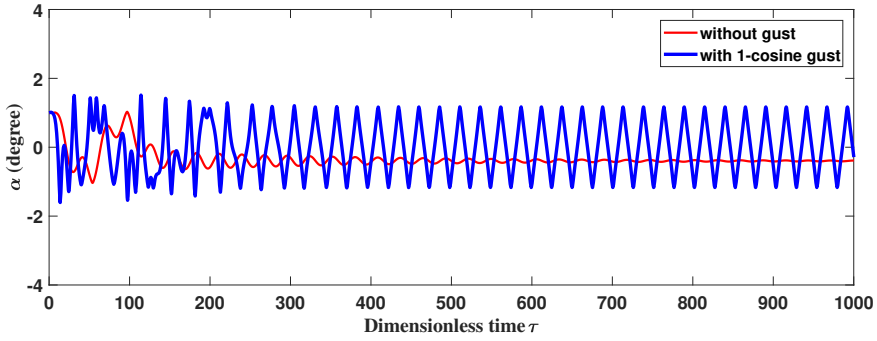

(b)

Figure 2.20: Gust response of airfoil 2 (heavy line; blue online) at $U^*/U_L^* = 0.136$, and $w_0^* = 1.83$ ($w_0 = 10$ m/s): (a) sharp-edged gust, and (b) 1-cosine gust. Light lines (red online) show the time response in the absence of gust.

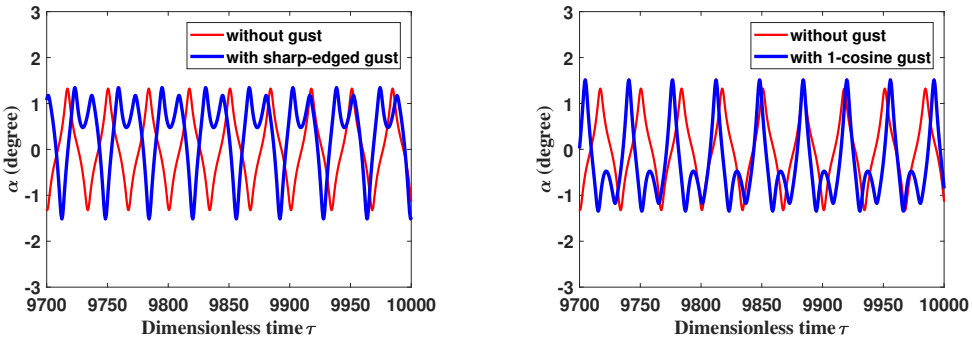

(a) (b)

Figure 2.21: Gust response of airfoil 2 (heavy line; blue online) at $U^*/U_L^* = 0.2$, and $w_0^* = 1.24$ ($w_0 = 10$ m/s): (a, c) sharp-edged gust, and (b, d) 1-cosine gust. Light lines (red online) show the time response in the absence of gust.

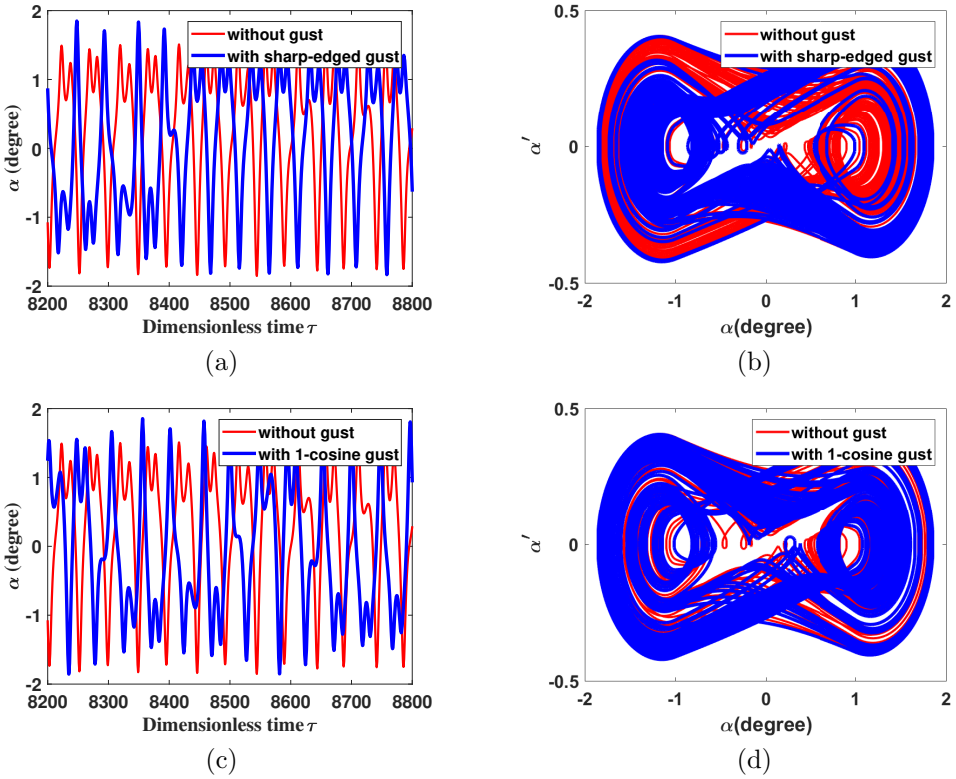

Figure 2.22: Gust response of airfoil 2 (heavy line; blue online) at $U^*/U_L^* = 0.3$, and $w_0^* = 0.83$ ($w_0 = 10$ m/s): sharp-edged (a, b), and 1-cosine (c, d). Light lines (red online) show the time response in the absence of gust.

motion due to the gust input. The increase of the amplitude of oscillation is also observed. These are more evident from Fig. 2.24 which shows the phase-plane plots for responses shown in Figs. 2.21(a) and 2.23(a).

Fig. 2.25 shows the time response at $U^*/U_L^* = 0.8$. Except for very large amplitudes due to gust effects in the transient part of the response, the responses with and without the gust input looks the same. Finally, as seen from Fig. 2.26, when U^* approaches U_L^*, the only difference between the time responses is that with the gust input the amplitude of LCO increases faster to very large values of the order of 23 deg. Such large pitch angles are beyond the stall angle of attack of most airfoils, where the linearity assumption of aerodynamic lift is violated, and thus the results for large values of U^*/U_L^* should be 'taken with a grain of

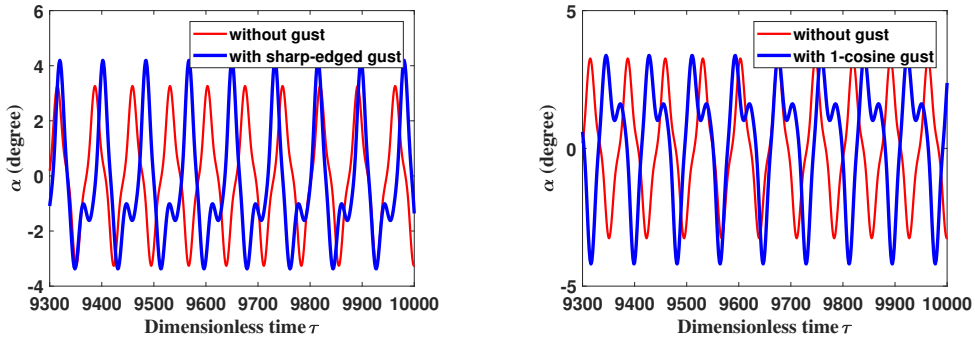

(a) (b)

Figure 2.23: Gust response of airfoil 2 (heavy line; blue online) at $U^*/U_L^* = 0.71$, and $w_0^* = 0.35$ ($w_0 = 10$ m/s): (a) sharp-edged gust, and (b) 1-cosine gust. Light lines (red online) show the time response in the absence of gust.

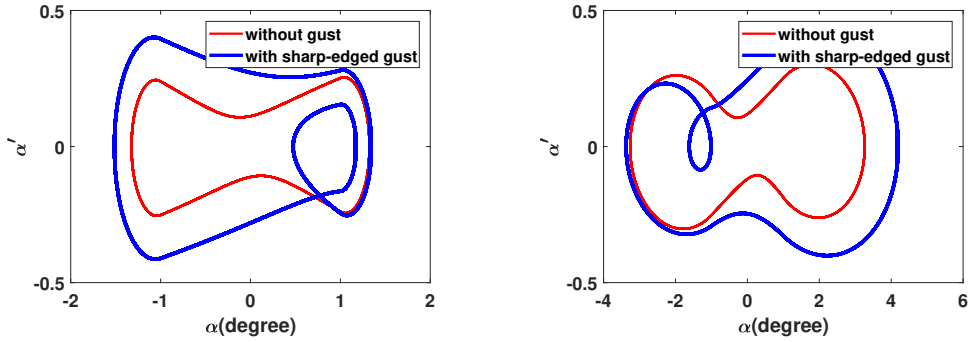

(a) (b)

Figure 2.24: Phase-plane plots of airfoil 2 with (heavy line; blue online) and without (light line; red online) a sharp-edged gust at: (a) $U^*/U_L^* = 0.2$ and $w_0^* = 1.24$ ($w_0 = 10$ m/s), and (b) $U^*/U_L^* = 0.71$ and $w_0^* = 0.35$ ($w_0 = 10$ m/s).

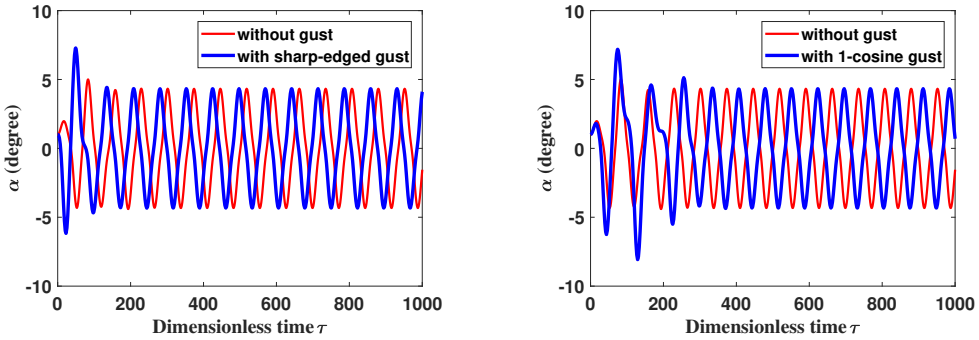

(a) (b)

Figure 2.25: Gust response of airfoil 2 (heavy line; blue online) at $U^*/U_L^* = 0.8$, and $w_0^* = 0.31$ ($w_0 = 10$ m/s): (a) sharp-edged gust, and (b) 1-cosine gust. Light lines (red online) show the time response in the absence of gust.

salt.'

2.2.3 Aeroelastic Behaviour of the System with Hysteresis Nonlinearity

When friction and backlash occur simultaneously, the nonlinearity usually exhibits a hysteresis feature. As force (or moment) is increased, displacement (or rotation angle) varies linearly until a certain point is reached at which a jump occurs, beyond which the system behaves linearly again. On the return path, a jump occurs at another value of the force, featuring a hysteresis loop. In the case of a wing, this type of nonlinearity may represent the effect of rivet slip [5].

In this section, we examine the dynamics of a system with hysteresis stiffness in the pitch DOF. The parameters are: $M_0 = 0.5$, $\delta = 1$ deg, $\alpha_f = 0$, and $M_f = 0$ (airfoil 3). Similarly to airfoils 1 and 2, the linear flutter speed for airfoil 3 is $U_L^* = 6.28$. Here, the initial conditions, except for basin of attraction plots, are set to be: $\alpha_0 = 1$ deg, and $\alpha_0' = 0.5$ deg/dimensionless time.

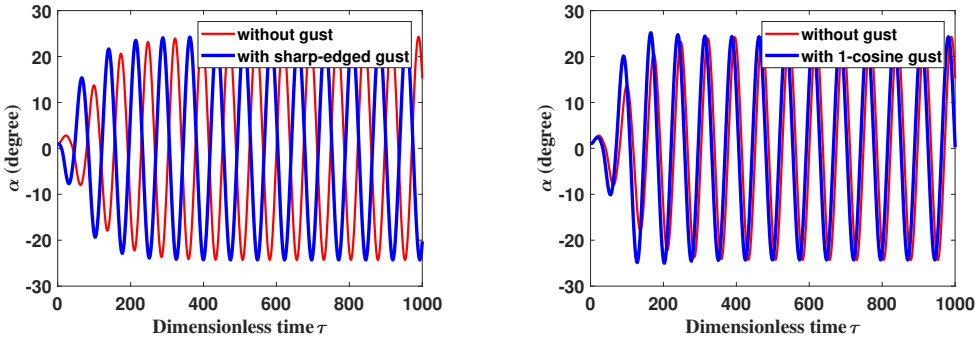

(a) (b)

Figure 2.26: Gust response of airfoil 2 (heavy line; blue online) at $U^*/U_L^* = 0.97$, and $w_0^* = 0.26$ ($w_0 = 10$ m/s): (a) sharp-edged gust, and (b) 1-cosine gust. Light lines (red online) show the time response in the absence of gust.

Figs. 2.27 and 2.28 show the bifurcation diagrams for free vibration (i.e. no gust input) of a typical airfoil section with hysteresis-type nonlinearity in the pitch and plunge DOFs, respectively. Compared to the dynamical behaviour shown in Figs. 2.8 to 2.11 for the system with free-play nonlinearity, the dynamics of the system with hysteresis nonlinearity seems much simpler. As seen, the system remains stable up to high flow velocities; however, it becomes unstable at $U^*/U_L^* = 0.799$ via a Hopf bifurcation leading to period-1 LCO for both pitch and plunge DOFs. No secondary bifurcations are observed at higher flow velocities. The amplitude of LCO increases sharply as the flow velocity is increased, which signifies the occurrence of divergent flutter – a similar behaviour was observed for the airfoil with free-play nonlinearity; see Section 2.2.1. Fig. 2.29 shows the time history, PSD, phase-plane, and Poincaré plots for both DOFs at $U^*/U_L^* = 0.85$, which all indicate period-1 motion.

2.2.4 Gust Response of the System with Hysteresis Nonlinearity

Fig. 2.30 shows the basin of attraction at $U^*/U_L^* = 0.85$ for different sharp-edged gust amplitudes. We consider stronger gusts, compared to those taken in Section 2.2.2, as here the flow

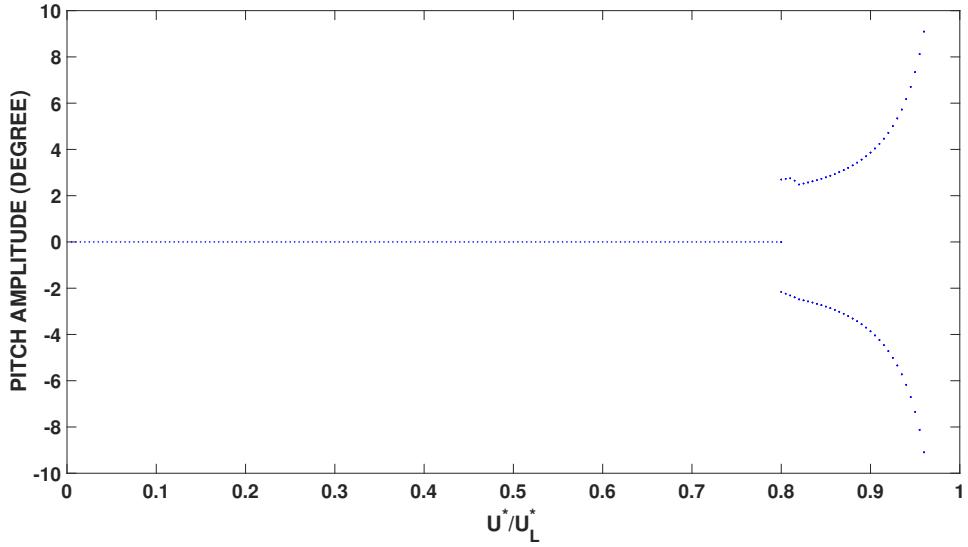

Figure 2.27: Bifurcation diagram for a system with the hysteresis nonlinearity in pitch (airfoil 3: $M_0 = 0.5, \delta = 1°$, $\alpha_f = 0, M_f = 0$) for $\alpha_0 = 1°$ and $\alpha_0' = 0.5°$/dimensionless time, in which the pitch angle α are plotted when $\alpha' = 0$ as a function of the normalized dimensionless airspeed, U^*/U_L^*.

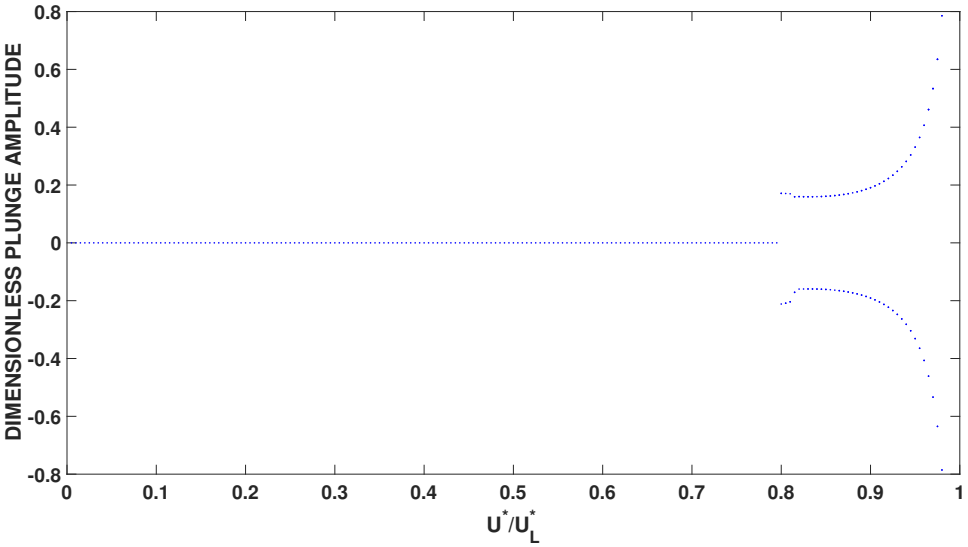

Figure 2.28: Bifurcation diagram for a system with the hysteresis nonlinearity in pitch (airfoil 3: $M_0 = 0.5, \delta = 1°$, $\alpha_f = 0, M_f = 0$) for $\alpha_0 = 1°$ and $\alpha_0' = 0.5°$/dimensionless time, in which the plunge ξ are plotted when $\xi' = 0$ as a function of the normalized dimensionless airspeed, U^*/U_L^*.

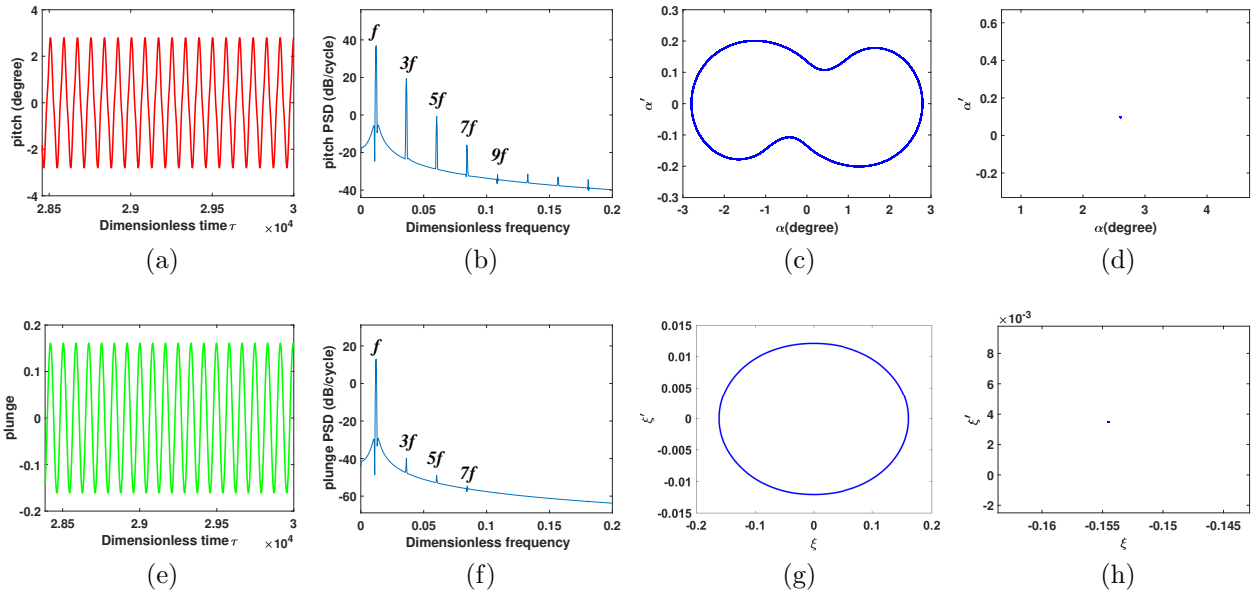

Figure 2.29: The dynamics of the system with hysteresis nonlinearity in pitch (airfoil 3) at $U^*/U_L^* = 0.85$ past the critical flow velocity where period-1 motion is observed: (a-d) time history, PSD, phase-plane, and Poincaré plots, respectively, for the pitch DOF, α, and (e-h) time history, PSD, phase-plane, and Poincaré plots, respectively, for the plunge DOF, ξ.

velocity at which the numerical results are obtained is much higher than that for the airfoil with free-play nonlinearity. As one can visually see from the sub-figures, the probability of the occurrence of LCO increases as the gust becomes stronger – the probability values are 39.6%, 41.0%, 43.6%, 51.5%, 62.3% and 64.1% for $w_0^* = 0,\ 0.031,\ 0.062,\ 0.093,\ 0.124,$ and 0.156 (i.e. $w_0 = 0,\ 1,\ 2,\ 3,\ 4,$ and 5 m/s), respectively. It is interesting to see from the plots that there are two finite bands (corresponding to the positive and negative values of α') between LCO regions, within which the system remains stable regardless of the value of α_0. From Fig. 2.30(a), it is also interesting to note that with no gust input, the distribution of dots and circles is point symmetric. Moreover, from Fig. 2.30(a)-(f), it is implied that the type of behaviour (i.e. stable or LCO) is more sensitive to the initial velocity (α_0') than the initial displacement (α_0).

Fig. 2.31 shows the time response of the airfoil to sharp-edged and 1-cosine gusts as well as that in the absence of the gust input at $U^*/U_L^* = 0.714$. In the absence of a gust, the system regains stability shortly after it is disturbed through the initial conditions, while with the gust input, the system is attracted to a period-1 LCO. When increasing U^*/U_L^* to 0.799, the time responses with and without the gust input becomes periodic with comparable amplitudes past the transition, as shown in Fig. 2.32. At $U^*/U_L^* = 0.85$, the time responses in the absence and presence of the gust becomes almost identical past the transition, as seen from Fig. 2.33. According to Figs. 2.32 and 2.33 and other results not shown here, past the Hopf bifurcation point, the disturbance due to the gust may only cause a phase difference in the response of the system, and except in the transient part, no obvious difference is observed between amplitudes in the time responses with and without the gust.

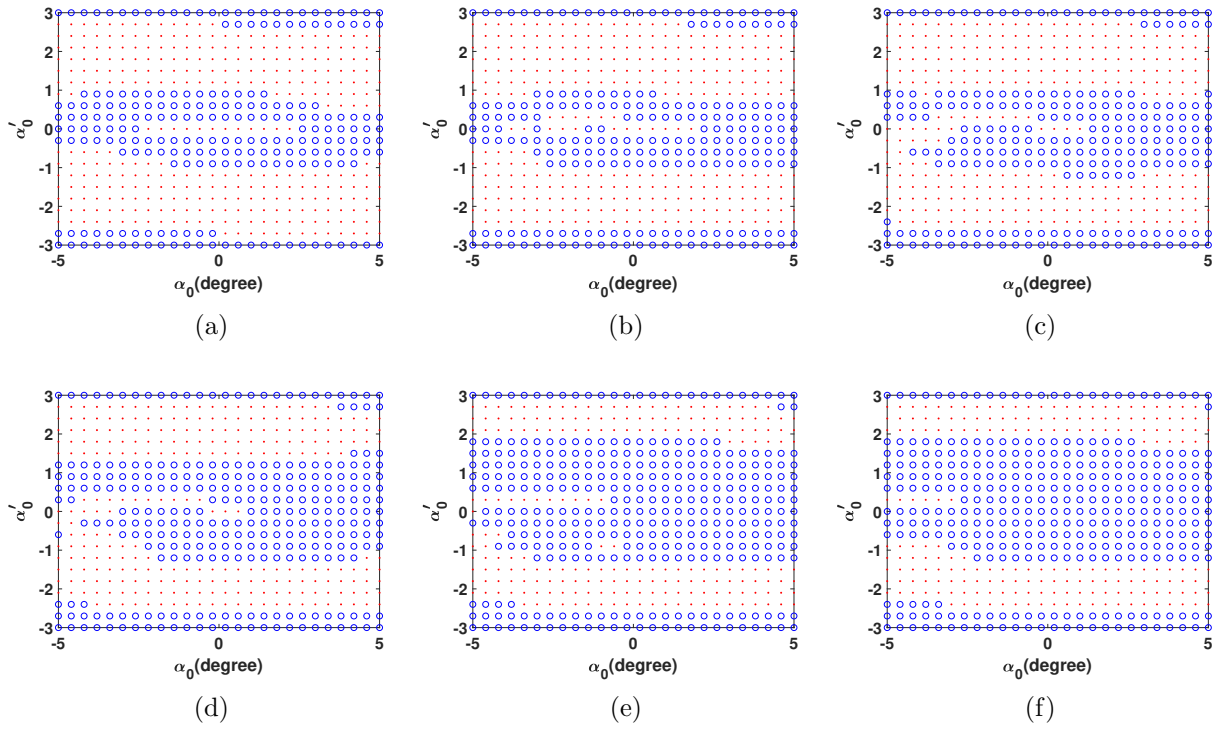

Figure 2.30: Basin of attraction at $U^*/U_L^* = 0.8$ for different amplitudes of sharp-edged gust (circle: LCO, dot: static equilibrium): (a) $w_0^* = 0$ ($P = 39.6\%$), (b) $w_0^* = 0.031$ ($P = 41.0\%$), (c) $w_0^* = 0.062$ ($P = 43.6\%$), (d) $w_0^* = 0.093$ ($P = 51.5\%$), (e) $w_0^* = 0.124$ ($P = 62.3\%$), and (f) $w_0^* = 0.156$ ($P = 64.1\%$), where P is the probability of the occurrence of LCO.

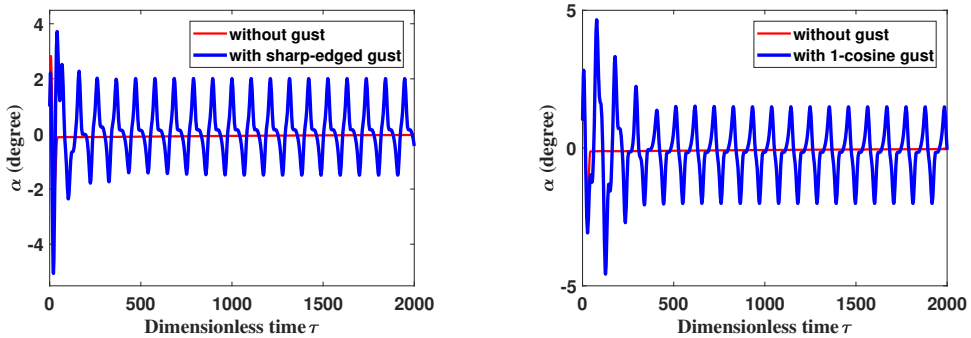

Figure 2.31: Gust response of airfoil 3 (heavy line; blue online) at $U^*/U_L^* = 0.714$, and $w_0^* = 0.35$ ($w_0 = 10$ m/s): (a) sharp-edged gust, and (b) 1-cosine gust. Light lines (red online) show the time response in the absence of gust.

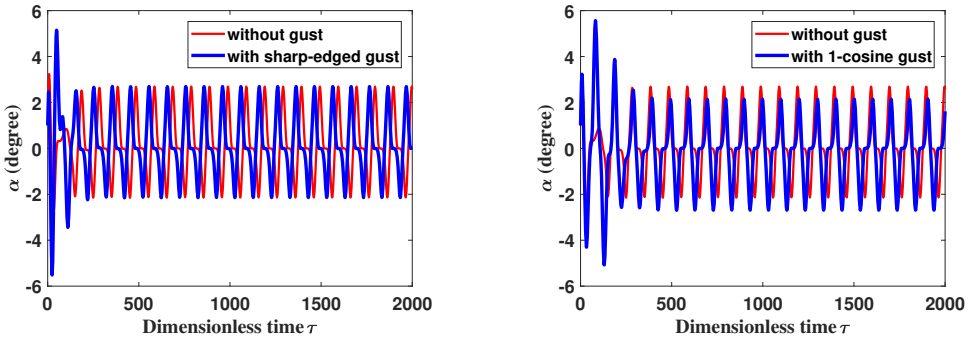

(a) (b)

Figure 2.32: Gust response of airfoil 3 (heavy line; blue online) at $U^*/U_L^* = 0.799$, and $w_0^* = 0.31$ ($w_0 = 10$ m/s): (a) sharp-edged gust, and (b) 1-cosine gust. Light lines (red online) show the time response in the absence of gust.

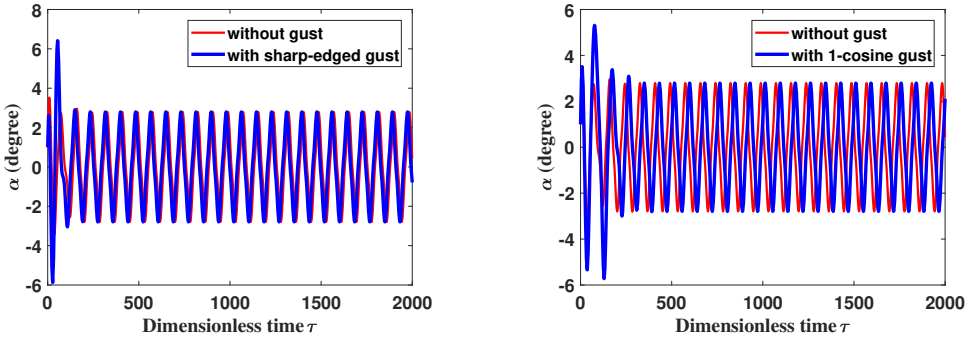

(a) (b)

Figure 2.33: Gust response of airfoil 3 (heavy line; blue online) at $U^*/U_L^* = 0.85$, and $w_0^* = 0.29$ ($w_0 = 10$ m/s): (a) sharp-edged gust, and (b) 1-cosine gust. Light lines (red online) show the time response in the absence of gust.

2.3 Summary

In this chapter, the typical dynamics characteristics for an airfoil with either a free-play or a hysteresis type of nonlinearity in the pitch DOF were presented. In addition, the responses of these systems to sharp-edged and 1-cosine gust profiles were examined. For the airfoil with the free-play nonlinearity, it was found that the stability may be lost through a Hopf bifurcation at a critical flow velocity significantly lower than that for the linear system. The post-critical dynamics of the system was found to be very complex, where motion may become chaotic through period-doubling bifurcations. Classical period-1 and period-2 motions were observed in plunge, while period-1 and period-2 with harmonics motions were observed in pitch. When there was no gust input, a complex but point-symmetric basin of attraction was found. However, when the airfoil was excited by the gust, the basin of attraction became relatively deterministic, where the region of stability became more confined to one side of the plot ($\alpha_0 > 0$ when the gust was in the positive direction and vice versa). It was also found that the probability of the occurrence of LCO increased as the gust became stronger.

For the airfoil with the hysteresis nonlinearity, the dynamics was found to be relatively simple, either in pitch or plunge DOF. The airfoil remained stable for a wide range of flow velocities but lost the stability via a Hopf bifurcation at a critical flow velocity comparable to the linear flutter speed. No secondary bifurcations were observed, and the amplitude of the LCO emanating from the Hopf bifurcation increased sharply with the flow velocity. It was found from the basin of attraction plots that there were two finite bands between regions of LCO, in which the stability was guaranteed independently from the value of the initial pitch angle.

From the results presented in this chapter, it may be concluded that studying the effects of time-dependent excitation due to atmospheric turbulence on the dynamics of nonlinear

lifting surfaces and designing control methods to mitigate those effects are essential for the design and operation of aircraft. These studies are particularly crucial for the design of new generation of aircraft, manned or unmanned, which are likely to be lighter, faster, more flexible, and more agile. In the next chapter, the control surface will be introduced to the wing model and there will be an extra DOF, which is flap.

Chapter 3

3-DOF Nonlinear Aeroelastic Model

By adding a control surface to the aeroelastic model mentioned in Chapter 2, an extra DOF (i.e. flap) is considered. This chapter is dedicated to the study of the typical dynamical behavior of a 3-DOF aeroelastic system with structural nonlinearities. Mode tracking method is employed to get the right trends of damping, and frequency as a function of flow velocity. For given system parameters, bifurcation diagrams are presented, and time-history, PSD, phase-plane and Poincaré diagrams are shown at different flow velocities.

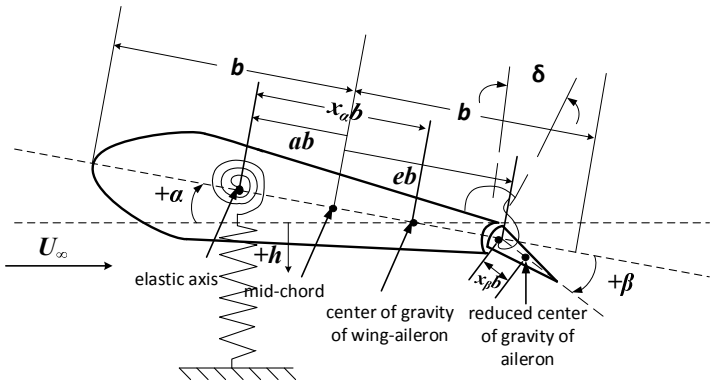

Figure 3.1: Schematic showing geometry of the wing section with three DOFs, i.e. pitch (α), plunge (h), and flap (β); b is the semi-chord.

3.1 Aeroelastic Modelling

Following the derivation in [14], the dimensionless aeroelastic equations for a two-dimensional wing with DOFs in plunge (ξ), pitch (α) and flap (β) may be written as [14] [1]

$$r_\alpha^2\ddot{\alpha} + [r_\beta^2 + (c-a)x_\beta]\ddot{\beta} + x_\alpha\ddot{\xi} + 2\zeta_\alpha\omega_\alpha\dot{\alpha} + r_\alpha^2\omega_\alpha^2 N_\alpha = \breve{M}, \tag{3.1}$$

$$[r_\beta^2 + (c-a)x_\beta]\ddot{\alpha} + r_\beta^2\ddot{\beta} + x_\beta\ddot{\xi} + 2\zeta_\beta\omega_\beta\dot{\beta} + r_\beta^2\omega_\beta^2 N_\beta = \breve{T}, \tag{3.2}$$

$$x_\alpha\ddot{\alpha} + x_\beta\ddot{\beta} + (m_{\text{tot}}/m)\ddot{\xi} + 2\zeta_\xi\omega_\xi\dot{\xi} + \omega_\xi^2 N_\xi = \breve{L}. \tag{3.3}$$

For a 3-DOF system, the structural stiffness for the pitch and plunge DOFs are typically of the cubic form, where the force exerted depends on the usual linear power of the displacement and, in addition, on a term containing the cube of the displacement. This can be considered either as a hard spring, which becomes stiffer as displacement increases, or as a soft spring, which becomes weaker as displacement increases. In the case of a structure, a hardening effect is found when a thin wing, or perhaps a propeller, is subjected to increasing amplitudes of torsion. A soft-spring effect may be associated with panel buckling [5]. Here, hard cubic

[1] It should be noted that in [14, equation(3)], h should be replaced by ξ.

stiffnesses are considered as:

$$N_\alpha = k_{1\alpha}\alpha + k_{3\alpha}\alpha^3, \tag{3.4}$$

$$N_\xi = k_{1\xi}\xi + k_{3\xi}\xi^3. \tag{3.5}$$

While in power-operated control systems and spring-tab systems, like the control surface hinge, the most common cause for nonlinear behavior is backlash. This produces a flat spot (free-play) nonlinearity which possesses a force-displacement characteristic in Fig. 2.2. For small displacements (free-play gap δ in Fig. 3.1), the spring offers no or small resistance to the movement of the control surface [2]. So the structural stiffness for the flap DOF is considered to be

$$N_\beta = \begin{cases} M_0 + \beta - \beta_f, & \text{for } \beta < \beta_f, \\ M_0 + M_f(\beta - \beta_f), & \text{for } \beta_f \le \beta \le \beta_f + \delta, \\ M_0 + \beta - \beta_f + \delta(M_f - 1), & \text{for } \beta > \beta_f + \delta, \end{cases} \tag{3.6}$$

where M_0 represents the preload, M_f is the stiffness in the free-play zone, β_f is the flap angle offset, and δ is the free-play range.

Expressions for the unsteady aerodynamic lift, L_a, pitching moment of the wing-flap system, M_a, and the pitching moment (torque) of the flap, T_a, are not repeated here for the sake of brevity; instead, they can be found in [14, 45]. Assuming $w_g(\tau)$ as the gust variable velocity and using Duhamel's integral, the lift, the pitching moment about the elastic axis, and the pitching moment about the flap hinge, in incompressible flow, due to penetration

into the gust, $L_g(\tau)$, $M_g(\tau)$, $T_g(\tau)$, respectively, may be written as [30, 45]:

$$L_g(\tau) = C_{L\alpha} b \rho_\infty U_\infty \int_0^\tau w_g(\tau_0) \frac{\partial \psi(\tau - \tau_0)}{\partial \tau} \mathrm{d}\tau_0, \tag{3.7}$$

$$M_g(\tau) = (1/2 + a) L_g(\tau), \tag{3.8}$$

$$T_g(\tau) = 0, \tag{3.9}$$

where $\psi(\tau)$ is the so-called Küssner function (for details, see Chapter 2).

To eliminate the integral terms in the expressions for aerodynamic and gust loading, the following eight new variables are introduced:

$$\begin{aligned}
w_1 &= \int_0^\tau e^{-b_1(\tau-\sigma)} \alpha(\sigma) \mathrm{d}\sigma, \;\; w_2 = \int_0^\tau e^{-b_2(\tau-\sigma)} \alpha(\sigma) \mathrm{d}\sigma, \\
w_3 &= \int_0^\tau e^{-b_1(\tau-\sigma)} \beta(\sigma) \mathrm{d}\sigma, \;\; w_4 = \int_0^\tau e^{-b_2(\tau-\sigma)} \beta(\sigma) \mathrm{d}\sigma, \\
w_5 &= \int_0^\tau e^{-b_1(\tau-\sigma)} \xi(\sigma) \mathrm{d}\sigma, \;\; w_6 = \int_0^\tau e^{-b_2(\tau-\sigma)} \xi(\sigma) \mathrm{d}\sigma, \\
w_7 &= \int_0^\tau e^{-b_3(\tau-\sigma)} \frac{w_g(\sigma)}{U_\infty} \mathrm{d}\sigma, \;\; w_8 = \int_0^\tau e^{-b_4(\tau-\sigma)} \frac{w_g(\sigma)}{U_\infty} \mathrm{d}\sigma,
\end{aligned} \tag{3.10}$$

in which constants b_1 and b_2 are from the well-known approximation for the Wagner function.

Using the new variables defined in Eq. (3.10) and the fact that $\partial(\;)/\partial t = (U_\infty/b)\partial(\;)/\partial\tau$,

Eqs. (3.1) to (3.3) may fully be rendered dimensionless:

$$A_1\alpha'' + A_2\beta'' + A_3\xi'' + A_4\alpha' + A_5\beta' + A_6\xi' + A_7\alpha + A_8\beta + A_9\xi + A_{10}N_\alpha + A_{11}w_1 + A_{12}w_2 + A_{13}w_3 + A_{14}w_4 + A_{15}w_5 + A_{16}w_6 + A_{17}w_7 + A_{18}w_8 = f(\tau), \tag{3.11}$$

$$B_1\alpha'' + B_2\beta'' + B_3\xi'' + B_4\alpha' + B_5\beta' + B_6\xi' + B_7\alpha + B_8\beta + B_9\xi + B_{10}N_\beta + B_{11}w_1 + B_{12}w_2 + B_{13}w_3 + B_{14}w_4 + B_{15}w_5 + B_{16}w_6 + B_{17}w_7 + B_{18}w_8 = g(\tau), \tag{3.12}$$

$$C_1\alpha'' + C_2\beta'' + C_3\xi'' + C_4\alpha' + C_5\beta' + C_6\xi' + C_7\alpha + C_8\beta + C_9\xi + C_{10}N_\xi + C_{11}w_1 + C_{12}w_2 + C_{13}w_3 + C_{14}w_4 + C_{15}w_5 + C_{16}w_6 + C_{17}w_7 + C_{18}w_8 = h(\tau). \tag{3.13}$$

The coefficients A_i, B_i, and C_i, $i = 1, 2, \ldots, 18$ are functions of the airfoil parameters, and their expressions can be found in [14, Appendix C], except for a few which are given as below:

$$\begin{aligned} &A_{10} = (\frac{r_\alpha^2}{U^*})^2,\ A_{17} = -(\frac{1}{2}+a)\frac{2}{\mu}s_3b_3,\ A_{18} = -(\frac{1}{2}+a)\frac{2}{\mu}s_4b_4,\\ &B_{17} = 0,\ B_{18} = 0,\\ &C_{10} = (\frac{\omega_\xi}{\omega_\alpha U^*})^2,\ C_{17} = -\frac{2}{\mu}s_3b_3,\ C_{18} = -\frac{2}{\mu}s_4b_4, \end{aligned} \tag{3.14}$$

in which $U^* = U_\infty/(b\omega_\alpha)$ is the dimensionless flow velocity, and $\mu = m/(\pi\rho b^2)$ being the mass ratio; also, $f(\tau)$, $g(\tau)$, and $h(\tau)$ may be written as

$$f(\tau) = \frac{-2(a+\frac{1}{2})}{\mu}[\xi(0) + (\frac{1}{2}-a)\alpha(0) + \frac{T_{11}}{2\pi}\beta(0)] \times (s_1b_1e^{-b_1\tau} + s_2b_2e^{-b_2\tau}), \tag{3.15}$$

$$g(\tau) = \frac{T_{12}}{\pi\mu}[\xi(0) + (\frac{1}{2}-a)\alpha(0) + \frac{T_{11}}{2\pi}\beta(0)] \times (s_1b_1e^{-b_1\tau} + s_2b_2e^{-b_2\tau}), \tag{3.16}$$

$$h(\tau) = \frac{2}{\mu}[\xi(0) + (\frac{1}{2}-a)\alpha(0) + \frac{T_{11}}{2\pi}\beta(0)] \times (s_1b_1e^{-b_1\tau} + s_2b_2e^{-b_2\tau}). \tag{3.17}$$

Finally, by introducing a variable vector $\mathbf{X} = (x_1,\ x_2, \cdots,\ x_{14})^T$ with $x_1 = \alpha,\ x_2 = \alpha',\ x_3 = \beta,\ x_4 = \beta',\ x_5 = \xi,\ x_6 = \xi',\ x_7 = w_1,\ x_8 = w_2,\ x_9 = w_3,\ x_{10} = w_4,\ x_{11} = w_5,\ x_{12} = w_6,\ x_{13} = w_7,\ x_{14} = w_8$, a set of 14 first-order ordinary differential equations written in the vector form can be obtained, as follows:

$$\mathbf{X}' = F(\mathbf{X}, \tau). \tag{3.18}$$

3.2 Typical Aeroelastic Behaviour

In this section, some numerical results are presented to illustrate the typical aeroelastic behaviour of the nonlinear system. Two different systems are studied, where they differ only in the pitching-plunging structural stiffness modelling. Both systems have free-play ($\delta = 2^\circ$) about the flap hinge (refer to Fig. 3.1), where the parameters are: $M_0 = M_f = 0,\ \beta_f = -1^\circ$. The first set is for a system (airfoil 4) with a linear pitching and a linear plunging stiffness ($k_{1\alpha} = 1,\ k_{1\xi} = 1$); the second set for a system (airfoil 5) with a linear plunging and a cubic pitching stiffness ($k_{1\alpha} = 1,\ k_{3\alpha} = 10,\ k_{1\xi} = 1$). The rest of system parameters are: $\mu = 26.47$, $a = -0.5$, $c = 0.5$, $x_\alpha = 0.33$, $x_\beta = 0.01789$, $r_\alpha = 0.814$, $r_\beta = 0.0947$, $m_{\text{tot}} = 3.625$ kg/m, $m = 1.73$ kg/m, $\omega_\xi = 4.39$ Hz, $\omega_\alpha = 8.012$ Hz, and $\omega_\beta = 16.187$ Hz, $\zeta_\xi = \zeta_\alpha = \zeta_\beta = 0.001$ [14]. The initial conditions are: $\xi_0 = 0$, $\alpha_0 = 1^\circ$, $\beta_0 = 0$, with their time derivatives equal to zero.

An aeroelastic stability analysis of aircraft structures can involve a large number of vibration modes, and mode crossing can occur during the analysis, complicating the interpretation of the results. The failure to track and correlate these mode crossings can cause misidentification of aeroelastic phenomena. The factors leading to flutter and divergence may be improperly understood and, therefore, attempts to make engineering decisions to improve

performance will be misguided and likely unsuccessful. Mode tracking methodologies establish correspondence among the set of point solutions generated at each discrete parameter increment of the aeroelastic analysis [54]. Fig. 3.2 shows damping and frequency diagrams with the application of the mode tracking technology, which shows the post-processing module succeeds in alleviating the severity of the mode switching [51]. The flutter speed is determined by these figures as $U_L^* = 5.455$, where U_L^* denotes the dimensionless flutter speed for the linear system, which agrees well with the experimental results in [14].

Fig. 3.3 shows the bifurcation diagram where maximum and minimum values (local and global) of the plunge, ξ, pitch angle, α, and flap angle, β, are plotted against the normalized dimensionless airspeed, (U^*/U_L^*). In the bifurcation diagrams, a single dot/point represents a static equilibrium position; two dots represent period-1 motion, four dots show period-2 motion or period-1-h and so on, and finally, multiple scattered dots may either indicate quasi-periodic or chaotic motion (for details, see Chapter 2). Fig. 3.4 shows the bifurcation diagram of a system with a linear plunging and a cubic pitching stiffness.

As seen from Fig. 3.3, the airfoil is stable for $(U^*/U_L^*) < 0.1$, and any disturbance is decayed to zero with time. However, the system loses its stable position, and it undergoes a Hopf bifurcation at $(U^*/U_L^*) \simeq 0.1$ leading to a period-1 LCO. The period-1 motion, however, quickly becomes period-1-h for the pitch and flap DOFs, while it remains period-1 for the plunge DOF. This behaviour lasts until $(U^*/U_L^*) \simeq 0.3$, where the motion becomes chaotic-like for a short range of flow velocity. It is then transformed into period-1 motion which remains dominant up to the maximum flow velocity investigated. For $(U^*/U_L^*) > 1$ (not shown here), the amplitudes for all DOFs increase sharply to very large values, indicating the occurrence of *divergent* or *violent* flutter. This phenomenon has been reported previously by several researchers, e.g., in [2, 36]. As seen from Fig. 3.4, the dynamical behaviour of airfoil 5 is very similar to that of airfoil 5. A few exceptions, however, exist. For example, for airfoil 5,

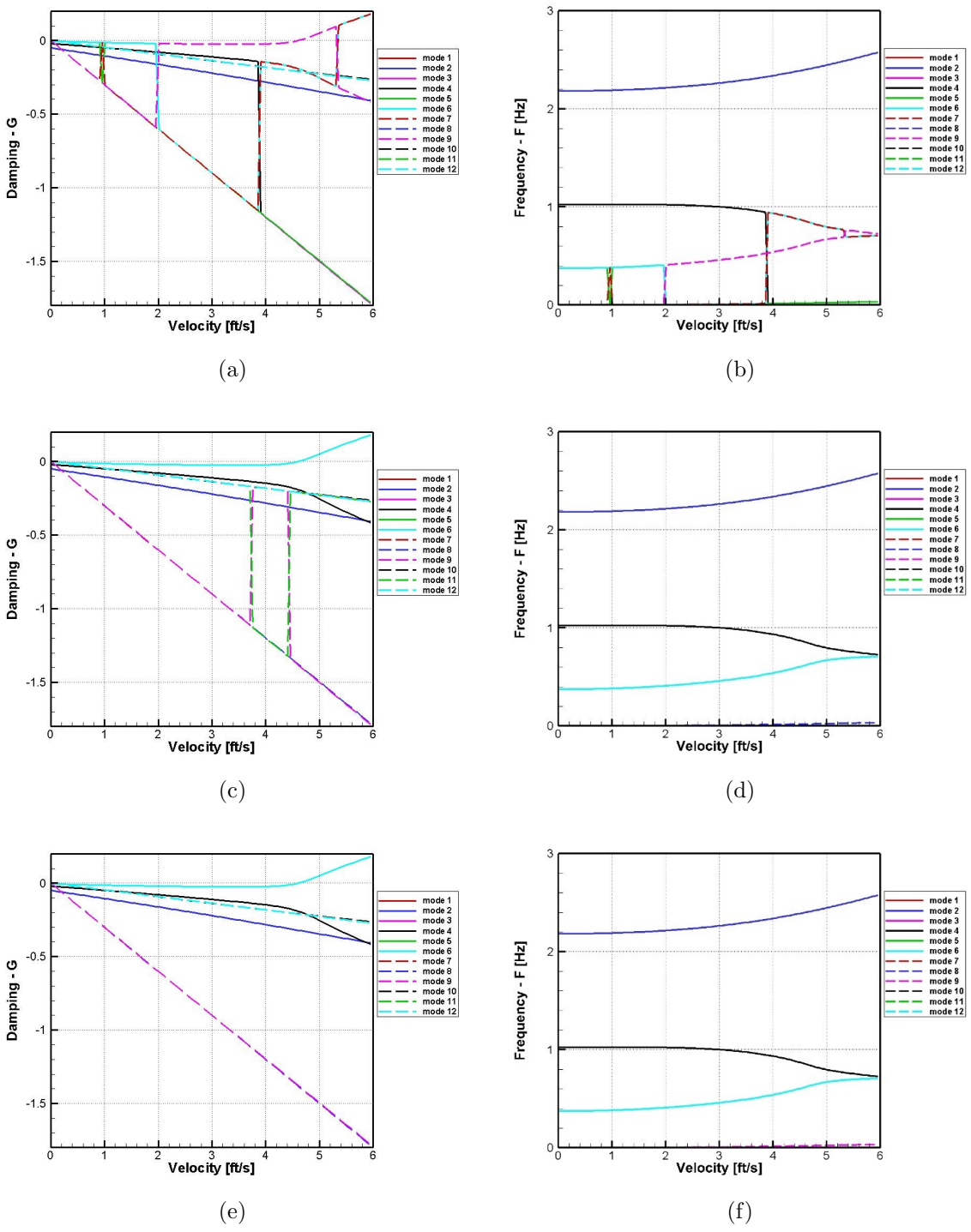

Figure 3.2: Damping (left) and frequency (right) diagrams with the application of the mode tracking technology.

beyond $(U^*/U_L^*) = 1.0$, the amplitudes gradually tend to increase to large values, most likely because of the self-limiting characteristic of the additional stiffness nonlinearity. It is also interesting to observe a period-3 flapping motion of the airfoil 5 airfoil for $(U^*/U_L^*) > 1.05$ (see Fig. 3.4, *right*). This phenomenon is, in fact, worthy of a further investigation in a future study.

Since the nonlinearities considered in this chapter are in the pitch and flap DOFs, so the dynamic results in this section are focused on these two DOFs as well. Fig. 3.5 shows the time-history, PSD, phase-plane, and Poincaré plots of airfoil 4 for the pitch and flap DOFs, respectively at $(U^*/U_L^*) = 0.17$. These plots confirm a period-1-h pitching and flapping motions (for details, see Chapter 2). Moreover, Fig. 3.6 shows the time-history, PSD, phase-plane, and Poncaré plots of airfoil 4 for the pitch and flap DOFs, respectively at $(U^*/U_L^*) = 0.30$. The appearance of a closed curve in the Poincaré maps as well as harmonics of two incommensurate frequencies in the PSD plots lend some evidence to the existence of quasi-periodic motion at this flow velocity.

3.3 Summary

The numerical results presented in this chapter show that structural nonlinearities may have significant effects on the dynamical behavior of the system. In particular, free-play about the flap hinge may cause the system to become unstable at a flow velocity well below the flutter speed of the linear system, U_L^*. The airfoil loses stability via a Hopf bifurcation for all three DOFs and the dynamics of the 3-DOF system with the free-play nonlinearity in flap may exhibit the phenomenon of quasi-periodic motion through period-doubling bifurcations, similar with the 2-DOF system mentioned in Chapter 2. The hard cubic stiffness has negligible effect effects on the dynamics of system within the linear flutter speed, but

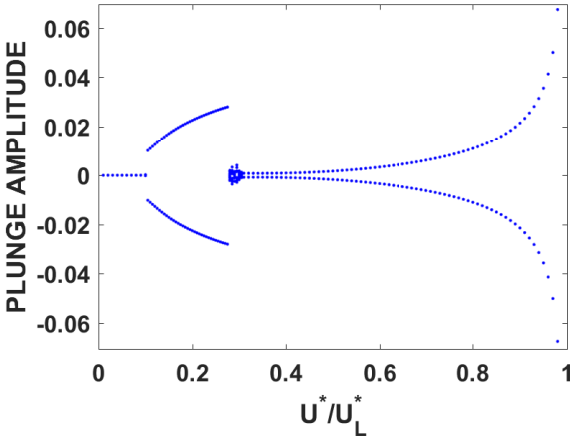

(a)

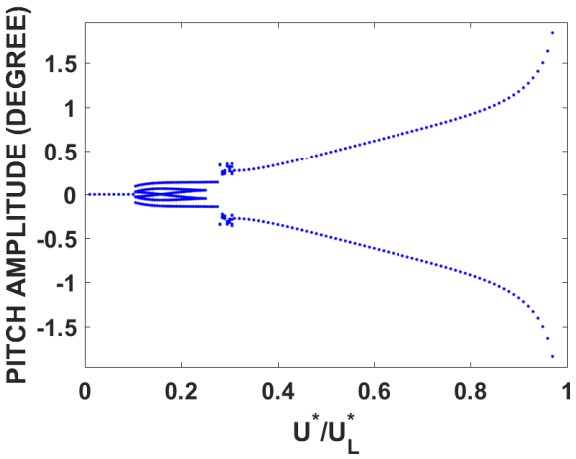

(b)

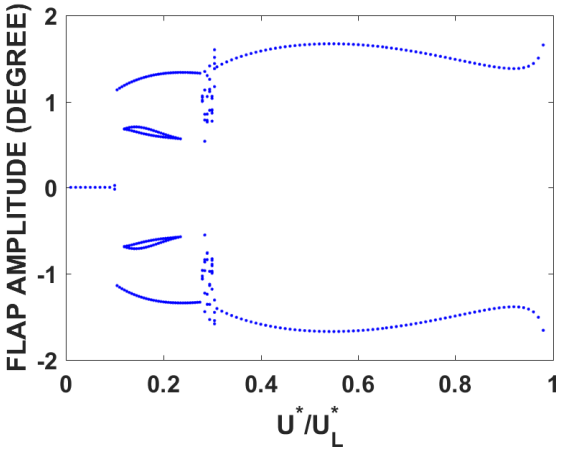

(c)

Figure 3.3: Bifurcation diagrams for (a) plunge, (b) pitch, and (c) flap DOFs, for a system with flap free-play and linear pitching and plunging stiffnesses (airfoil 4).

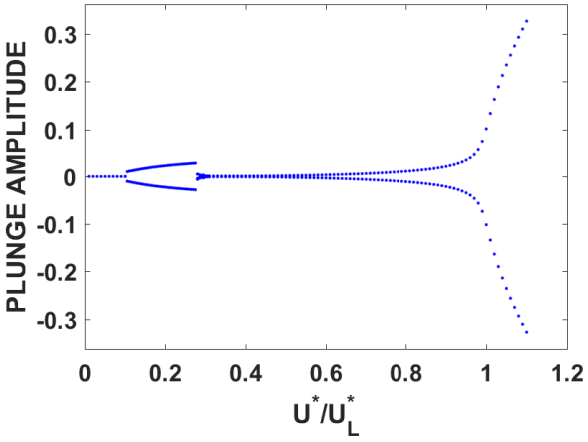

(a)

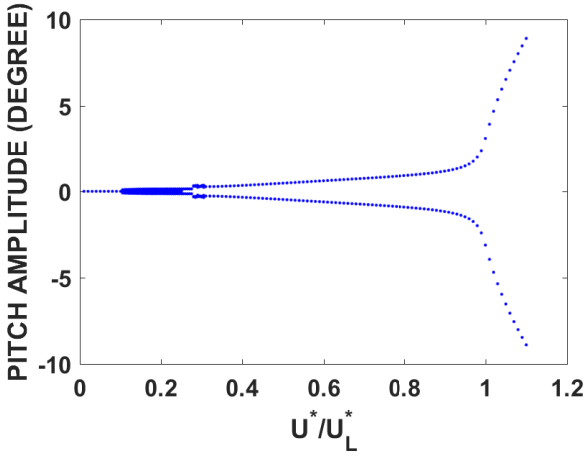

(b)

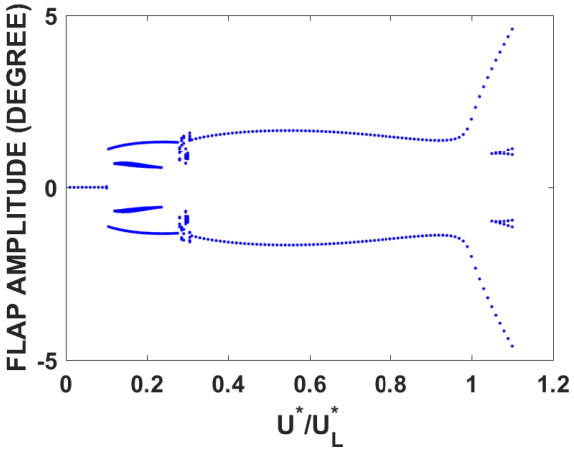

(c)

Figure 3.4: Bifurcation diagrams for (a) plunge, (b) pitch, and (c) flap DOFs, for a system with flap free-play and cubic pitching and linear plunging stiffnesses (airfoil 5).

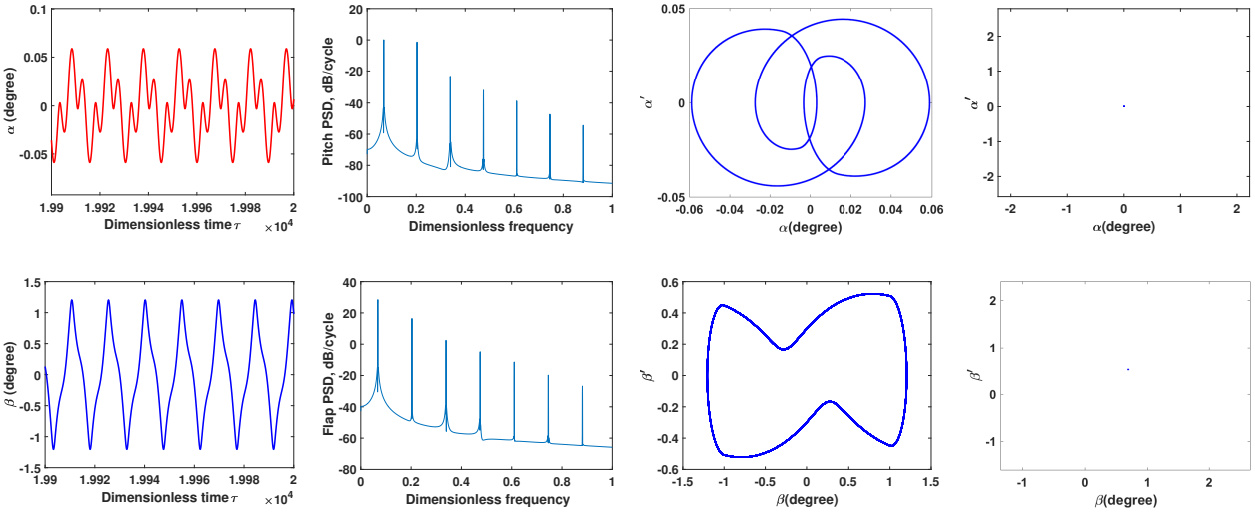

Figure 3.5: The dynamics of the system with the free-play nonlinearity in flap (airfoil 4) at $U^*/U_L^* = 0.17$: Top from *left* to *right*, time history, PSD, phase-plane, and Poincaré plots, respectively, for the pitch DOF, α, and bottom from *left* to *right*, time history, PSD, phase-plane, and Poincaré plots, respectively, for the flap DOF, β.

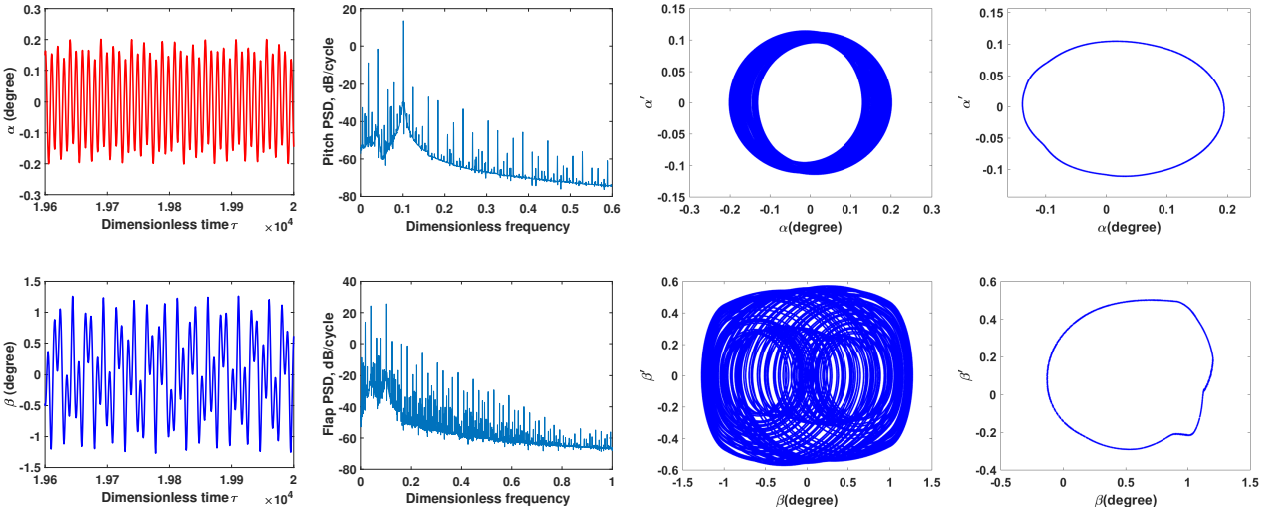

Figure 3.6: The dynamics of the system with the free-play nonlinearity in flap (airfoil 4) at $U^*/U_L^* = 0.30$: Top from *left* to *right*, time history, PSD, phase-plane, and Poincaré plots, respectively, for the pitch DOF, α, and bottom from *left* to *right*, time history, PSD, phase-plane, and Poincaré plots, respectively, for the flap DOF, β.

it is capable of avoiding the system from divergence beyond the flutter speed. However, long-time oscillation may lead to fatigue even structural failure. Therefore, the suppression of LCO will be the main objective of the next chapter.

Chapter 4

Active Control without Parametric Uncertainty

Starting from this chapter, the design of a control system for the nonlinear aeroelastic system introduced in Chapter 3 will be discussed. Here, the active controller based on feedback linearized system is designed. The effectiveness of the controller is assessed through some numerical results.

4.1 Feedback Linearization

To suppress flutter and to alleviate undesirable phenomena, such as atmospheric disturbances that may occur to an aircraft, a control system may be coupled to the original aeroelastic system. There are mainly two kinds of control techniques for the suppression of flutter. One technique is to passively control structural deformation by altering the structure to improve its aeroelastic performance, like improving the directional stiffness, or aeroelastic tailoring [55]. But the cost of this technique is very high as the aircraft structure should be redesigned and the control effect can not be guaranteed when the aircraft encounters disturbances during

the operation of flight. Thus in this thesis, active control system design is studied. The active control of aeroelastic systems, sometimes known as aero-servo-elasticity, has as its objective the modification of the aeroelastic behavior of the system by the introduction of deliberate control forces [56]. In aero-servo-elastic model, aerodynamic, inertia and dynamic loads, as well as control commands are balanced. Extensive research has been conducted in the past to achieve active flutter suppression and gust alleviation, where one or more control surfaces are actuated according to a control law which generates the control command based on the measurements taken, by sensors, on the aircraft.

Adding the control command β_c to the 3-DOF system in Chapter 3, the state-space equation (3.18) with the control input may be modified as:

$$\mathbf{X}' = F(\mathbf{X}, \tau) + \mathbf{G}\beta_c, \tag{4.1}$$

where $\mathbf{G} = (0, g_2, 0, g_4, 0, g_6, 0, 0, 0, 0, 0, 0, 0, 0)^T$; g_2, g_4 and g_6 are control input coefficients which are non-zero.

Define the following output variable: $y = H(x) = x_1$, meaning that the primary control objective is to stabilize the pitch output α. The relative degree of the above output is calculated as follows:

$$\begin{aligned} &y = H(x) = x_1, \quad y' = L_F H + L_G H = x_2, \\ &y'' = L_F^2 H + L_G L_F H = F_2 + g_2 \beta_c, \end{aligned} \tag{4.2}$$

where F_2 is the second row of $F(\mathbf{X})$, and $L_f y(x)$ is a Lie derivative of y in the direction of

f defined as [57]

$$L_f y(x) = \sum_{i=1} \frac{\partial y}{\partial x_i} \cdot f_i, \quad L_f L_g y(x) = L_g[L_f y(x)]. \tag{4.3}$$

Due to the fact that $g_2 \neq 0$, we can say that the relative degree of the system is $r = 2$, meaning that 2 DOFs of the system can be linearized. To accomplish the partial feedback linearization, the state transformation $X \rightarrow \Phi$ is considered, as follows:

$$\begin{aligned}
&\mathbf{X} \rightarrow \Phi \\
&\phi_1 = y = x_1 \\
&\phi_2 = y' = x_2 \\
&\phi_3 = x_3 \\
&\phi_4 = g_2 x_4 - g_4 x_2 \\
&\phi_5 = x_5 \\
&\phi_6 = g_6 x_4 - g_4 x_6 \\
&\phi_i = x_i, \ i = 7, 8, 9...14.
\end{aligned} \tag{4.4}$$

Note that the transformation for ϕ_3, ϕ_4, ϕ_5, ϕ_6 should satisfy $L_g \phi_i = 0, \ i = 3, 4, 5, 6$. Thus, the new state-space equations are obtained as below,

$$\Phi' = F(\Phi) + \begin{Bmatrix} 0 & g_2 & 0 & \dots 0 \end{Bmatrix}^{\mathrm{T}} \beta_c, \tag{4.5}$$

where $F_i(\Phi), \ i = 2, 4, 6$ are converted by $F_i(\mathbf{X})$. Now, the partial feedback linearization can

be achieved by setting the control input β_c as

$$\beta_c = (-F_2(\Phi) + \upsilon)/g_2, \tag{4.6}$$

where υ is a new yet to be defined control input. The second row in equation (4.5) will then be

$$\phi_2' = \upsilon. \tag{4.7}$$

By choosing a suitable υ based on any linear control design technique, we can make the linear subsystem $\{\phi_1, \phi_2\}'$ stable. Then, the question is whether the internal dynamics will also behave well, i.e. whether the internal states will remain bounded, which may not be easy to investigate. However, the output y is maintained at identically zero, i.e. all its time derivatives are zero. So the zero-dynamics of the nonlinear system can be analyzed.

4.2 Active Controller Design and Numerical Results

Airfoil 5 in Section 3.2 is considered for the aero-servo-elastic analyses. In order to test the closed-loop control system, the system is excited by a 1-cosine gust input with $w_0^* = 0.29$ (i.e. $w_0 = 10$ m/s) at $U^* = U_L^*$. The same initial conditions as those in Section 3.2 are also used here. A PD controller is utilized to design the closed-loop control system for the linearized system as below:

$$\upsilon = G_d(0 - \alpha) + G_v(0 - \alpha'), \tag{4.8}$$

where G_d and G_v are the control gains about the generalized displacement error and velocity error, respectively. Combining equations 4.7 and 4.8 along with the assuming $\alpha = \alpha_0 e^{\lambda t}$, the

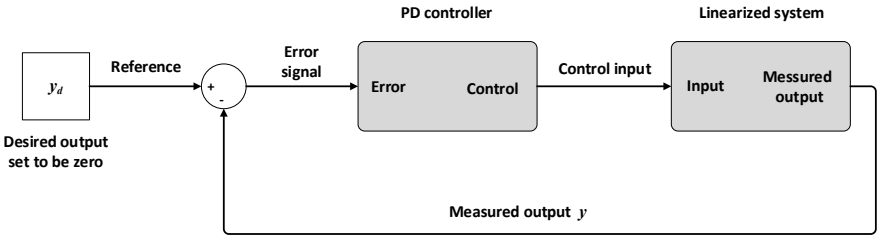

Figure 4.1: Control block diagram without uncertainties.

eigenvalue equation can be obtained as

$$\lambda^2 + G_v\lambda + G_d = 0, \tag{4.9}$$

where $\lambda_i = Re(\lambda_i) + jIm(\lambda_i), (i = 1, 2)$ being the complex eigenvalues of the linear subsystem.

Fig. 4.1 shows the control block diagram with the PD controller and the feedback linearization controller. By analysing the eigenvalues of the linear subsystem $\{\phi_1, \phi_2\}'$, multiple sets of gains are tested. All the gains tested lead the poles of subsystem located at the negative semi-plane of the complex coordinate. Through the zero dynamics analysis, the nonlinear systems are all stable at trans-flutter speed. But it should be emphasized that the zero dynamics stability only guarantees the local stability of the internal dynamics; for details, refer to [57].

Three sets of time responses for the three DOFs are shown in Figs. 4.2 to 4.4. As the convergence of all DOFs should be considered for the stability problem, the responses for three DOFs are all presented in Chapters 4 and 5. It is found that if the imaginary parts of the eigenvalues are non-zero, the pitching response overshoots, which also results in greater amplitude in the other DOFs as shown in Fig. 4.2. When $G_d = G_v = 0.01$, the eigenvalues are calculated as $\lambda_1 = -0.005 + j0.2,\ \lambda_2 = -0.005 - j0.2$. Although the convergence of three DOFs is achieved, but the transient time is quite long and overshoots of pitching response are observed. Also the control surface deflection of closed-loop is greater than that of open-loop

with gust.

Therefore, the imaginary parts of the eigenvalues are removed. For the first set, we have taken $\lambda_1 = -1,\ \lambda_2 = -0.5$, then the gains are obtained as $G_d = 0.5,\ G_v = 1.5$ in the control law. While for the second set, $\lambda_1 = -0.2,\ \lambda_2 = -0.005$ ($G_d = 0.001,\ G_v = 0.205$) have been considered. As seen from the figures, the control system via either set of gains could effectively suppress LCOs and stabilize the system at the linear flutter speed. It is noted that since a pitch primary control has been implemented here, the closed-loop pitching response decays rapidly with time (compared with the other two DOFs), and its peak value may be much smaller than that for the open-loop system under the gust load. From Fig. 4.3, it is evident that large absolute values of real parts would result in short convergence time while also demanding large flap deflections. As seen from Fig. 4.4, the system behaves reasonably well: closed-loop pitching and plunging amplitudes do not exceed those for the open-loop system under the gust load, and the control surface just overshoots a little bit to execute control of the system.

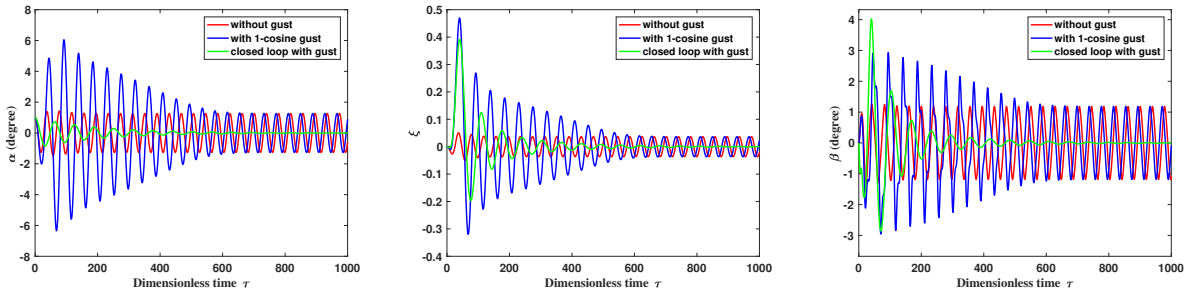

Figure 4.2: Open- and closed-loop pitch(*left*), plunge(*centre*), and flap(*right*) responses to a 1-cosine gust with $w_0^* = 0.29$ ($w_0 = 10$ m/s) at $U^* = U_L^*$ with $\alpha_0 = 1^\circ$, and $G_d = G_v = 0.01$.

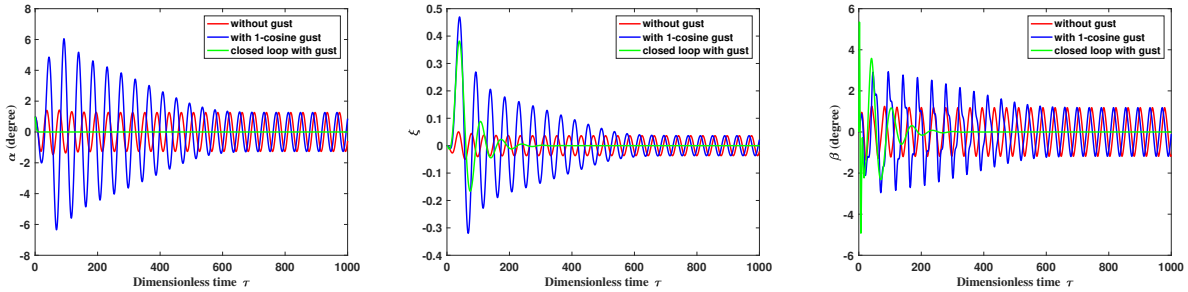

Figure 4.3: Open- and closed-loop pitch(*left*), plunge(*centre*), and flap(*right*) responses to a 1-cosine gust with $w_0^* = 0.29$ ($w_0 = 10$ m/s) at $U^* = U_L^*$ with $\alpha_0 = 1^\circ$, and $G_d = 0.5$, $G_v = 1.5$.

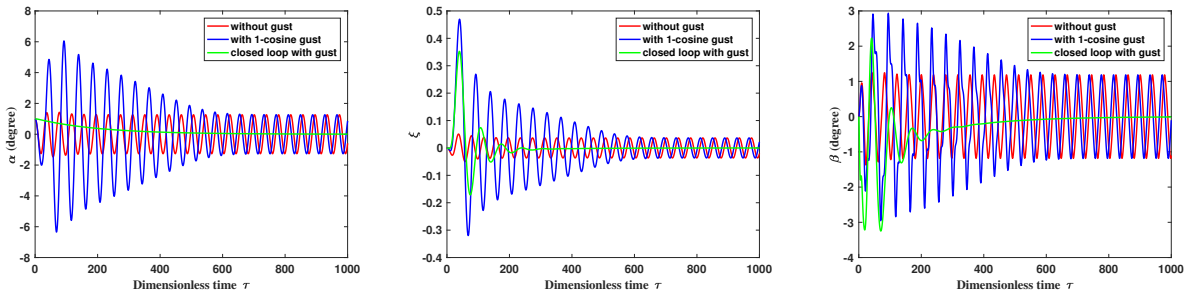

Figure 4.4: Open- and closed-loop pitch(*left*), plunge(*centre*), and flap(*right*) responses to a 1-cosine gust with $w_0^* = 0.29$ ($w_0 = 10$ m/s) at $U^* = U_L^*$ with $\alpha_0 = 1^\circ$, and $G_d = 0.001$, $G_v = 0.205$.

4.3 Summary

In this chapter, the partial feedback linearization was used in order to allow for the application of a viable control system to suppress flutter and to stabilize the system. A PD controller was designed with some reasonable choice of control parameters, and it was shown to be quite effective. Note that this only guarantees a local asymptotic stabilization due to the zero-dynamics and the controller is designed without considering the uncertainties of the system. In the next chapter, an adaptive controller is designed considering some structural uncertainties.

Chapter 5

Adaptive Control with Parametric Uncertainties

Considering structural uncertainties including uncertain structural stiffness and damping coefficients, an adaptive controller is designed based on the similar design thought with that in Chapter 4.

In this chapter, a Lyapunov function is employed to prove the stability of the system, and the robustness of the controller is demonstrated through some numerical results considering both stiffness and damping uncertainties.

5.1 Adaptive Controller Design

In Chapter 4, the nonlinearity in pitching was considered as a cubic form and the parameters of nonlinearity were assumed to be known. While in real situations, it is quite difficult to estimate the stiffness nonlinearity. Adaptive control is a approach to the control of the system with uncertainties. The basic idea in adaptive control is to estimate the uncertain plant parameters (or, equivalently, the corresponding controller parameters) on-line based

on the measured system signals, and use the estimated parameters in the control input computation. An adaptive control system can thus be regarded as a control system with on-line parameter estimation [57]. According to [58], the continuous nonlinear stiffness of the pitching DOF can be identified using a polynomial fit of the measured response. Thus, in this chapter, the uncertain stiffness in pitching is estimated. The torsional spring stiffness for the pitch DOF is modelled as a polynomial:

$$N_\alpha = \theta_1\alpha + \theta_2\alpha^2 + \theta_3\alpha^3 + \cdots + \theta_N\alpha^N = \sum_{i=1}^{N} \theta_i\alpha^i. \tag{5.1}$$

The structural damping is also considered as uncertainties. equation (3.13) can be rewritten as

$$\begin{aligned}
&A_1\alpha'' + A_2\beta'' + A_3\xi'' + A_4\alpha' + A_5\beta' + A_6\xi' + A_7\alpha + A_8\beta + A_9\xi + A_{10}N_\alpha + A_{11}w_1 \\
&\quad + A_{12}w_2 + A_{13}w_3 + A_{14}w_4 + A_{15}w_5 + A_{16}w_6 + A_{17}w_7 + A_{18}w_8 + A_{19}\alpha' = f(\tau), \quad (5.2)\\
&B_1\alpha'' + B_2\beta'' + B_3\xi'' + B_4\alpha' + B_5\beta' + B_6\xi' + B_7\alpha + B_8\beta + B_9\xi + B_{10}N_\beta + B_{11}w_1 \\
&\quad + B_{12}w_2 + B_{13}w_3 + B_{14}w_4 + B_{15}w_5 + B_{16}w_6 + B_{17}w_7 + B_{18}w_8 + B_{19}\beta' = g(\tau), \quad (5.3)\\
&C_1\alpha'' + C_2\beta'' + C_3\xi'' + C_4\alpha' + C_5\beta' + C_6\xi' + C_7\alpha + C_8\beta + C_9\xi + C_{10}N_\xi + C_{11}w_1 \\
&\quad + C_{12}w_2 + C_{13}w_3 + C_{14}w_4 + C_{15}w_5 + C_{16}w_6 + C_{17}w_7 + C_{18}w_8 + C_{19}\xi' = h(\tau), \quad (5.4)
\end{aligned}$$

where A_{19}, B_{19} and C_{19} are some coefficients including uncertain damping ratios.

In Chapter 4, we show that the nonlinear aeroelastic system can be stabilized (at least

locally) using the partial feedback linearization based on the pitching DOF. Including uncertainty terms, equation (4.2) is rewritten as follows:

$$y = H(x) = x_1, \quad y' = L_F H + L_G H = x_2,$$
$$y'' = L_F^2 H + L_G L_F H = F_2 + \sum_{i=1}^{n} \theta_i R_i + \sum_{j=1}^{3} \delta_j Q_j + g_2 \beta_c, \tag{5.5}$$

where

$$F_2 = \sum_{i=1}^{14} h_i x_i, \ R_i = p_1 (\frac{r_\alpha}{U^*})^2 \alpha^i, \ \delta_1 = \zeta_\alpha, \ \delta_2 = \zeta_\beta, \ \delta_3 = \zeta_\xi,$$
$$Q_1 = \frac{2p_1 (r_\alpha)^2 \alpha'}{U^*}, \ Q_2 = \frac{2p_2 \bar{\omega}_2 (r_\beta)^2 \beta'}{U^*}, \ Q_3 = \frac{2p_3 \bar{\omega}_1 \xi'}{U^*}, \tag{5.6}$$

where h_i $(i = 1, \ldots, 14)$ are the coefficients of states; p_j $(j = 1, 2, 3)$ are the system parameters derived from [37, equation (2)].

To achieve the partial feedback linearization, the control command β_c is obtained as

$$\beta_c = \frac{1}{g_2}(-F_2(\Phi) - \sum_{i=1}^{N} \theta_i R_i - \sum_{j=1}^{3} \delta_j Q_j + \upsilon), \tag{5.7}$$

where υ is the modified control input for the adaptive controller.

Provided that θ_i and δ_i are uncertain, and if their estimations are available, denoted by $\hat{\theta}_i$ and $\hat{\delta}_j$, respectively, then equation (5.7) may be rewritten using the 'certainty equivalent' control law as below

$$\beta_c = \frac{1}{g_2}(-F_2(\Phi) - \sum_{i=1}^{N} \hat{\theta}_i R_i - \sum_{j=1}^{3} \hat{\delta}_j Q_j + \upsilon), \tag{5.8}$$

and thus, the linearized sub-system will be:

$$\begin{aligned}
\phi_1' &= \phi_2, \\
\phi_2' &= \sum_{i=1}^{N}(\theta_i - \hat{\theta}_i)R_i + \sum_{j=1}^{3}(\delta_j - \hat{\delta}_j)Q_j + \upsilon \\
&\equiv (\Theta - \hat{\Theta})^T\mathbf{R} + (\Delta - \hat{\Delta})^T\mathbf{Q} + \upsilon,
\end{aligned} \tag{5.9}$$

in which

$$\begin{aligned}
&\Theta = \{\theta_i\}, \hat{\Theta} = \{\hat{\theta}_i\}, \mathbf{R} = \{R_i(\phi)\}, \\
&\Delta = \{\delta_j\}, \hat{\Delta} = \{\hat{\delta}_j\}, \mathbf{Q} = \{Q_j(\phi)\}.
\end{aligned} \tag{5.10}$$

A modified control input $\upsilon = -\bar{G}_d\phi_1 - \bar{G}_v\phi_2$ ($\bar{G}_d,\ \bar{G}_v > 0$) is utilized to make the linear sub-system $\{\phi_1, \phi_2\}$ stable. By substituting the control input υ, equation (5.9) may be rewritten as

$$\begin{Bmatrix} \phi_1' \\ \phi_2' \end{Bmatrix} = \begin{bmatrix} 0 & 1 \\ -\bar{G}_d & -\bar{G}_v \end{bmatrix} \begin{Bmatrix} \phi_1 \\ \phi_2 \end{Bmatrix} + \begin{Bmatrix} 0 \\ \tilde{\Theta}^T\mathbf{R} \end{Bmatrix} + \begin{Bmatrix} 0 \\ \tilde{\Delta}^T\mathbf{Q} \end{Bmatrix}, \tag{5.11}$$

where $\tilde{\Theta} = \Theta - \hat{\Theta}$, $\tilde{\Delta} = \Delta - \hat{\Delta}$ are the estimation errors.

5.2 Estimation Update Law Design

The stability and convergence of the adaptive control system can be analyzed using the Lyapunov theory. The basic philosophy of Lyapunov's direct method is the mathematical extension of a fundamental physical observation: if the total energy of a mechanical (or electrical) system is continuously dissipated, the system, whether linear or nonlinear, must

eventually settle down to an equilibrium point. Thus, the stability of a system can be determined by examining the variation of a single scalar function, which is called the Lyapunov function [57]. For the closed-loop dynamics equation (5.11), with $\{\phi_1, \phi_2\}^T$, Θ and Δ as states, the following Lyapunov function candidate is chosen

$$V = \frac{1}{2} \left\{ \begin{array}{c} \phi_1 \\ \phi_2 \end{array} \right\}^T \left\{ \begin{array}{c} \phi_1 \\ \phi_2 \end{array} \right\} + \frac{1}{2} \tilde{\Theta}^T \tilde{\Theta} + \frac{1}{2} \tilde{\Delta}^T \tilde{\Delta}. \tag{5.12}$$

The time derivative of equation (5.12) is obtained as

$$V' = \left\{ \begin{array}{c} \phi_1 \\ \phi_2 \end{array} \right\}^T \left[\begin{array}{cc} 0 & 1 \\ -\bar{G}_d & -\bar{G}_v \end{array} \right] \left\{ \begin{array}{c} \phi_1 \\ \phi_2 \end{array} \right\} + \phi_2 \tilde{\Theta}^T \mathbf{R} + \tilde{\Theta}^T \tilde{\Theta}' + \phi_2 \tilde{\Delta}^T \mathbf{Q} + \tilde{\Delta}^T \tilde{\Delta}'. \tag{5.13}$$

If the estimation parameter update laws are chosen to be as

$$\tilde{\Theta}' = (-\hat{\Theta}') = -\phi_2 \mathbf{R}, \tilde{\Delta}' = (-\hat{\Delta}') = -\phi_2 \mathbf{Q}, \tag{5.14}$$

then $V' \leq 0$, and thus, the stability of the sub-system equation (5.11) is guaranteed. Fig. 5.1 shows the control block diagram with structural uncertainties. Compared with Fig. 4.1, there is an extra module which is employed to update the estimation parameters. It should be emphasized that the above adaptive law does not guarantee the convergence of the estimation parameters, which are largely dependent on the richness of the excitation signal [59].

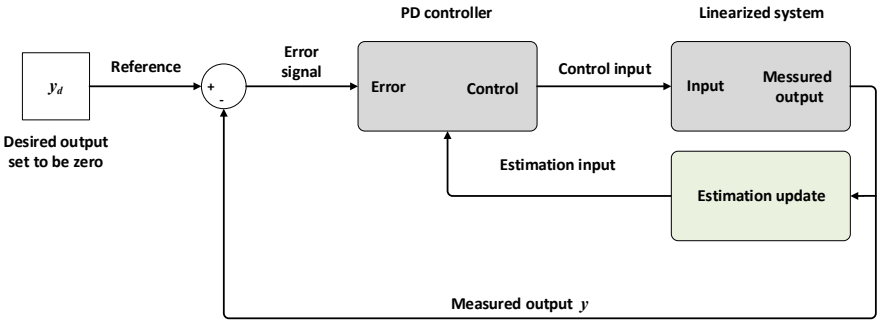

Figure 5.1: Control block diagram with structural uncertainties.

5.3 Closed-loop Numerical Results

It is assumed that the 2-D rigid wing is supported by a nonlinear rotational and a linear translational spring and has a linear spring about the flap hinge (refer to Fig. 3.1). The rest of system parameters (including the nominal values of δ_i) are taken from [14, Table 1]. The initial conditions are: $\xi_0 = 0$, $\alpha_0 = 1°$, $\beta_0 = 0$, with their time derivatives equal to zero. Same as Section 4.2, the system is excited by a 1-cosine gust input with $w_0^* = 0.29$ (i.e. $w_0 = 10$ m/s) at $U^* = U_L^*$. Here, the control parameters are set as $\bar{G}_d = 0.001$, $\bar{G}_v = 0.205$, which behave well in Chapter 4, in the control law (eigenvalues of subsystem $\lambda_1 = -0.2, \lambda_2 = -0.005$) for the PD controller after the application of partial feedback linearization. The true values of $\{\Theta\}$ used in the simulation are taken as $\{\Theta\}^T = \{1 \;\; 1.459 \;\; 97.715 \;\; 3.889 \;\; -744.612\}$ [60].

The adaptive controllers are developed for three different scenarios of system parameters uncertainty: (i) stiffness coefficients are uncertain, (ii) damping coefficients are uncertain, and (iii) both stiffness and damping coefficients are uncertain. The results are shown, respectively, in Figs. 5.2 to 5.4. These figures confirm that the adaptive control system could effectively suppress LCOs and stabilize the system at the linear flutter speed for all three scenarios. It is noted that since a pitch primary control has been implemented here, the closed-loop pitching response decays rapidly with time (compared with the other two

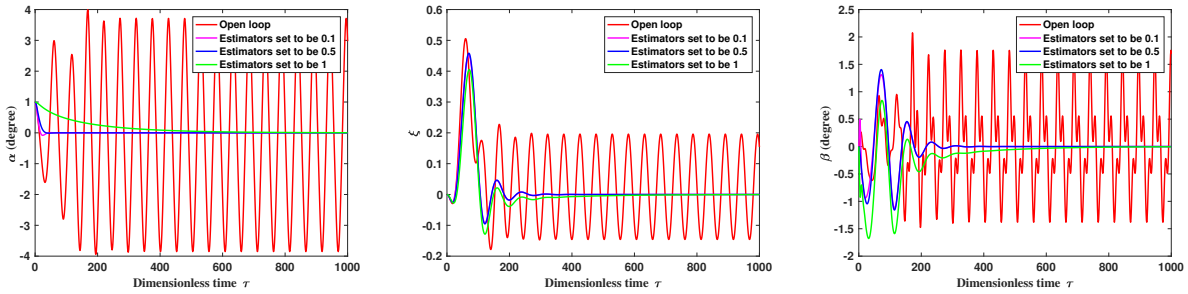

Figure 5.2: Pitch (*left*), plunge (*centre*), and flap (*right*) responses of open- and closed-loop with different initial estimations of stiffness parameters to a 1-cosine gust with $w_0^* = 0.29$ ($w_0 = 10$ m/s) at $U^* = U_L^*$ with $\alpha_0 = 1^\circ$ and $\beta_0 = \xi_0 = \alpha_0' = \beta_0' = \xi_0' = 0$.

DOFs), and its peak value may be much smaller than that for the open-loop system under the gust load.

Fig. 5.2 shows the open-loop results (i.e. time responses) along with closed-loop results for the first scenario of system parameters uncertainty. Three sets of initial estimation of parameters are examined, where as seen from the figure, with either set, the control system is capable of suppressing the LCO at the linear flutter speed. Since here the pitching DOF is taken as the primary control output, the controller performs very well in damping pitching motion, where virtually no overshoot is observed. Surprisingly, when using an initial estimation with smaller deviation from the true values (used for open-loop solutions), the convergence time for all DOFs increases. This, however, may not be always true, as can be verified, for example, from Fig. 5.3 which shows the results for the second uncertainty scenario – damping uncertainty. As seen from the figure, with the initial estimation parameters $\hat{\Delta}^T = \{0.05\ 0.05\ 0.05\}$, which is closer to the true values, the controller shows superiority in stabilizing LCOs.

Fig. 5.4 shows the results for the third scenario where both stiffness and damping parameters are considered as uncertain. Here, $\hat{\Theta}^T = \{0.1\ 0.1\ 0.1\ 0.1\ 0.1\}$ and $\hat{\Delta}^T = \{0.25\ 0.25\ 0.25\}$ are taken as the initial estimation parameters. As seen from the figure, LCO suppression is achieved after the airfoil undergoes a few cycles of oscillation. The dimensionless time required for the response to reach the desired value (zero, here) is about 400 (≈ 1.46 sec).

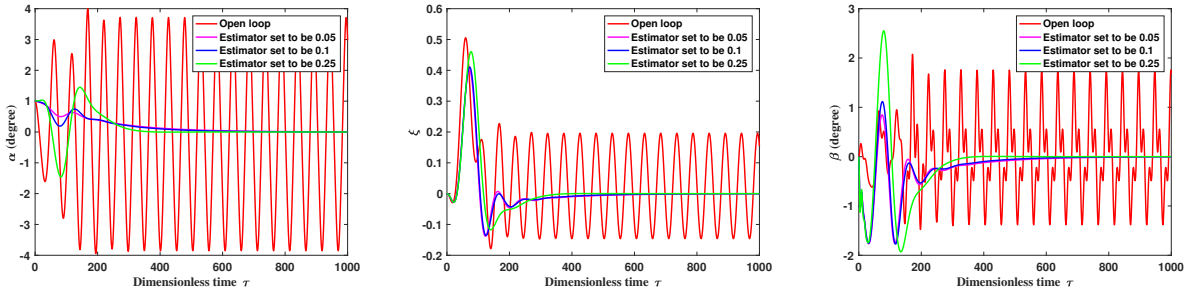

Figure 5.3: Pitch (*left*), plunge (*centre*), and flap (*right*) responses of open- and closed-loop with different initial estimations of damping parameters to a 1-cosine gust with $w_0^* = 0.29$ ($w_0 = 10$ m/s) at $U^* = U_L^*$ with $\alpha_0 = 1^\circ$ and $\beta_0 = \xi_0 = \alpha_0' = \beta_0' = \xi_0' = 0$.

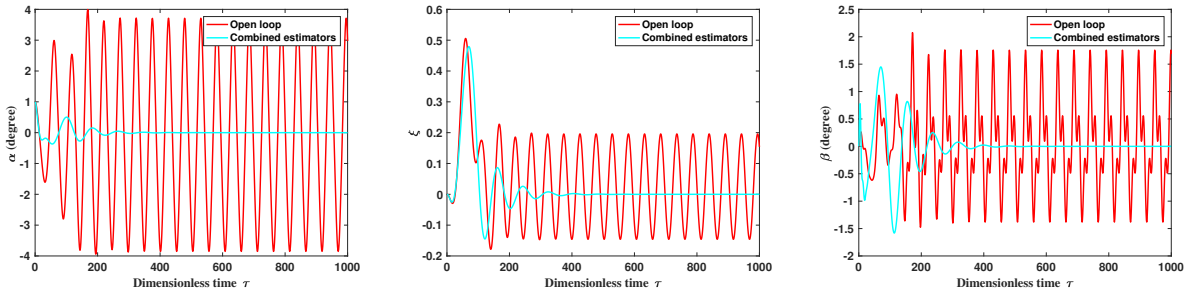

Figure 5.4: Pitch (*left*), plunge (*centre*), and flap (*right*) responses of open- and closed-loop with combined initial estimations of both stiffness and damping parameters to a 1-cosine gust with $w_0^* = 0.29$ ($w_0 = 10$ m/s) at $U^* = U_L^*$ with $\alpha_0 = 1^\circ$ and $\beta_0 = \xi_0 = \alpha_0' = \beta_0' = \xi_0' = 0$.

Considering the fact that the dimensionless loading time of the 1-cosine gust is 100, the adaptive control system designed in this chapter is quite effective.

5.4 Summary

In this chapter, after introducing structural uncertainties, an adaptive control system was designed for the 2-D wing. The parameter update law was proposed to estimate the unknown parameters and a Lyapunov function was constructed and utilized to prove the stability of the subsystem. Numerical results show that the adaptive control system is effective in suppressing limited-cycle oscillations for different scenarios of structural stiffness and damping uncertainties. The controller was demonstrated to be quite robust when considering

different initial estimation parameters for the simulations. Even with both uncertainties, the adaptive controller was capable of stabilizing the system from LCO effectively.

Chapter 6

Conclusions and Future Works

In this chapter, the key findings of the present thesis are summarized, and then, some possible extensions and future works are mentioned.

6.1 Conclusions

In this thesis, the typical dynamics of a structurally-nonlinear airfoil in incompressible flow and the coupling effects of a gust input with structural nonlinearities were presented. The suppression of LCO was investigated considering some structural uncertainties.

For the 2-DOF model, two types of nonlinearities including free-play and hysteresis in the pitch DOF were studied. In addition, the response of these systems to sharp-edged and 1-cosine gust profiles were examined. The numerical results presented in this thesis showed that structural nonlinearities may have significant effects on the dynamical behavior of the system. In particular, for the airfoil with the free-play nonlinearity, it was found that the stability may be lost through a Hopf bifurcation at a critical flow velocity significantly lower than that for the linear system. The post-critical dynamics of the system was found to be very complex, where motion may become chaotic through period-doubling bifurcations. Classical period-1 and period-2 motions were observed in plunge DOF, while period-1 and

period-2 with harmonics motions were observed in pitch DOF, which was more complicated. When there was no gust input, a complex but point-symmetric basin of attraction was found. However, when the airfoil was excited by the gust, the basin of attraction became relatively deterministic, where the region of stability became more confined to one side of the plot ($\alpha_0 > 0$ when the gust was in the positive direction and vice versa). The probability of the occurrence of LCO was also found to increase as the gust became stronger.

For the airfoil with the hysteresis nonlinearity, the dynamics was found to be relatively simple. The airfoil remained stable for a wide range of flow velocities but lost the stability via a Hopf bifurcation at a critical flow velocity comparable to the linear flutter speed. No secondary bifurcations were observed, and the amplitude of the LCO emanating from the Hopf bifurcation increased sharply with the flow velocity. It was found from the basin of attraction plots that there were two finite bands between regions of LCO, in which the stability was guaranteed independently from the value of the initial pitch angle.

From the results presented in the modelling part, it is concluded that studying the effects of time-dependent excitation due to atmospheric turbulence on the dynamics of nonlinear lifting surfaces and devising methods to mitigate those effects are essential for the design and operation of aircraft. These studies are particularly crucial for the design of new generation of aircraft, manned or unmanned, which are likely to be lighter, faster, more flexible, and more agile. A good example is in the application of Urban Air Mobility (UAM). In the complex urban environment, the flying vehicles may encounter gusts or turbulences from different directions. Besides, the effects of these disturbances are likely to be significant as the airflow velocity around the vehicles change obviously compared to the situation where vehicles fly at a high speed in the stratosphere. For both safety of the flight and comfort level of passengers, the coupling effects of structural nonlinearities and gusts demonstrated in this thesis should be considered.

For an airfoil with a control surface, free-play about the flap hinge may cause the system to become unstable at a flow velocity well below the flutter speed of the linear system, U_L^*. The flat spot nonlinearity about the flap hinge, in addition to LCOs, may also lead to complex motion of airfoil, such as quasi-periodic and chaotic-like. Moreover, it was found that the partial feedback linearization may be used in order to allow for application of a viable control system to suppress flutter and to decrease the amplitude of LCO. This, however, guaranteed only a local asymptotic stabilization due to the zero-dynamics. After introducing structural uncertainties, an adaptive control system was designed for the wing. The estimate law was updated and a Lyapunov function was constructed and utilized to prove the stability of the subsystem. Numerical results showed that the adaptive control system was effective in suppressing LCOs for different scenarios of structural stiffness and damping uncertainties. The robustness of controller was examined when considering different initial estimation parameters. Considering both uncertainties, the controller was capable of suppressing LCO with initial estimation of great deviation. Also, it was found that the convergence of the estimation parameters was not necessary for the stability of the system.

From the results presented in the control part, it is concluded that the effective active controller may expand the flight envelope and suppress the oscillation quickly. On the premise that some structural parameters are uncertain, the control of oscillation is still achieved effectively, which makes the control system designed in this thesis feasible in the reality. Due to the suppression of oscillation, the control system may prevent the airfoil from fatigue, which is pretty common in the aircraft structure.

6.2 Future Works

- In this study, the indicial aerodynamic model based on Wagner's function and gust model based on Küssner function are employed to make up for the whole aeroelastic

system in time domain. Two deterministic gust models are explored in this study; however, in reality atmospheric turbulence may be highly stochastic. If, instead, high-fidelity CFD models are utilized to generate aerodynamic forces and moments, including those due to the stochastic gust excitation, the numerical results on the interactions between the structure and air flow are expected to be more accurate. This is left as a future extension of the present work.

- The local stability of the nonlinear system has been achieved based on the assumption of zero-dynamics. For the next step, the achievement of global stability will be pursued. Furthermore, an effective adaptive controller of a system with uncertain structural stiffness and damping coefficients has been designed. How to achieve the adaptive control of a system with more uncertainties, even the whole system being a 'black box', will also be a future task.

Bibliography

[1] F. Afonso, J. Vale, É. Oliveira, F. Lau, and A. Suleman, "A review on non-linear aeroelasticity of high aspect-ratio wings," *Progress in Aerospace Sciences*, vol. 89, pp. 40–57, 2017.

[2] B. H. K. Lee, S. J. Price, and Y. S. Wong, "Nonlinear aeroelastic analysis of airfoils: bifurcation and chaos," *Progress in Aerospace Sciences*, vol. 35, no. 3, pp. 205–334, 1999.

[3] T. Theodorsen, "General theory of aerodynamic instability and the mechanism of flutter." *NACA*, no. 496, 1935.

[4] P. Beran, B. Stanford, and C. Schrock, "Uncertainty quantification in aeroelasticity," *Annual Review of Fluid Mechanics*, vol. 49, pp. 361–386, 2017.

[5] D. S. Woolston, H. L. Runyan, and R. E. Andrews, "An investigation of effects of certain types of structural nonlinearities on wing and control surface flutter," *Journal of the Aeronautical Sciences*, vol. 24, no. 1, pp. 57–63, 1957.

[6] B. Lee and J. Desrochers, "Flutter analysis of a two-dimensional airfoil containing structural nonlinearities." National Aeronautical Establishment Ottawa (Ontario), Tech. Rep., 1987.

[7] E. H. Dowell and D. Tang, "Nonlinear aeroelasticity and unsteady aerodynamics," *AIAA Journal*, vol. 40, no. 9, pp. 1697–1707, 2002.

[8] J. R. Wright and J. E. Cooper, *Introduction to Aircraft Aeroelasticity and Loads*. John Wiley & Sons, 2008, vol. 20.

[9] S. J. Price, B. H. K. Lee, and H. Alighanbari, "Post instability behavior of a two-dimensional airfoil with a structural nonlinearity," *Journal of Aircraft*, vol. 31, no. 6, pp. 1395–1401, 1994.

[10] S. J. Price, H. Alighanbari, and B. H. K. Lee, "The aeroelastic response of a two-dimensional airfoil with bilinear and cubic structural nonlinearities," *Journal of Fluids and Structures*, vol. 9, no. 2, pp. 175–193, 1995.

[11] H. Alighanbari and S. Price, "The post-Hopf-bifurcation response of an airfoil in incompressible two-dimensional flow," *Nonlinear Dynamics*, vol. 10, no. 4, pp. 381–400, 1996.

[12] L. Liu, Y. Wong, and B. Lee, "Non-linear aeroelastic analysis using the point transformation method, part 1: Freeplay model," *Journal of Sound and Vibration*, vol. 253, no. 2, pp. 447–469, 2002.

[13] L. Liu, Y. Wong, and B. Lee, "Non-linear aeroelastic analysis using the point transformation method, Part 2: hysteresis model," *Journal of Sound and Vibration*, vol. 253, no. 2, pp. 471–483, 2002.

[14] L. Liu and E. H. Dowell, "Harmonic balance approach for an airfoil with a freeplay control surface," *AIAA Journal*, vol. 43, no. 4, pp. 802–815, 2005.

[15] F. Chen, Y. Chen, and J. Liu, "Equivalent linearization method for the flutter system of an airfoil with multiple nonlinearities," *Communications in Nonlinear Science and Numerical Simulation*, vol. 17, no. 12, pp. 4529–4535, 2012.

[16] C. Cui, J. Liu, and Y. Chen, "Simulating nonlinear aeroelastic responses of an airfoil with freeplay based on precise integration method," *Communications in Nonlinear Science and Numerical Simulation*, vol. 22, no. 1-3, pp. 933–942, 2015.

[17] C. Cui, S. Xie, X. Huang, J. Liu, and Y. Chen, "A highly accurate approach for aeroelastic system with hysteresis nonlinearity," *International Journal of Aerospace Engineering*, vol. 2017, 2017.

[18] W.-X. Zhong, "On precise integration method," *Journal of Computational and Applied Mathematics*, vol. 163, no. 1, pp. 59–78, 2004.

[19] H. Yamasaki and B. I. Epureanu, "Forecasting supercritical and subcritical hopf bifurcations in aeroelastic systems," *International Journal of Non-Linear Mechanics*, vol. 94, pp. 400–405, 2017.

[20] A. Ghadami and B. I. Epureanu, "Forecasting critical points and post-critical limit cycles in nonlinear oscillatory systems using pre-critical transient responses," *International Journal of Non-Linear Mechanics*, vol. 101, pp. 146–156, 2018.

[21] L. Zhang and F. Chen, "Bifurcation behavior and chaotic dynamics of a three-degree-of-freedom aeroelastic system," *International Journal of Non-Linear Mechanics*, vol. 109, pp. 63–79, 2019.

[22] W. Tian, Z. Yang, and T. Zhao, "Nonlinear aeroelastic characteristics of an all-movable fin with freeplay and aerodynamic nonlinearities in hypersonic flow," *International Journal of Non-Linear Mechanics*, 2019.

[23] D. Tang and E. H. Dowell, "Aeroelastic airfoil with free play at angle of attack with gust excitation," *AIAA Journal*, vol. 48, no. 2, pp. 427–442, 2010.

[24] D. A. Peters, S. Karunamoorthy, and W.-M. Cao, "Finite state induced flow models. I-Two-dimensional thin airfoil," *Journal of Aircraft*, vol. 32, no. 2, pp. 313–322, 1995.

[25] M. Berci, P. H. Gaskell, R. W. Hewson, and V. V. Toropov, "A semi-analytical model for the combined aeroelastic behaviour and gust response of a flexible aerofoil," *Journal of Fluids and Structures*, vol. 38, pp. 3–21, 2013.

[26] M. D. Conner, D. M. Tang, E. H. Dowell, and L. N. Virgin, "Nonlinear behavior of a typical airfoil section with control surface freeplay: a numerical and experimental study," *Journal of Fluids and Structures*, vol. 11, no. 1, pp. 89–109, 1997.

[27] D. Tang, D. Kholodar, and E. H. Dowell, "Nonlinear response of airfoil section with control surface freeplay to gust loads," *AIAA Journal*, vol. 38, no. 9, pp. 1543–1557, 2000.

[28] D. A. Peters and M. J. Johnson, "Finite-state airloads for deformable airfoils on fixed and rotating wings," *ASME-Publications-AD*, vol. 44, 1994.

[29] D. C. Poirel and S. J. Price, "Post-instability behavior of a structurally nonlinear airfoil in longitudinal turbulence," *Journal of Aircraft*, vol. 34, no. 5, pp. 619–626, 1997.

[30] P. Marzocca, L. Librescu, and G. Chiocchia, "Aeroelastic response of 2-d lifting surfaces to gust and arbitrary explosive loading signatures," *International Journal of Impact Engineering*, vol. 25, no. 1, pp. 41–65, 2001.

[31] D. Tang and E. H. Dowell, "Experimental and theoretical study of gust response for high-aspect-ratio wing," *AIAA Journal*, vol. 40, no. 3, pp. 419–429, 2002.

[32] H. Haddadpour, S. Shams, and M. Kheiri, "Sharp edge gust effects on aeroelastic behavior of a flexible wing with high aspect ratio," in *43rd AIAA Aerospace Sciences Meeting and Exhibit*, 2005, p. 838.

[33] D. Poirel and S. J. Price, "Bifurcation characteristics of a two-dimensional structurally non-linear airfoil in turbulent flow," *Nonlinear Dynamics*, vol. 48, no. 4, pp. 423–435, 2007.

[34] D. Dessi and F. Mastroddi, "A nonlinear analysis of stability and gust response of aeroelastic systems," *Journal of Fluids and Structures*, vol. 24, no. 3, pp. 436–445, 2008.

[35] S. Shams, H. Haddadpour, M. H. Sadr-Lahidjani, and M. Kheiri, "An analytical method in computational aeroelasticity based on wagner function," in *25th International Congress of the Aeronautical Sciences, ICAS 2006*, 2006.

[36] X. Zhang, M. Kheiri, and W.-F. Xie, "Gust response of a two-dimensional nonlinear wing," in *Proceedings of the Canadian Society for Mechanical Engineering International Congress, Toronto, ON, Canada*, 2018.

[37] X. Zhang, M. Kheiri, and W.-F. Xie, "Active control of a two-dimensional nonlinear wing encountering a gust," in *Proceedings of the 27th Canadian Congress of Applied Mechanics, Sherbrooke, QC, Canada*, 2019.

[38] H. Horikawa and E. H. Dowell, "An elementary explanation of the flutter mechanism with active feedback controls," *Journal of Aircraft*, vol. 16, no. 4, pp. 225–232, 1979.

[39] J. A. Luton and D. T. Mook, "Numerical simulations of flutter and its suppression by active control," *AIAA Journal*, vol. 31, no. 12, pp. 2312–2319, 1993.

[40] L. Librescu, S. Na, P. Marzocca, C. Chung, and M. K. Kwak, "Active aeroelastic control of 2-d wing-flap systems operating in an incompressible flowfield and impacted by a blast pulse," *Journal of Sound and Vibration*, vol. 283, no. 3-5, pp. 685–706, 2005.

[41] D. L. York, "Analysis of flutter and flutter suppression via an energy method. MS Thesis, Virginia Tech., Blacksburg, VA." 1980.

[42] S. Mozaffari-Jovin, R. D. Firouz-Abadi, J. Roshanian, and A. Ghaffari, "Discussion on "Active aeroelastic control of 2-D wing-flap systems operating in an incompressible flowfield and impacted by a blast pulse" by librescu et al., *Journal of Sound and Vibration* 283 (3-5)(2005) 685-706," *Journal of Sound and Vibration*, vol. 332, pp. 3351–3358, 2013.

[43] S. Mozaffari-Jovin, R. D. Firouz-Abadi, J. Roshanian, and A. Ghaffari, "Corrigendum to: Discussion on "Active aeroelastic control of 2-D wing-flap systems operating in an incompressible flowfield and impacted by a blast pulse" by librescu et al., *Journal of Sound and Vibration* 283 (3–5)(2005) 685–706 [*Journal of Sound Vibration* 332 (13)(2013) 3351–3358]," *Journal of Sound and Vibration*, vol. 333, no. 25, pp. 7084–7087, 2014.

[44] J. Ko, A. Kurdila, and T. Strganac, "Nonlinear control theory for a class of structural nonlinearities in a prototypical wing section," in *35th Aerospace Sciences Meeting and Exhibit*, 1997, p. 580.

[45] K. Zhang and A. Behal, "Continuous robust control for aeroelastic vibration control of a 2-d airfoil under unsteady flow," *Journal of Vibration and Control*, vol. 22, no. 12, pp. 2841–2860, 2014.

[46] A. Mannarino, E. H. Dowell, and P. Mantegazza, "An adaptive controller for nonlinear flutter suppression and free-play compensation," *Journal of Vibration and Control*, vol. 23, no. 14, pp. 2269–2290, 2017.

[47] Y. Dai and C. Yang, "Methods and advances in the study of aeroelasticity with uncertainties," *Chinese Journal of Aeronautics*, vol. 27, no. 3, pp. 461–474, 2014.

[48] A. Kareem and W.-J. Sun, "Dynamic response of structures with uncertain damping," *Engineering Structures*, vol. 12, no. 1, pp. 2–8, 1990.

[49] J. Ko, T. W. Strganac, and A. J. Kurdila, "Adaptive feedback linearization for the control of a typical wing section with structural nonlinearity," *Nonlinear Dynamics*, vol. 18, no. 3, pp. 289–301, 1999.

[50] X. Zhang, M. Kheiri, and W.-F. Xie, "Adaptive control of a two-dimensional nonlinear wing with structural stiffness and damping uncertainties," in *Proceedings of the 27th Canadian Congress of Applied Mechanics, Sherbrooke, QC, Canada*, 2019.

[51] X. Zhang and W. Yuan, "Development of flutter analysis solver FLUTQ," National Research Council (Ottawa), Tech. Rep., 2019.

[52] D. M. Tang and E. H. Dowell, "Flutter and stall response of a helicopter blade with structural nonlinearity," *Journal of Aircraft*, vol. 29, no. 5, pp. 953–960, 1992.

[53] A. Wolf, J. B. Swift, H. L. Swinney, and J. A. Vastano, "Determining Lyapunov exponents from a time series," *Physica D: Nonlinear Phenomena*, vol. 16, no. 3, pp. 285–317, 1985.

[54] M. Eldred, V. Venkayya, and W. Anderson, "New mode tracking methods in aeroelastic analysis," *AIAA journal*, vol. 33, no. 7, pp. 1292–1299, 1995.

[55] E. Sulaeman, N. Abdullah, and S. Kashif, "Aeroelastic passive control optimization of supersonic composite wing with external stores," in *IOP Conference Series: Materials Science and Engineering*, vol. 184, no. 1. IOP Publishing, 2017, p. 012010.

[56] E. H. Dowell, H. C. Curtiss, R. H. Scanlan, and F. Sisto, *A modern course in aeroelasticity*. Springer, 1989, vol. 3.

[57] J.-J. E. Slotine and W. Li, *Applied Nonlinear Control*. Prentice hall Englewood Cliffs, NJ, 1991.

[58] T. O'Neil, H. Gilliatt, and T. Strganac, "Investigations of aeroelastic response for a system with continuous structural nonlinearities," in *37th Structure, Structural Dynamics and Materials Conference*, 1996, p. 1390.

[59] J. La Salle and S. Lefschetz, *Stability by Liapunov's Direct Method with Applications by Joseph L Salle and Solomon Lefschetz*. Elsevier, 2012, vol. 4.

[60] T. W. Strganac, J. Ko, and D. E. Thompson, "Identification and control of limit cycle oscillations in aeroelastic systems," *Journal of Guidance, Control, and Dynamics*, vol. 23, no. 6, pp. 1127–1133, 2000.